Single-fluid radiation-hydrodynamic modeling of laser-driven EUV-emitting plasmas

Diko Hemminga

VRIJE UNIVERSITEIT

Single-fluid radiation-hydrodynamic modeling of laser-driven EUV-emitting plasmas

ACADEMISCH PROEFSCHRIFT

ter verkrijging van de graad Doctor of Philosophy aan
de Vrije Universiteit Amsterdam,
op gezag van de rector magnificus
prof.dr. J.J.G. Geurts,
in het openbaar te verdedigen
ten overstaan van de promotiecommissie
van de Faculteit der Bètawetenschappen
op maandag 20 november 2023 om 13.45 uur
in een bijeenkomst van de universiteit,
De Boelelaan 1105

door

Diko Jelle Hemminga

geboren te Amstelveen

Cover design by Marinus Jongeneel based on the ideas of Diko Hemminga.

Cover: Dandelion seed head and stem represent the plasma-enveloped tin droplet illuminated by a laser beam. EUV light and ions (seeds) leave the plasma and head towards the collector mirror (soil, on back cover).

Contents

ix

x

Introduction

I

1 Plasma

All throughout history, mankind has wondered about natural phenomena producing bright light on Earth and in the sky above. Examples of such phenomena are the Sun, the stars, the polar aurorae, and lightning. Over the past one-and-half century, it was realized by Langmuir that these natural phenomena are all instances of a fourth state of matter, called 'plasma' [1]. It is now known to be the most abundant form of matter in the universe: from stars and the space in between, to the earthly examples mentioned above. In artificially produced plasmas, a transition from the gas phase to the plasma phase, through ionization of atoms, can be induced by heating to extreme temperatures.

In contemporary physics, there is interest in matter under extreme conditions [2]. Astrophysicists wonder about supernovae and the internal dynamics of stars, enormous projects are undertaken to achieve energy production in controlled fusion reactors, and matter can be made to radiate at alien wavelengths. High-energy-density matter is characterized by extreme temperature, pressure, or charge. Under such extreme conditions, plasma is the phase of matter, from low density in interstellar space to high density inside stars. Plasmas also arise in man-made fusion reactors, from low-density plasma in magnetic confinement fusion (MCF) to high-density in inertial confinement fusion (ICF) reactors. While fusion energy produced by the
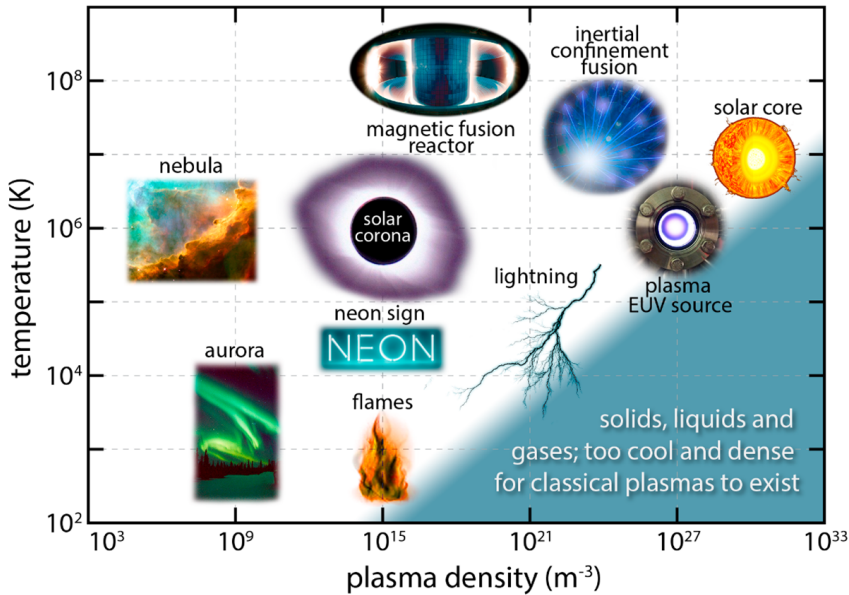
Figure I.1: Density–temperature space with examples of matter in the plasma phase. (Figure: ARCNL)

Sun has nourished our planet for billions of years, since the mid-twentieth century controlled fusion on Earth has been in development as a future man-made energy source, spanning two major branches: magnetic confinement fusion and inertial confinement fusion. Magnetic confinement fusion is investigated in tokamak magnetic confinement devices such as ITER in France [3] and utilizes electric and magnetic fields to enable thermonuclear fusion. In inertial confinement fusion, the needed increase in temperature and pressure is induced by implosion of the fuel [4]. At the end of last year, the Indirect Drive ICF collaboration at the National Ignition Facility in the USA reported for the first time that an ICF device produced more energy than was delivered to the target [5]. This result, known as ignition or scientific breakeven, is a major scientific breakthrough in fusion energy research.

2   Extreme ultraviolet lithography

In the zoo of possible states of matter, examples of which are shown in Fig. I.1, plasmas radiating at a specific wavelength are the topic of this thesis. These plasmas are

engineered for the emission of extreme ultraviolet (EUV) light, the wavelength region between ultraviolet and (soft) x-ray radiation. In the state-of-the-art equipment for the semiconductor industry, an EUV light beam with a wavelength of 13.5 nm is the 'sharp pencil' for drawing the smallest features of integrated circuits in silicon in a process known as extreme ultraviolet lithography (EUVL) [6, 7]. The foundation of such an optical lithography process is light being absorbed by a photoresist material in the illumination step. The illumination occurs in the pattern transferred to the light beam by a photomask. Next, due to changes in solubility in the photoresist material, the material at the exposed locations can be removed to leave the desired structure behind [6, (Ch. 8)]. While this is the end point of each illumination in the lithography process, the focus of this thesis lies on the source of the light utilized.

The wavelength of 13.5 nm, down from the previous state-of-the-art using 193 nm, allows for a fundamentally smaller (critical) dimension of such a pattern, as summarized by Abbe's diffraction limit [6, (Ch. 1)], which states that the smallest structures resolvable, thus 'printable', by a wavelength λ have a size $\lambda/(2\text{NA})$, where NA denotes the numerical aperture. Therefore, EUVL is the latest leap in the continuation of one of the exponential laws of computing growth [8]: the doubling of components per area every two years, known as Moore's law[*], has continued for well over fifty years [9–11]. Denning [8] notes that Moore's law is one of the most durable technology forecasts ever made and has become a design objective in the semiconductor industry. The relentless size scaling of the computer chip has enabled the information age with technical, economic, and social revolutions. The improvement in energy efficiency, summarized as Koomey's law [11], is quantified by the exponential growth of the number of computations per kWh of electricity used. In this century, this may become of particular importance in an energy-constrained world: from the electricity consumption of large data centers to battery life, the scaling embodied in Koomey's law has already enabled the rise of cloud services and mobile devices over the past decades.

State-of-the-art EUV nanolithography machines have been developed, where extreme ultraviolet light is emitted from a tin plasma produced by a pulsed CO_2 gas laser operating at a wavelength of $\lambda_{\text{laser}} = 10.6\,\mu\text{m}$. The plasma formation repeats at a rate of tens of kilohertz on pizza-shaped targets shaped by a so-called pre-pulse from droplets tens of micrometer in size. The EUV light from this pulsed source is focused by a collector mirror spanning the 2π solid angle of the laser-illuminated side to be utilized in the so-called scanner for nanolithography. Based on such EUV source design, EUV nanolithography has entered high-volume manufacturing [7,

---

[*]Gordon Moore sadly passed away on the 24th of March, 2023, during the writing of this thesis.

12]. The laser-produced plasma emitting EUV light is characterized by temperatures of tens of eV (or several 10^5 Kelvin) and electron densities of $10^{18} - 10^{21}$ e^- cm^{-3}. As schematically presented in Fig. I.1, the EUV source plasma can be regarded as high density and moderately high temperature in comparison to other plasmas.

The wavelength of 13.5 nm has been selected due to the availability of a method for the manipulation of the EUV light. As common optics absorb EUV light, one has to utilize mirrors built up from multiple layers for reflecting the light, i.e., utilizing Bragg reflection. In the so-called in-band region, 13.5 nm $\pm 1\%$, molybdenum-silicon multilayer mirrors exhibit high reflectance due to this process [13, 14]. Extreme ultraviolet light can be efficiently generated from a tin plasma due to emission through bound-bound atomic transitions in $Sn^{11+} - Sn^{15+}$ ions [15, 16]. These transitions form an unresolved transition array (UTA) in the emission spectrum centered around 13.5 nm [17]. Recent work has uncovered the importance of multiply excited states contributing to the EUV emission [18, 19].

The industrial application puts special requirements on controlling the plasma physics. The EUV output must be optimized, which includes efficient generation but also efficient transport from the source to the scanner, and achieving a constant dose with continuous uptime of the nanolithography machine [7, 12]. Optimization of the EUV emission efficiency builds upon knowledge of atomic and plasma physics, as well as the hydrodynamics governing the laser pre-shaping of the tin microdroplet. Important scientific contributions, already implemented in the process, substantiate the emission properties of tin [15–17] and its use in the form of mass-limited droplets [20], to increase EUV light output while minimizing tin droplet 'debris'. Moreover, the action of pre-shaping the droplet with an additional pulse was recognized early as a way to improve emission efficiency [21], as a result of creating lower densities and longer scale lengths.

3   Laser-produced plasma

Elements of the laser-produced plasma (LPP), the source of EUV light, provide different perspectives on the physics of hot, dense plasmas and the fluid physics of liquid metal after interaction with a directed impulse. The understanding and characterization of the created plasma lie at the heart of both scientific and industrial interests. Plasma properties, such as density and temperature, can be directly influenced by changing the laser parameters. For example, the plasma density is closely related to the laser wavelength through the dependence of the critical electron density on laser wavelength. Moreover, plasma temperature scales with laser

intensity. The emission characteristics of the LPP are directly influenced by these plasma properties. Naturally, the plasma density determines the density of tin ions, while the plasma temperature influences the presence of the EUV-emitting charge states. Importantly, the plasma density also directly determines the optical depth of the plasma for EUV emission. The optical depth is defined as the integral of the attenuation coefficient over the path of an EUV photon. Higher densities lead to smaller mean free paths, which cause higher optical depths: an EUV photon can be repeatedly reabsorbed and re-emitted while traversing the plasma. The result is a spectral broadening of the tin emission peak at 13.5 nm.

For quantification, two measures for the radiative efficiency of the EUV source are commonly used. Spectral broadening is quantified in the spectral purity (SP), which is defined as the ratio between the radiated energy (or power) emitted in the in-band region and the total radiated energy (or power). The in-band radiative efficiency of the laser-produced plasma is condensed in a quantity known as the conversion efficiency (CE), which is defined as the ratio of the in-band emission energy into the laser-illuminated half-sphere to the laser pulse energy. In addition to conversion efficiency, efforts have been concentrated on raising the power of the in-band EUV emission. In search of optimal emission efficiency and increased radiative power for industrial applications, characterization of the plasma properties may guide future opportunities.

As a result of the high plasma temperature, the high plasma pressure and resulting strong gradients induce plasma expansion in all directions away from the droplet. The expansion of the plasma is non-trivial under EUV source conditions, as quantified by the distribution of ions over kinetic energy: the dynamics of the created plasma is induced by the temporal profile of the laser pulse. An essential component for EUV light transport, the collector mirror, is placed on the laser-illuminated side to capture the EUV light emission. However, the particularly energetic plasma ions are directed towards the collector mirror, with the potential of causing mirror degradation. The efficiency and uptime of the nanolithography machine may therefore be compromised by the plasma expansion. Therefore, characterization and subsequent mitigation of the ionic debris is necessary [22, 23].

As the plasma is formed by a laser pulse with a pulse length of $\tau_{\mathrm{FWHM}} = 10\,\mathrm{ns}$, high plasma pressures create a short impulse (on the same timescale as the laser pulse) on the droplet surface, inducing liquid dynamics which persists over a timescale of microseconds. The liquid volume is propelled and, coincidently, deformed into a pizza-like shape [24–26]. Research into the preparation of the desired target morphology is ongoing, in search of optimal conditions. This includes improvement of EUV emission properties such as conversion efficiency and radiative

power, as well as increased tin mass efficiency, which is closely related to decreased amounts of liquid debris.

While state-of-the-art industrial EUV sources are based on CO_2 gas lasers to drive plasma formation and heating, solid-state lasers are a viable alternative in the future. Such solid-state lasers, typically operating in the near- to mid-infrared wavelength range, are undergoing rapid developments [27, 28] and show high efficiencies in converting electrical power to laser light and potential for scaling to high average powers.

Currently, the knowledge of EUV light sources driven by solid-state lasers is insufficiently complete to employ such EUV sources in the EUV nanolithography industry. In this thesis, first the understanding of plasma expansion and high-energy ion emission is advanced for Nd:YAG-laser ($\lambda_{\text{laser}} = 1.064\,\mu\text{m}$) illumination. Second, the characterization of plasmas driven by solid-state lasers operating at wavelengths $\lambda_{\text{laser}} = 1.064$ or $2\,\mu\text{m}$ is progressed. Both laser systems are being experimentally investigated as EUV source drivers. Moreover, the wavelength region between $\lambda_{\text{laser}} = 2\,\mu\text{m}$ and $\lambda_{\text{laser}} = 10.6\,\mu\text{m}$ is explored in search of efficient future EUV source designs.

The aim of this thesis is to investigate the suitability of applying single-fluid radiation-hydrodynamic modeling to laser-produced, EUV-emitting plasmas and, next, to utilize it to guide experiments, with the ambition to enable designing next-generation EUV light sources.

4   Research methodology

Similar to contemporary work on high-energy-density physics [2], a combined numerical and experimental study is conducted. The research presented in this thesis is based on numerical simulations in conjunction with experimental measurements. The measurements have been performed by colleagues in the EUV Plasma Processes group at the Advanced Research Center for Nanolithography (ARCNL), encompassing both plasma expansion diagnostics and imaging of the droplet dynamics. The numerical simulations reveal the underlying physical processes at a level of detail unobtainable in experiments. Moreover, the set of physical variables that can be quantified is significantly larger, including fundamental quantities such as plasma density, pressure, temperature, and velocity. Before the simulations are employed to enrich the studies further, the experimental measurements are used to validate the modeling approach on 'observables' available in both experiments and simulations.

For the physical description employed in the simulations, a simplified approach is combined with the inclusion of essential physical processes. The central simplification is the approach based on single-fluid, single-temperature fluid dynamics. Additional energy transport in the fluid is enabled through thermal conduction and radiation transport, e.g., EUV emission. Essential to a laser-produced plasma is the inclusion of laser light transport, absorption, and reflection.

This physical model is implemented in a radiation-hydrodynamics code, RALEF-2D, to perform two-dimensional simulations of tin plasma formation, EUV emission, subsequent plasma expansion, and early-time liquid droplet dynamics. As surface tension is not included in the simulation approach, only the droplet dynamics during early times is considered, where the related forces play a negligible role. An advantage of the simulations is the spatially and temporally resolved view into the laser-produced plasma dynamics, at a level of detail unattainable in experiments. Lastly, the simulations have been employed for the prediction of plasma characteristics driven by laser wavelengths yet to be experimentally explored. Thereby, after validating the simulation approach, the detailed characterization of the laser-produced plasma may guide ongoing and future experiments.

5 Thesis outline and summary

This thesis presents work on radiation-hydrodynamic simulations of tin droplet-based laser-produced plasmas, including plasma characterization, plasma expansion, and subsequent early-time droplet dynamics. A schematic of the tin droplet-based laser-produced plasma is displayed in Fig. I.2 along with the topics discussed in this thesis. The topics mentioned will be presented in the following order: the principles of radiation-hydrodynamic modeling employed in this work (Chapter 1), the non-trivial plasma expansion and its influence on the distribution of plasma ions over energy and space (Chapters 2 and 3), the early-time dynamics of a liquid droplet after laser impact (Chapter 4), and the characteristics of plasma driven by a broad range of laser wavelengths and intensities (Chapter 5).

In **Chapter 1**, an overview of the physical models underlying the simulations is given. After an introduction to laser-produced plasma physics, a description known as kinetic theory is first discussed. From this description, the backbone of the model is consequently derived, and condensed to conservation equations of mass, momentum, and energy. The approach is based on a single-fluid, single-temperature model for the description of the laser-produced plasma. The implementation of the energy transport processes is discussed next: heat conduction, radiation transport, and laser
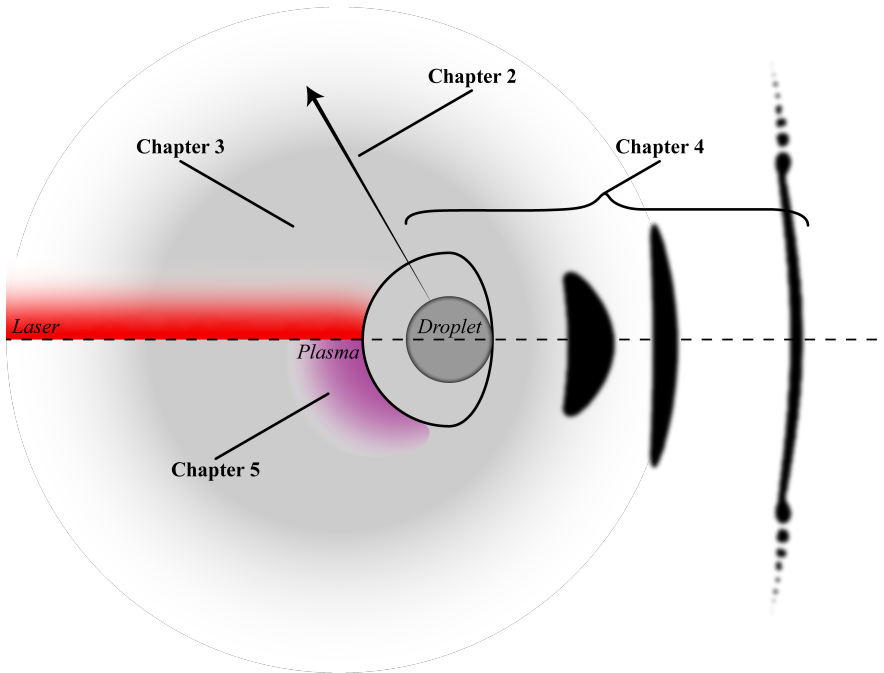
Figure I.2: Schematic of laser illumination (red) of a tin microdroplet (dark gray), EUV emission (purple), and subsequent droplet deformation dynamics (black). The topics of the chapters of this thesis are indicated: in Ch. 2, the plasma expansion (gray shading) under a 60° angle is investigated. Next, the investigation is extended to the full space in Ch. 3. In Ch. 4, the early-time dynamics of a droplet deforming upon laser impact is discussed. Lastly, in Ch. 5, the details of the laser absorption and EUV emission around the critical surface (black contour) are examined.

absorption. For the closure of the system of fluid equations, the topic of equation-of-state is discussed. The chapter ends with analytical solutions describing plasma expansion based on simplifying assumptions, as preparation for the next two chapters.

In **Chapters 2 and 3**, the investigation of the expansion of a laser-produced tin plasma is discussed. Both chapters report on joint experimental and numerical studies of plasmas generated by Nd:YAG laser pulse ablation of tin microdroplets under conditions relevant for extreme ultraviolet lithography. Good agreement is found between the simulations and the experimental measurements on the ion kinetic energy distribution, which quantifies the number of ions propagating in a certain direction as a function of kinetic energy.

In **Chapter 2**, the focus lies on the shape of the ion kinetic energy distribution. Measurements reveal a near-plateau in the distribution for kinetic energies

in the range 0.03 – 1 keV and a peak near 2 keV followed by a sharp fall-off in the distribution for energies above 2 keV. Charge-state-resolved measurements attribute this peak to the existence of peaks centered near 2 keV in the Sn^{3+} – Sn^{8+} ion energy distributions. The two-dimensional radiation-hydrodynamic simulations of the laser–droplet interaction and subsequent plasma expansion, as introduced before, are employed to better understand the physical processes governing the shape of the distribution. This leads to attributing a peak in the distribution near 2 keV to a quasi-spherical expanding shell formed at early times in the expansion. The good agreement between simulated and experimental data covers both the shape of the distribution and the absolute number of detected ions.

Chapter 3 extends the investigation of plasma expansion by studying its angular dependence. Whereas in Ch. 2 measurements are performed with an electrostatic analyzer (ESA) at a single angle, in Ch. 3 absolutely calibrated, charge-state-resolved measurements are reported of the ion emission with retarding field analyzers (RFAs) positioned at seven angles. The measurements of the ion kinetic energy distributions under this multitude of angles reveal strongly anisotropic emission characteristics. Again, close agreement is found with the two-dimensional radiation-hydrodynamic simulations, extending the favorable comparison. Furthermore, the angle-resolved ion spectral measurements enable the accurate prediction of the plasma propulsion of the laser-impacted droplet.

The plasma propulsion of a tin microdroplet after laser impact is a central topic addressed in **Chapter 4**. Here, a joint experimental and numerical investigation is presented of the early-time hydrodynamic response of a tin microdroplet due to a laser-produced plasma. Using stroboscopic microscopy, the propulsion speed and the initial radial expansion rate are determined over an extensive parameter space of tin droplet sizes, laser beam diameters, and laser pulse energies. Good agreement is found between the experimentally obtained values and those extracted from the radiation-hydrodynamic simulations, thus validating the modeling approach in this new context. After this model validation, the spatial distribution of the plasma-driven pressure impulse at the droplet–plasma interface is considered, as extracted from the simulations. The influence of the pressure impulse on the partitioning of kinetic energy is quantified, specifically energy channeled into propulsion or deformation. In conclusion, the width of the pressure impulse is the pertinent parameter for extracting the kinetic energy partitioning. Related to this finding is the good agreement found between the full radiation-hydrodynamic modeling and a generalized analytical fluid-dynamics model. The early-time dynamics, as quantified by the kinetic energy partitioning, ultimately determines the late-time target morphology, so these findings can be used to tailor the features of tin targets for applications in

EUV nanolithography.

In **Chapter 5**, the next step is undertaken, from the kinetic energy partitioning inside the tin droplet to the full energy partitioning of the laser-produced plasma. The tin droplet-based laser-produced plasma is characterized, being driven by laser wavelengths in the $\lambda_{\text{laser}} = 1.064 - 10.6\,\mu\text{m}$ range and laser intensities of $I_{\text{laser}} = 0.5 - 5 \times 10^{11}\,\text{W}\,\text{cm}^{-2}$ for $\lambda_{\text{laser}} = 1.064\,\mu\text{m}$. The numerical simulations reveal a strong laser-wavelength dependence of both laser absorptivity and the conversion efficiency. Moreover, with increasing laser intensity for $\lambda_{\text{laser}} = 1.064\,\mu\text{m}$ irradiation, the increase in in-band radiation is offset by only a minor reduction in conversion efficiency. Examining the energy partitioning inside the plasma, radiative losses are found to dominate the power balance for all laser wavelengths and intensities. A clear shift from kinetic to in-band radiative losses is found with increasing laser wavelength. Yet, with increasing laser intensity, a shift is absent. The existence of an optimum 'drive' laser wavelength is reported that maximizes the conversion efficiency for this specific droplet-target geometry. Based on the analysis of the energy partitioning, this optimum originates from the interplay between the optical depth of the plasma for the incoming laser light and the optical depth for the outgoing in-band EUV light. Quantitatively, the concave dependence can be understood from the laser absorptivity, which monotonically decreases with increasing laser wavelength due to the decreasing optical depth for laser light, and the spectral purity of the EUV emission, which monotonically increases with increasing wavelength due to the decreasing optical depth for EUV light.

In summary, this thesis presents radiation-hydrodynamic modeling of tin droplet-based laser-produced plasmas. The work is closely connected to experimental measurements, be it to successfully validate the simulation results on plasma expansion and droplet dynamics, or to guide future experiments towards optimal EUV emission conditions. It is shown that, after validation, the simulations can provide additional insight into (i) non-trivial plasma dynamics leading to the measured ion kinetic energy distributions and (ii) the plasma impulse shaping the early-time droplet dynamics that ultimately determines the late-time droplet morphology. Moreover, the simulations can successfully explore a broad range of laser wavelengths and intensities. Finally, these investigations aim to complement efforts to increase the performance of the EUV source system: the conversion efficiency of laser pulses to in-band EUV radiation as well as the lifetime of the collector mirror, which may be affected by ionic or liquid debris.

1

Radiation hydrodynamics as a model for laser-produced plasma

In this first chapter, the theory and background of our approach for modeling laser-produced plasmas is provided. First, a short introduction to plasmas is given, in particular those produced by laser illumination. Second, kinetic theory is introduced, where solutions to the Boltzmann equation, called distribution functions, describe the plasma properties. From these distribution functions, the approach taken in our modeling is derived: a fluid approach. Then the underlying assumptions of single-fluid single-temperature radiation hydrodynamics are discussed in detail. In the discussion of the system of equations used in the modeling, special attention is given to the energy source and sink terms. The closure of the system of equations is achieved by means of an equation-of-state. Lastly, building up to the next two chapters of this thesis, analytical solutions to plasma expansion are discussed based on the single-fluid approach.

1.1 Plasma

Plasma physics encompasses a broad field of research, spanning stellar atmospheres, solar physics, lightning, magnetic and inertial confinement fusion as well as light sources for lithography and microscopy [29]. In simple terms, a plasma can be described as an ionized gas: a mixture of positively charged ions, negatively charged electrons and neutral atoms. The difference between the two lies in the possible interactions: in a plasma, electromagnetic fields play an important role. This fourth state of matter (next to solid, liquid and gas), is the most abundant in the universe. On Earth, human-made plasma technologies are an ever-growing interest, e.g., neon lights, nuclear fusion and laser-produced plasmas: the last being the topic of this thesis.

As alluded to above, plasmas differ from gases by the existence of long-range, electromagnetic interactions, which leads to the occurrence of collective motion. One such example is rapid oscillations of the electron density, n_e, known as plasma oscillations or Langmuir waves. If the thermal motion of the electrons is ignored, one finds that the plasma frequency of the oscillation is given by

$$\omega_{pe} = \sqrt{\frac{n_e q_e^2}{\varepsilon_0 m_e}}, \tag{1.1}$$

which depends on the free electron number density n_e, electron charge $q_e = -e$ and mass m_e, as well as the fundamental constant ε_0 called the vacuum permittivity.

1.1.1 Laser-produced plasmas

Laser-produced plasmas (LPPs) are typically created by irradiation of the laser beam of $10^8 - 10^{21}$ W cm^{-2} on a solid or liquid target [30, 31]. The plasma creation proceeds through several phases: laser absorption in the target material, heating and ablation of the upper layer of material, followed by further laser absorption in the ablated plasma layer [30].

Laser absorption in a plasma is dominated by inverse Bremsstrahlung, where an incoming laser photon is absorbed by a plasma electron while the electron collides with a plasma ion. In other words, laser energy is converted to kinetic energy of the plasma electrons. The process is sometimes referred to as a free–free transition, as the electron is free (unbound) before and after the interaction [32]. The term Bremsstrahlung comes from the opposite process, where electromagnetic radiation is produced by the deceleration of a charged particle when deflected by another

charged particle. A common example is an electron being deflected by an atomic nucleus. The loss in kinetic energy is converted to radiation. Consequently, elastic collisions between (accelerated) electrons and ions yield conversion of the electron's kinetic energy into kinetic energy of the ions, thereby heating the plasma [33, (Ch. 10)]. The numerical implementation of laser absorption will be discussed in detail in Sec. 1.4.3. An important concept related to LPPs is the existence of a critical electron density. At this electron density, the plasma becomes opaque to the laser irradiation [32]. In other words, at this 'cut-off' frequency, the index of refraction goes to zero and the light wave is fully attenuated. The critical electron density is defined as the electron density n_e where the plasma frequency ω_{pe} (which depends on n_e as defined in Eq. (1.1)) equals the laser frequency ω_{laser}. The formula for the critical electron density $n_{e,cr}$ is found to be

$$n_{e,cr} = \frac{\varepsilon_0 m_e}{e^2} \omega_{laser}^2. \tag{1.2}$$

Written in terms of the laser wavelength, $\lambda_{laser} = 2\pi c/\omega_{laser}$, one finds

$$n_{e,cr} = \frac{4\pi^2 c^2 \varepsilon_0 m_e}{e^2} \frac{1}{\lambda_{laser}^2} \approx 1.1 \cdot 10^{21} \left(\frac{\mu m^2}{\lambda_{laser}^2} \right) cm^{-3}. \tag{1.3}$$

In the context of LPPs as light source for extreme ultraviolet nanolithography, laser intensities of interest are situated in the range $10^9 - 10^{12}$ W cm^{-2} for the creation of the plasmas emitting EUV radiation. In comparison to other plasma examples (see I.1 in the Introduction), the EUV-emitting laser-produced plasma is characterized as hot and dense, with $T_e = 20 - 40$ eV and $n_e = 10^{18} - 10^{21}$ cm^{-3} [17, 34]. The laser frequency plays an important role in determining the plasma conditions due to its relation with the critical electron density. It therefore determines the location where laser energy is deposited, resulting in locations of maximum plasma temperature. Laser-produced plasmas for a laser wavelength (λ_{laser}) of 1.064 μm are investigated in Ch. 2 – 4 of this thesis, whereas in Ch. 5 the influence of the laser wavelength on the plasma conditions is explored in detail. In high-density conditions generated by short-wavelength lasers such as $\lambda_{laser} = 1.064$ μm, the plasma is dominated by collisions and is often approximated as being in local thermodynamic equilibrium (LTE) [33, (Ch. 10)]. In LTE, the populations of the available energy levels are determined by electron–ion collisions. The effect of radiation processes on these populations is assumed to be negligible. Therefore, LTE conditions particularly apply when collisional processes are dominant over radiative processes, and

if radiation can escape from the plasma, i.e., an optically thin plasma. This assumption is often invoked when describing energy transport by radiation, and is also used in our approach: in Sec. 1.4.2 the quasi-static, LTE radiation transport equation will be discussed.

A second important concept in plasma physics is that of quasi-neutrality. In this approximate picture, the plasma is electrically neutral on average: positively charged ions are found in a cloud of negatively charged electrons, which effectively screens the ion charge to their environment. The length over which the electric potential decreases by $1/e$ (inverse Euler's number) is known as the Debye length [35]. If ion motion is negligible, the Debye length is given by

$$\lambda_{\mathrm{D}} = \sqrt{\frac{\varepsilon_0 k_{\mathrm{B}} T_{\mathrm{e}}}{n_{\mathrm{e}} q_{\mathrm{e}}^2}}, \tag{1.4}$$

given the electron temperature T_{e}, electron number density n_{e} and electron charge $q_{\mathrm{e}} = -e$ (minus elementary charge), as well as the vacuum permittivity ε_0 and the Boltzmann constant k_{B}. A short Debye length corresponds to a strong screening of the ion charge, which occurs for a high electron density and low electron temperature. So, a short Debye length describes a case closer to an electrically neutral fluid where electromagnetic fields play a minor role.

From its dependence on electron number density and (electron) temperature, one can derive characteristic values of the Debye length for EUV source plasma conditions. In the hot ($T_{\mathrm{e}} \approx 20 - 40$ eV) and dense ($n_{\mathrm{e}} \approx 10^{19} - 10^{21}$ cm^{-3}) region of the plasma, one can find $\lambda_{\mathrm{D}} < 10$ nm. In Sec. 1.3 this value is used as an argument for the applicability of a single-fluid approach to EUV source plasma modeling.

1.2 Kinetic theory of plasma

A description of plasma physics should both (i) be able to treat collective motion and (ii) lead to a manageable set of mathematical equations. Therefore, an approach based on tracking every particle is impossible, and it is appropriate and convenient to use a statistical approach. Such description considers the distribution of the particles over physical space and their distribution over different velocities (or, equivalently, momenta). This is the basis of plasma kinetic theory [35]. After choosing a coordinate system, the dynamical state of each particle is specified by the position coordinates of its center of mass (together forming configuration space) and its velocity coordinates (forming velocity space) of the linear velocity of the center of

mass. In this description, a so-called phase space is considered combining config-uration and velocity space. In this six-dimensional space, the state of each particle is represented by a single point with coordinates $(\vec{\mathbf{r}}, \vec{\mathbf{v}})$. Summarizing, a distribution function f over phase space is considered, which can be understood as a probability distribution function for the position $\vec{\mathbf{r}}$ and velocity $\vec{\mathbf{v}}$ of a typical particle.

Having defined phase space, let us now consider a small element of volume in this space. Note that it should be interpreted as a finite element of volume, which is both sufficiently large to contain many particles and sufficiently small with respect to the characteristic length scale of any spatial variation of physical variables, such as number density. So, although this volume element is used as differential form in volume integrals in the following, it should not be interpreted as a mathematically infinitesimal quantity. The familiar volume element in configuration space d^3r is combined with its equivalent in velocity space, d^3v, to find a differential volume element in our six-dimensional phase space: $d^3r\, d^3v$. The number of representative points, or dynamical states of a particle, inside the volume element $d^3r\, d^3v$ is, in general, a function of the coordinates of this element in phase space and of time. The coordinates $\vec{\mathbf{r}}$ and $\vec{\mathbf{v}}$ of phase space are considered to be independent variables.

1.2.1   Distribution functions and the Boltzmann equation

Next, let us define $d^6\mathcal{N}(\vec{\mathbf{r}}, \vec{\mathbf{v}}, t)$ as the number of particles inside the volume element $d^3r\, d^3v$ around the phase space coordinates $\vec{\mathbf{r}}, \vec{\mathbf{v}}$ at a time t. The distribution function in phase space follows this definition as

$$f(\vec{\mathbf{r}}, \vec{\mathbf{v}}, t) = \frac{d^6\mathcal{N}(\vec{\mathbf{r}}, \vec{\mathbf{v}}, t)}{d^3r\, d^3v}, \tag{1.5}$$

representing the density of representative points (or particle states) in phase space. From its definition, it is a positive and finite function at any instant in time. It can be considered a continuous function of its arguments, as it is assumed the density in phase space does not vary rapidly. Moreover, physical considerations require that f must tend to zero as the velocity becomes infinitely large.

In a statistical sense, the distribution function provides a complete description of the system. As will be explicitly worked through in Sec. 1.3.1, macroscopic vari-ables of physical interest can be derived from knowing $f(\vec{\mathbf{r}}, \vec{\mathbf{v}}, t)$. So, one of the pri-mary challenges of kinetic theory is in determining the distribution function. The

differential equation that governs the temporal and spatial variation of the distribution function is generally known as the Boltzmann equation. In the absence of particle collisions (and radiation losses, particle production or loss), it takes the form [35]

$$\frac{\partial f(\vec{r}, \vec{v}, t)}{\partial t} + \vec{v} \cdot \nabla_r f(\vec{r}, \vec{v}, t) + \vec{a} \cdot \nabla_v f(\vec{r}, \vec{v}, t) = 0, \tag{1.6}$$

which can be also be understood as the total derivative with respect to time t in phase space applied to the distribution function f. So gradients of the distribution function f are taken to both position (∇_r) and velocity (∇_v). Its form presented here uses $\vec{a} = \vec{F}/m$ as the particle acceleration as a result of an external force $\vec{F}$ (with m denoting the particle mass). In the presence of collisions, Eq. (1.6) is modified by replacing the zero on the right-hand side of this equation by a collision term

$$\left(\frac{\delta f(\vec{r}, \vec{v}, t)}{\delta t} \right)_{\text{coll}},$$

which denotes the change of the distribution function in time due to collisions. Naturally, without a precise form for this term the collisional Boltzmann equation is incomplete, but these details will not be examined here.

1.2.2 Vlasov equation

For the description of plasma dynamics, it is useful to consider the plasma particle motion governed by macroscopic average internal fields in addition to external forces. These electromagnetic fields are due to the presence and motion of all plasma particles, and require a self-consistent solution to be found, meaning that the particle positions determine the average electromagnetic fields and vice versa. The collisionless Boltzmann equation (given in Eq. (1.6)) including internal fields is commonly known as the Vlasov equation. This is written

$$\frac{\partial f}{\partial t} + \vec{v} \cdot \nabla_r f + \frac{1}{m} \left[\vec{F}_{\text{ext}} + q(\vec{E}_{\text{int}} + \vec{v} \times \vec{B}_{\text{int}}) \right] \cdot \nabla_v f = 0. \tag{1.7}$$

In this equation, $\vec{F}_{\text{ext}}$ represents external forces such as those generated by *externally* applied electric and magnetic fields, and $\vec{E}_{\text{int}}$ and $\vec{B}_{\text{int}}$ are macroscopic internal electric and magnetic fields due to all charged particles inside the plasma, included as the Lorentz force on a particle of charge q (and mass m). A complete set of self-consistent equations is defined by combining Eq. (1.7) with the Maxwell equations, which describes the dynamics of electric $\vec{E}$ and magnetic fields $\vec{B}$ based on plasma

charge density ρ_c and plasma current density $\vec{\mathbf{J}}_c$. Similar to the derivation of the number density and flow velocity in Sec. 1.3.1, the charge density and current density can be related to the particle distribution function f. Therefore, the system of equations containing the Vlasov and Maxwell equations is closed, coupled through the charge density, current density, and the electric and magnetic fields.

1.2.3 Macroscopic quantities based on distribution functions

Macroscopic variables, such as number density, flow velocity, pressure and thermal energy flux, involve the collective behavior of many particles and may be considered as the average values of certain physical variables. The systematic method discussed here [35] relates macroscopic variables to moments of the distribution function, which can be seen as averaging a physical variable, such as velocity, weighted by the probability distribution function (representing the probability of finding a particle with that velocity). Let us recall the definitions of the particle distribution function $f(\vec{\mathbf{r}}, \vec{\mathbf{v}}, t)$ and the closely related expression $d^6 \mathcal{N}(\vec{\mathbf{r}}, \vec{\mathbf{v}}, t)$ for the number of particles inside a volume element $d^3r \, d^3v$. Firstly, the number density, $n(\vec{\mathbf{r}}, t)$, is a macroscopic variable defined as the number of particles per unit volume. It can be derived from $d^6 \mathcal{N}$ by integrating over all velocity space and dividing by the size of the volume element in configuration space, d^3r. This is written

$$n(\vec{\mathbf{r}}, t) = \frac{\int_v d^6 \mathcal{N}(\vec{\mathbf{r}}, \vec{\mathbf{v}}, t)}{d^3r}. \tag{1.8}$$

In terms of a particle distribution function $f(\vec{\mathbf{r}}, \vec{\mathbf{v}}, t)$, the expression becomes

$$n(\vec{\mathbf{r}}, t) = \int_v f(\vec{\mathbf{r}}, \vec{\mathbf{v}}, t) d^3v, \tag{1.9}$$

which can be understood as the zeroth velocity moment of f. In this simplified notation, this single integral must be interpreted as a triple integral over the full (infinite) velocity space.

Secondly, the average velocity $\vec{\mathbf{u}}(\vec{\mathbf{r}}, t)$ can be considered, which is based on the first velocity moment of f. It is defined as the macroscopic flow velocity of particles in the volume element at $\vec{\mathbf{r}}$ at an instant t. Again, in terms of distribution function f, $\vec{\mathbf{u}}(\vec{\mathbf{r}}, t)$ is defined as

$$\vec{\mathbf{u}}(\vec{\mathbf{r}}, t) = \frac{1}{n(\vec{\mathbf{r}}, t)} \int_v \vec{\mathbf{v}} f(\vec{\mathbf{r}}, \vec{\mathbf{v}}, t) d^3v. \tag{1.10}$$

Note that both macroscopic variables $n(\vec{\mathbf{r}}, t)$ and $\vec{\mathbf{u}}(\vec{\mathbf{r}}, t)$ are functions of only position and time. Consequently, let us define a notation for the average value of a certain variable $\chi(\vec{\mathbf{v}})$,

$$\left\langle \chi(\vec{\mathbf{v}}) \right\rangle = \frac{1}{n(\vec{\mathbf{r}}, t)} \int_v \chi(\vec{\mathbf{v}}) f(\vec{\mathbf{r}}, \vec{\mathbf{v}}, t) \mathrm{d}^3 v, \qquad (1.11)$$

such that $\vec{\mathbf{u}}(\vec{\mathbf{r}}, t)$ now simply becomes $\left\langle \vec{\mathbf{v}} \right\rangle$.

1.2.4 Maxwell–Boltzmann distribution and the Boltzmann factor

A well-known solution to the Boltzmann equation (Eq. (1.6)) in the absence of external forces ($\vec{\mathbf{F}} = 0$) is the time-independent solution: the equilibrium distribution function, which is also known as the Maxwell–Boltzmann or Maxwellian velocity distribution function [35]. In this state, particle interactions such as collisions cause no changes in the distribution $\left(\left(\partial f(\vec{\mathbf{r}}, \vec{\mathbf{v}}, t)/\partial t \right)_{\text{coll}} = 0 \right)$ and particles are uniformly distributed without spatial gradients ($\nabla_r f = 0$). The result is

$$f(c) = n \left(\frac{m}{2\pi k_{\mathrm{B}} T} \right)^{3/2} \exp\left(-\frac{mc^2}{2k_{\mathrm{B}} T} \right), \qquad (1.12)$$

where c denotes the magnitude of the random velocity $\vec{\mathbf{c}} = \vec{\mathbf{v}} - \vec{\mathbf{u}}$, based on the particle velocity $\vec{\mathbf{v}}$ and average flow velocity $\vec{\mathbf{u}}$ (definition in Eq. (1.10)). Note that the formulation of $f(c)$ in Eq. (1.12) is a number distribution function (over velocity space) instead of a probability distribution. Therefore, the expression is based on number density n, which is constant over space, as defined in Eq. (1.9).

As an extension to the Maxwell–Boltzmann distribution, consider a gas under steady-state conditions in a conservative force field. In this case, the distribution function differs by a quantity known as the Boltzmann factor. For a conservative force field $\vec{\mathbf{F}}(\vec{\mathbf{r}}) = -\nabla U(\vec{\mathbf{r}})$ and with $\vec{\mathbf{u}} = \vec{\mathbf{0}}$, the equilibrium distribution function becomes

$$f(\vec{\mathbf{r}}, v) = n_0 \left(\frac{m}{2\pi kT} \right)^{3/2} \exp\left(-\frac{\frac{1}{2}mv^2 + U(\vec{\mathbf{r}})}{k_{\mathrm{B}} T} \right). \qquad (1.13)$$

The corresponding number density is amended by the Boltzmann factor and is given by

$$n(\vec{\mathbf{r}}) = n_0 \exp\left[-\frac{U(\vec{\mathbf{r}})}{k_{\mathrm{B}} T} \right]. \qquad (1.14)$$

In the context of electrostatics in a plasma, an important example is found: a conservative force due to an electrostatic field. For an electrostatic scalar potential $\phi(\vec{r})$, the field becomes $\vec{E} = -\nabla\phi(\vec{r})$ and the corresponding potential energy $U(\vec{r}) = q\phi(\vec{r})$, resulting in

$$n(\vec{r}) = n_0 \exp\left[-\frac{q\phi(\vec{r})}{k_B T}\right]. \tag{1.15}$$

for the number density for particles of charge q in equilibrium under the action of an electrostatic field. In the literature of plasma expansion discussed in Sec. 1.6, this form is utilized as an ansatz of the particle distribution.

1.3   Fluid approach to plasma modeling

In this section, the approach to plasma modeling utilized in this thesis is outlined. First, the derivation of the fluid approach from kinetic theory is discussed. Second, further simplifications to the fluid model are introduced used in the work presented in this thesis: assumptions of a single-fluid, single-temperature model. Next, based on this model, the fluid equations are stated which are numerically solved and the system of equations is closed by discussing the adopted equation-of-state. Special attention is placed on explaining the energy source and sink terms in the energy conservation equation. This section ends with a brief exposition of analytical models for plasma expansion, preparing ourselves for the next chapters.

1.3.1   From plasma particle distributions to a fluid approach

1.3.1.a   Macroscopic transport equations

In the previous section, the Boltzmann equation was introduced and its equilibrium solution was discussed. While in principle the distribution function for a system not in equilibrium can be obtained from the Boltzmann equation, this is generally a difficult task. In this section, an alternate method will be discussed for determining physical macroscopic variables without explicitly solving the Boltzmann equation. Differential equations governing the temporal and spatial variation of these macroscopic variables will be derived, which are known as macroscopic transport equations. Similar to how the moments of the distribution function gave us macroscopic variables such as number density and average velocity in Sec. 1.2.3, the transport equations are obtained by taking moments of the Boltzmann equation. Looking forward, the first three (velocity) moments of the Boltzmann equation will result

in the equations of conservation of (i) mass (zeroth moment), (ii) momentum (first moment) and (iii) energy (second moment). Additionally, the calculation of each moment will introduce a new variable, which is described by the equation from the next higher order moment. For example, the mass conservation equation will contain velocity, which can only be solved using the momentum conservation equation. Therefore, it is necessary to truncate the system of transport equations (as done here at the second velocity moment). Lastly, since a plasma is composed of multiple particle species, a system of transport equations exists for each species.

Now the method of calculating moments is applied to the Boltzmann equation (as introduced in Eq. (1.6)): the Boltzmann equation is multiplied by a function $\chi(\vec{v})$ (which may depend on velocity $\vec{v}$) and integrated over velocity space. The result is an equation for the dynamics of the average value of this function, in other words, the temporal and spatial variation of a physically relevant macroscopic variable [35]. For brevity, consider the derivation using a general $\chi(\vec{v})$, which gives the following equation based on the collisional Boltzmann equation

$$\int_v \chi(\vec{v}) \frac{\partial f}{\partial t} \mathrm{d}^3 v + \int_v \chi(\vec{v}) \vec{v} \bullet \nabla_r f \mathrm{d}^3 v$$
$$+ \int_v \chi(\vec{v}) \vec{a} \bullet \nabla_v f \mathrm{d}^3 v = \int_v \chi(\vec{v}) \left(\frac{\delta f(\vec{r}, \vec{v}, t)}{\delta t} \right)_{\mathrm{coll}} \mathrm{d}^3 v. \quad (1.16)$$

This can be simplified [35] by noting that the limits of integration do not depend on space or time, $\chi(\vec{v})$ does not depend on $\vec{r}$ or t, and $\vec{r}$, $\vec{r}$ and t are independent variables. Moreover, it is assumed that (i) each force component F_i is independent of the corresponding velocity component v_i and (ii) that the distribution function f tends to zero when the velocity becomes infinitely large (as was stated above). The result is

$$\frac{\partial}{\partial t} \left(\int_v \chi f \mathrm{d}^3 v \right) + \nabla_r \bullet \left(\int_v \chi \vec{v} f \mathrm{d}^3 v \right)$$
$$- \int_v f \vec{a} \bullet \nabla_v \chi \mathrm{d}^3 v = \int_v \chi(\vec{v}) \left(\frac{\delta f}{\delta t} \right)_{\mathrm{coll}} \mathrm{d}^3 v, \quad (1.17)$$

which can be stated in a simpler form using the notation introduced in Eq. (1.11) for the average value of a variable $\chi(\vec{v})$ as

$$\frac{\partial}{\partial t} \left(n \langle \chi \rangle \right) + \nabla_r \bullet \left(n \langle \chi \vec{v} \rangle \right) - n \langle \vec{a} \bullet \nabla_v \chi \rangle = \left[\frac{\delta}{\delta t} \left(n \langle \chi \rangle \right) \right]_{\mathrm{coll}}. \quad (1.18)$$

1.3.1.b   Mass conservation

For the derivation of the first macroscopic transport equation, let us consider particle mass, $\chi(\vec{\mathbf{v}}) = m$, which leads to

$$\frac{\partial}{\partial t}\left(n\left\langle m\right\rangle\right) + \nabla_r \bullet \left(n\left\langle m\vec{\mathbf{v}}\right\rangle\right) - n\left\langle \vec{\mathbf{a}} \bullet \nabla_v m\right\rangle \qquad = \left[\frac{\delta}{\delta t}(n\left\langle m\right\rangle)\right]_{\text{coll}},$$

$$\frac{\partial}{\partial t}\left(nm\right) + \nabla_r \bullet \left(nm\vec{\mathbf{u}}\right) \qquad = \left[\frac{\delta}{\delta t}(nm)\right]_{\text{coll}},$$

$$\frac{\partial \rho}{\partial t} + \nabla_r \bullet \left(\rho\vec{\mathbf{u}}\right) \qquad = \left[\frac{\delta\rho}{\delta t}\right]_{\text{coll}} \qquad (1.19)$$

where $\rho = mn$ is the mass density. This equation is known as the continuity equation, the mathematical statement for conservation of mass. The right-hand side of the equation is the collision term and represents the rate per unit volume at which particles are produced or lost as a result of collisions. Note that the continuity equation can also be derived using the method of fluid dynamics: the change in the amount of mass in a certain volume must equal the mass flow through the surface bounding that volume (in general, combined with any production or loss of particles due to, e.g., collisions). This is closely related to the concept of flux, the quantity $\rho\vec{\mathbf{u}}$ can be called the mass flux or mass transport rate per unit area, i.e., the amount of mass flowing through a surface (perpendicular to the direction of $\vec{\mathbf{u}}$) per unit time per unit area.

1.3.1.c   Momentum conservation

Next, based on the general form derived in Eq. (1.18), consider the first moment: $\chi(\vec{\mathbf{v}}) = m\vec{\mathbf{v}}$. The previously introduced partitioning of particle velocity into average flow velocity and random thermal velocity is used, $\vec{\mathbf{v}} = \vec{\mathbf{c}} + \vec{\mathbf{u}}$, and one may note that $\left\langle \vec{\mathbf{c}}\right\rangle = 0$. The result is

$$\frac{\partial}{\partial t}\left(n\left\langle m\vec{\mathbf{v}}\right\rangle\right) + \nabla_r \bullet \left(n\left\langle m\vec{\mathbf{v}}\vec{\mathbf{v}}\right\rangle\right) - n\left\langle \vec{\mathbf{a}} \bullet \nabla_v(m\vec{\mathbf{v}})\right\rangle \quad = \left[\frac{\delta}{\delta t}(n\left\langle m\vec{\mathbf{v}}\right\rangle)\right]_{\text{coll}}, \quad (1.20)$$

$$\rho\frac{\partial \vec{\mathbf{u}}}{\partial t} + \vec{\mathbf{u}}\frac{\partial \rho}{\partial t} + \nabla_r \bullet (\rho\vec{\mathbf{u}}\vec{\mathbf{u}} + \rho\left\langle \vec{\mathbf{c}}\vec{\mathbf{c}}\right\rangle) - n\left\langle \vec{\mathbf{F}}\right\rangle \qquad = \left[\frac{\delta(\rho\vec{\mathbf{u}})}{\delta t}\right]_{\text{coll}}. \qquad (1.21)$$

The third term can be rewritten as follows: the expression $\rho\left\langle \vec{\mathbf{c}}\vec{\mathbf{c}}\right\rangle$ is known as the kinetic pressure dyad (or tensor) $\mathcal{P}$. The expression $-\nabla \bullet \mathcal{P}$ represents the force exerted in a unit volume of plasma due to variations of the random particle velocities,

which combines scalar pressure and tangential shear forces. The effect of viscosity is relatively unimportant in plasma due to the low densities. So the non-diagonal terms of $\mathcal{P}$ can be neglected. Moreover, assuming that the distribution of random velocities is isotropic, the diagonal terms of $\mathcal{P}$ are equal, and the following simplification in the equation can be made,

$$\nabla \bullet \left(\rho \vec{c}\vec{c} \right) = \nabla \bullet \mathcal{P} = \nabla p, \tag{1.22}$$

where p is the scalar kinetic pressure. Pressure p introduced here plays an important role in gas dynamics, i.e., compressible inviscid flow. An equation-of-state, as discussed in Sec. 1.5, defines a relation between pressure and density ρ for closure of the system of equations. The first part of the third term, $\nabla \bullet \left(\rho \vec{u}\vec{u} \right)$, can be rewritten as

$$\rho \left(\vec{u} \bullet \nabla \right) \vec{u} + \vec{u} \nabla \bullet \left(\rho \vec{u} \right), \tag{1.23}$$

where one can recognize a term of the continuity equation, such that substitution leads to

$$\rho \left(\vec{u} \bullet \nabla \right) \vec{u} + \vec{u} \left(\left[\frac{\delta \rho}{\delta t} \right]_{\text{coll}} - \frac{\partial \rho}{\partial t} \right). \tag{1.24}$$

The simplified form of the momentum transport equation now becomes

$$\rho \left[\frac{\partial}{\partial t} + \left(\vec{u} \bullet \nabla \right) \right] \vec{u} + \nabla p - n \left\langle \vec{F} \right\rangle = \left[\frac{\delta (\rho \vec{u})}{\delta t} \right]_{\text{coll}} - \vec{u} \left[\frac{\delta \rho}{\delta t} \right]_{\text{coll}}. \tag{1.25}$$

Note that the operator in square brackets in the first term can be interpreted as the time variation observed in a reference frame moving with the average flow velocity $\vec{u}$. In case the electromagnetic Lorentz force is considered, the force term $\langle \vec{F} \rangle$ becomes $q(\vec{E} + \vec{u} \times \vec{B})$, where the fields $\vec{E}$ and $\vec{B}$ represent smoothed macroscopic fields. Lastly, the right-hand side vanishes under the assumption that neither the number of particles nor their momentum changes during collisions. The second statement is particularly applicable to elastic collisions between identical particles.

1.3.1.d Energy conservation

The third equation is derived from the second velocity moment, $\chi(\vec{\mathbf{v}}) = \frac{1}{2}mv^2$, the particle kinetic energy.

$$\frac{\partial}{\partial t}\left(n\left\langle\frac{1}{2}mv^2\right\rangle\right) + \nabla_r \bullet \left(n\left\langle\frac{1}{2}mv^2\vec{\mathbf{v}}\right\rangle\right)$$

$$-n\left\langle\vec{\mathbf{a}} \bullet \nabla_v\left(\frac{1}{2}mv^2\right)\right\rangle \quad = \left[\frac{\delta}{\delta t}\left(n\left\langle\frac{1}{2}mv^2\right\rangle\right)\right]_{\text{coll}},$$

$$\frac{\partial}{\partial t}\left(\frac{1}{2}\rho\left(\left\langle c^2\right\rangle + u^2\right)\right) + \nabla_r \bullet \left(\frac{1}{2}\rho\left\langle v^2\vec{\mathbf{v}}\right\rangle\right)$$

$$-n\left\langle\vec{\mathbf{F}} \bullet \vec{\mathbf{v}}\right\rangle \quad\quad = \left[\frac{\delta}{\delta t}\left(\frac{1}{2}\rho\left\langle v^2\right\rangle\right)\right]_{\text{coll}} \quad (1.26)$$

The expression in the second term can be expanded further by recognizing that $\left\langle v^2\vec{\mathbf{v}}\right\rangle = \left\langle(\vec{\mathbf{v}} \bullet \vec{\mathbf{v}})\vec{\mathbf{v}}\right\rangle$ and remembering that $\vec{\mathbf{v}} = \vec{\mathbf{c}} + \vec{\mathbf{u}}$:

$$\frac{1}{2}\rho\left\langle(\vec{\mathbf{v}} \bullet \vec{\mathbf{v}})\vec{\mathbf{v}}\right\rangle = \frac{1}{2}\rho\left(u^2\vec{\mathbf{u}} + \left\langle c^2\right\rangle\vec{\mathbf{u}} + 2\left\langle\vec{\mathbf{c}}\vec{\mathbf{c}}\right\rangle \bullet \vec{\mathbf{u}} + \left\langle c^2\vec{\mathbf{c}}\right\rangle\right)$$

$$= \frac{1}{2}\rho u^2\vec{\mathbf{u}} + \frac{1}{2}\rho\left\langle c^2\right\rangle\vec{\mathbf{u}} + \rho\left\langle\vec{\mathbf{c}}\vec{\mathbf{c}}\right\rangle \bullet \vec{\mathbf{u}} + \frac{1}{2}\rho\left\langle c^2\vec{\mathbf{c}}\right\rangle$$

$$= \frac{1}{2}\rho u^2\vec{\mathbf{u}} + \frac{1}{2}\rho\left\langle c^2\right\rangle\vec{\mathbf{u}} + p\vec{\mathbf{u}} + \vec{\mathbf{q}} \quad\quad (1.27)$$

where the expression for the kinetic pressure dyad is used in its non-viscous isotropic form $\rho\left\langle\vec{\mathbf{c}}\vec{\mathbf{c}}\right\rangle = \mathcal{P} = p\mathbb{1}$ and the heat flux vector $\vec{\mathbf{q}} = \frac{1}{2}\rho\left\langle c^2\vec{\mathbf{c}}\right\rangle$ is introduced.

Let us introduce the following notation $E = \frac{1}{2}\left(\left\langle c^2\right\rangle + u^2\right)$ and insert the expression of Eq. (1.27) into the energy transport equation (Eq. (1.26)), which then reads

$$\frac{\partial}{\partial t}(\rho E) + \nabla_r \bullet \left((\rho E + p)\vec{\mathbf{u}}\right) + \nabla_r \bullet \vec{\mathbf{q}}$$

$$-n\left\langle\vec{\mathbf{F}} \bullet \vec{\mathbf{v}}\right\rangle \quad = \left[\frac{\delta}{\delta t}\left(\frac{1}{2}\rho\left\langle v^2\right\rangle\right)\right]_{\text{coll}} \quad (1.28)$$

1.3.2 Single-fluid, single-temperature approach

In the previous section, the derivation of the fluid equations from kinetic theory was discussed. For brevity, the types of particles described by the equations were not specified. Each species in the plasma (ions of different charge states, electrons and atoms) can, in theory, be described by its own fluid equation. The various 'fluids'

are then coupled through the force term and the (right-hand side) interaction term. Such a large system of equations is very difficult to solve.

A simplified approach is provided by the two-fluid model, in which both ions and electrons are treated. The ion fluid may be assigned a fixed charge state [36] for simplification. In this approach the two sets of fluid equations are coupled through self-consistent electromagnetic fields, i.e., the force term equals the Lorentz force combined with the charge and current density incorporating both ion and electron number densities.

In the remainder of this section, arguments are given that the plasma can be treated as a single fluid for our applications. A single-fluid approach is based on a system of equations as derived in the previous section, those of a single particle species. In a plasma context, one can think of the ions and electrons behaving in unison. This is due to the frequent collisions in the hot, dense plasmas conditions in laser-produced plasma [37]. Moreover, this approach builds on the assumption of quasi-neutrality, which is captured in a relation between electron and ion density: $n_e = Z n_i$, where Z denotes the average charge state of the plasma ions. In a quasi-neutral plasma, electromagnetic fields are neglected in the fluid equations. Quasi-neutrality holds when the following criterion is satisfied: the local Debye length, as given in Eq. (1.4), must be significantly smaller than the length scale of the plasma flow. In formula form, $\lambda_D \ll n_i / |\nabla n_i|$.

In the single-fluid approach, one property of ions and electrons still plays a fundamental role. The mass ratio between (tin) ions and electrons equals $m_{Sn}/m_e \approx 10^5$, which has two effects: (i) fluid density is determined by the ion number density, (ii) fluid temperature is in the first place dependent on the electrons. The second assumption is due to both the larger electron mobility and the absorption mechanism of laser irradiation being inverse Bremsstrahlung.

The limitations to the approach lie in the breakdown of the two assumptions, frequent collisions and quasi-neutrality. The collision rate is dependent on the density of particles, so care must be taken in low density conditions, such as during plasma expansion over larger distances. Specifically for laser-produced plasma, a high laser intensity can break quasi-neutrality as the laser energy is absorbed by the electrons, which consequently are accelerated to large kinetic energies. When electrons leave the material with their acquired speeds, an electric field is also established, both being effects not captured in a single-fluid model [36].

The temperature of the fluid is a measure of the random thermal motion of its constituents. In a (more general) two-fluid model, the ion and electron fluid are both assigned a temperature.

In the model discussed here, a single temperature is used in the description of the single fluid. In low-density plasma conditions, one may consider this equivalent to an electron temperature only, effectively assuming a zero temperature for the ion fluid. Due to their large relative mass (to the electron mass), ions may be assumed to be stationary on the timescales in which electrons are able to react.

The timescale over which thermal energy is transferred from the electrons to the ions is dependent on the ion–electron collision rate, its classical expression will be stated in Eq. (1.44). Therefore, in high-density conditions, the implied assumption of zero ion temperature is no longer applicable. In the high-density plasma conditions of the laser-produced plasmas considered, the ions attain the same temperature as the electrons, which defines the temperature of the fluid T

$$T_{\mathrm{e}} = T_{\mathrm{ion}} = T. \tag{1.29}$$

Based on the quasi-neutrality condition, the contribution of the electrons to the pressure is higher by a factor Z, the average charge state. For moderate ionization degrees, $Z \approx 11 - 15$, its contribution to the pressure outweighs the ionic contribution. This is important as the pressure which drives the expansion dynamics in the hydrodynamic framework.

Summarizing, the two-fluid description of a quasi-neutral plasma with an electron temperature that equals the ion temperature reduces to the gas-dynamic equations [38]. The use of gas dynamics to model the plasma expansion is justified by the dominant effect of the pressure gradient in the expansion of the plasma plume.

1.4   System of equations underlying the fluid simulations

This section introduces the set of (fluid) equations underlying the radiation-hydrodynamic simulations presented in this thesis. The simulations are performed with the code RALEF-2D, which solves the single-fluid single-temperature equations in two spatial dimensions. RALEF-2D, acronym for Radiative Arbitrary Lagrange–Eulerian Fluid dynamics in 2D, combines hydrodynamics with energy transport by heat conduction and radiation transport, which will be introduced in the following subsections.

The system of fluid equations solved in RALEF-2D is derived from Eq. (1.19, 1.25 and 1.28) including the assumptions of single-fluid single-temperature modeling. This corresponds to neglecting shear stresses due to viscosity, electromagnetic

fields (therefore $\vec{\mathbf{F}} = 0$) and any influence of particle collisions. The effects of particle collisions were captured by the $\left[\delta(n\langle\chi\rangle)/\delta t\right]_{\text{coll}}$ terms in the macroscopic transport equations and are zero under the assumption of elastic collisions between identical particles, where no particles are produced or lost.

The first equation is the continuity equation (conservation of mass), introduced in Eq. (1.19), without the collision term on the right-hand side. The form of the second equation is simplified after neglecting viscosity and shear forces in the fluid (such that only ∇p remains) and follows directly from the first two terms of Eq. (1.20). For the third equation, terms describing energy transport need to be introduced. The shown derivation already includes $Q_{\text{T}} = -\nabla_r \cdot \vec{\mathbf{q}}$, a source term due to thermal conduction that follows from the heat flux, i.e., the transport of random thermal motion. Additionally, a source term is included due to energy transport by thermal radiation, Q_{rad}, and a term Q_{dep} describing the volume-specific heating power by external energy sources, e.g., energy deposition by a laser beam.

For reference, the system of RALEF-2D's fluid equations can be summarized as

$$\frac{\partial \rho}{\partial t} + \qquad \nabla_r \cdot \left(\rho \vec{\mathbf{u}}\right) \qquad\qquad = 0, \tag{1.30}$$

$$\frac{\partial (\rho \vec{\mathbf{u}})}{\partial t} + \qquad \nabla_r \cdot \left(\rho \vec{\mathbf{u}}\vec{\mathbf{u}}\right) + \nabla p \qquad = 0, \tag{1.31}$$

$$\frac{\partial (\rho E)}{\partial t} + \qquad \nabla_r \cdot \left((\rho E + p)\vec{\mathbf{u}}\right) \qquad = Q_{\text{T}} + Q_{\text{rad}} + Q_{\text{dep}}. \tag{1.32}$$

Here, in RALEF-2D terminology, $E = e + u^2/2$ denotes the mass-specific total energy, summing internal and kinetic contributions ($e = \frac{1}{2}\langle c^2\rangle$ is identified in the E term introduced in Eq. (1.28)).

1.4.1 Heat conduction

The first volume-specific power term in the fluid energy equation (Eq. (1.32)), Q_{T}, follows directly from the derivation from kinetic theory. It is found that $Q_{\text{T}} = -\nabla_r \cdot \vec{\mathbf{q}}$, with the heat flow vector (or heat flux) $\vec{\mathbf{q}} = \frac{1}{2}\rho\langle c^2 \vec{\mathbf{c}}\rangle$ in kinetic theory notation. However, for further implementation in the fluid equations, the heat flow is directly related to the (negative) temperature gradient by

$$Q_{\text{T}} = -\nabla_r \cdot \vec{\mathbf{q}} \tag{1.33}$$

$$\vec{\mathbf{q}} = -\kappa \nabla T \tag{1.34}$$
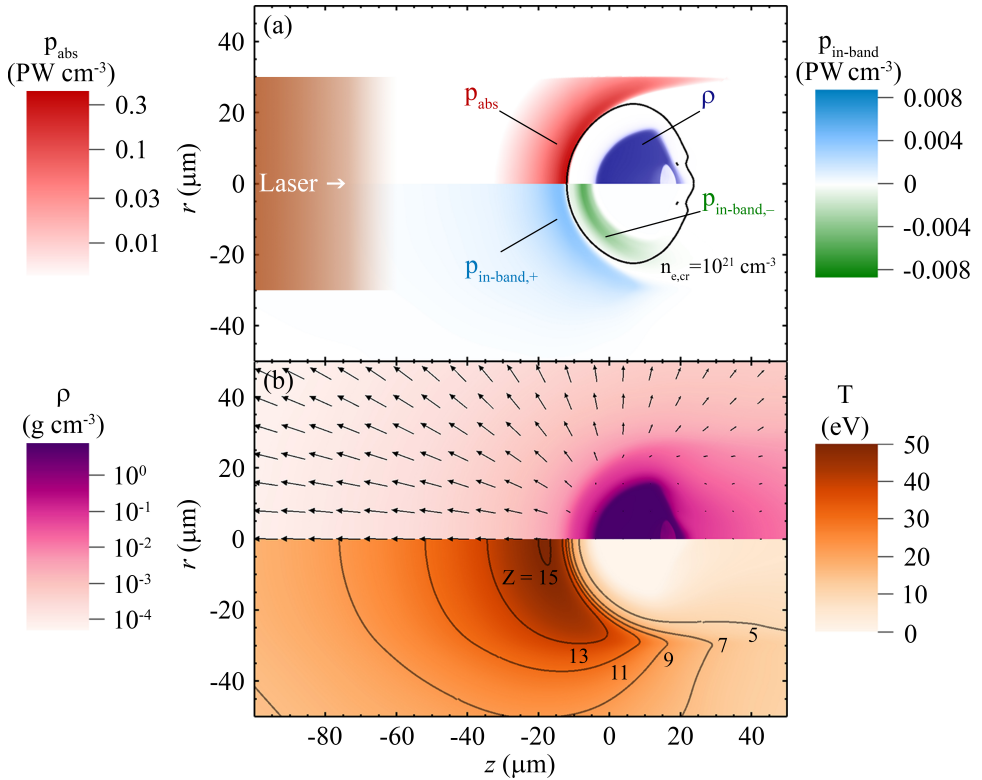
Figure 1.1: Collection of physical quantities in a typical radiation-hydrodynamic simulation: illumination of a tin microdroplet, 30 μm in diameter, by a $\lambda_{laser} = 1.064$ μm laser beam with a beam width of 60 μm. (a) The instantaneous (at $t = 18$ ns) volume-specific laser deposition rate [39] p_{abs} (red) and in-band radiative power $p_{in\text{-}band}$ (light blue – green). The critical electron density (black contour) and fluid density ρ (dark blue) are indicated. (b) The fluid density ρ (log-scale, purple) and temperature T (orange) with superimposed velocity vectors and contours of average charge state Z.

where $\kappa(\rho, T)$ denotes the heat conduction coefficient, which is evaluated for each fluid element. In the RALEF-2D simulations performed in this thesis, $\kappa(\rho, T)$ is taken from pre-tabulated data generated by the THERMOS code [40, 41]. Equation (1.34) is also known as the differential form of Fourier's law of thermal conduction. Conceptually, it means that heat is transferred from hot regions to cold regions in the fluid, i.e., in the opposite direction of the temperature gradient.

1.4.2 Radiation transport

The second term in Eq. (1.32), corresponding to energy transport by thermal radiation, is more involved. It signifies an important part of *radiation*-hydrodynamic simulations. Radiation transport is essential to the formation of the radiating plasmas investigated in this thesis, as plasmas consisting of heavy weight (high atomic number) ions are known to display large energy losses through radiation [42]. The term in Eq. (1.32) is defined by

$$Q_{\text{rad}} = -\nabla_r \bullet \vec{\mathbf{q}}_{\text{rad}} \tag{1.35}$$

$$\vec{\mathbf{q}}_{\text{rad}} = \int_0^\infty d\nu \int_{4\pi} I_\nu \vec{\mathbf{\Omega}} \, d\vec{\mathbf{\Omega}}. \tag{1.36}$$

Note that the definition of Q_{rad} is similar to Q_{T} in that it is the divergence of an energy flux [43]. As given by Eq. (1.36), the radiation energy flux $\vec{\mathbf{q}}_{\text{rad}}$ is found by the integration of the spectral radiation intensity I_ν over the full solid angle and all photon frequencies $0 < \nu < \infty$. In general, the spectral intensity $I_\nu(t, \vec{\mathbf{x}}, \vec{\mathbf{\Omega}}, \nu)$ satisfies the following transfer equation

$$\frac{1}{c}\frac{\partial I_\nu}{\partial t} + \vec{\mathbf{\Omega}} \bullet \nabla_r I_\nu = \eta_\nu - k_\nu I_\nu = k_\nu \left(\frac{\eta_\nu}{k_\nu} - I_\nu \right) \tag{1.37}$$

$$\overset{\text{LTE}}{=} k_\nu (B_\nu - I_\nu). \tag{1.38}$$

In this equation, $\vec{\mathbf{\Omega}}$ denotes the propagation direction of a photon with frequency ν; $\eta_\nu(\nu, \rho, T)$ and $k_\nu(\nu, \rho, T)$ are the spectral emission and absorption coefficients, respectively, corrected for induced emission, and $B_\nu(\nu, \rho, T)$ is the radiation source function. The possible role of scattering is ignored. The quasi-static approximation is used, where the first (time-derivative) term is neglected. This is justified as long as the characteristic timescale of any variation of the fluid variables greatly exceeds the ratio of the characteristic size of the simulation region and the speed of light c. This form is written under the assumption that at each time a negligible amount of energy resides in the radiation field (i.e., negligible heat capacity), so the energy radiated by a fluid element is assumed to be either instantaneously reabsorbed by other fluid elements or lost from the system. From the point of view of fluid dynamics, radiation transport acts as non-local heat transport. Another assumption is that no momentum is transferred by radiation, i.e., radiation pressure can be ignored [44]. Our work is based on the LTE (Local Thermodynamic Equilibrium) form given in Eq. (1.38), where the source function equals the blackbody spectral Planckian intensity given

by

$$B_\nu(\rho, T) = \frac{2h\nu^3}{c^2} \frac{1}{\exp(h\nu/T) - 1}, \tag{1.39}$$

where h denotes the Planckian constant and c the speed of light. Note that, since B_ν does not depend on $\vec{\Omega}$, integrating over the full solid angle results in $4\pi B_\nu$. Now, using Eq. (1.38), the radiative source term (Eq. (1.35)) can be written as

$$
\begin{aligned}
Q_{\text{rad}} &= -\nabla_r \bullet \left(\int_0^\infty d\nu \int_{4\pi} I_\nu \vec{\Omega} \, d\vec{\Omega} \right) &&= -\int_0^\infty d\nu \int_{4\pi} \nabla_r \bullet \left(I_\nu \vec{\Omega} \right) \, d\vec{\Omega} \\
&= -\int_0^\infty d\nu \int_{4\pi} \vec{\Omega} \bullet \nabla_r I_\nu \, d\vec{\Omega} &&= \int_0^\infty k_\nu \left(\int_{4\pi} I_\nu d\vec{\Omega} - 4\pi B_\nu \right) d\nu.
\end{aligned}
\tag{1.40}
$$

The implementation in RALEF-2D is based on using pre-tabulated absorption coefficients, again generated by the THERMOS code [40, 41].

1.4.3   Laser propagation and absorption

Just as thermal radiation transport is fundamental to radiation-hydrodynamic modeling, laser–plasma modeling demands considering an external energy source corresponding to the laser. More precisely, the deposition of laser energy in the plasma needs to be included, i.e., laser absorption. Importantly, the deposited power depends on the state of the plasma, i.e., its density and temperature. The previously introduced critical electron density is a central concept for laser absorption in an LPP. Namely, laser absorption will take place up to the critical surface, assuming a generic increasing electron density profile seen by the laser.

Our simulations employ the hybrid refractive/reflective model of laser light transport implemented in RALEF-2D. The hybrid feature entails combining the approximation of geometric optics with the wave theory of light. Geometric optics is employed in plasma regions with electron densities below the critical electron density, while wave optics is used close to the critical surface. The implementation is based on the complex dielectric permittivity $\varepsilon_\omega = \varepsilon(\omega)$.

1.4.3.a   Complex dielectric permittivity

The complex dielectric permittivity is generally defined in the context of electric induction in a material by an electrical field, where it represents the proportionality factor between the induction and the magnitude of the applied electric field. Based

on the wave theory of light, it may be applied to the interaction of electromagnetic light waves with a material. Note that it will be heavily dependent on the local properties of the material, and in our application ε_ω is continuously changing. As reflected in the given functional form, the response to external fields generally depends on the frequency of the field, ω. It is assumed that the relevant timescale ω^{-1} is much shorter than any timescale of hydrodynamic motion or kinetic relaxation in the plasma. Our present description also remains within the framework of linear optics, i.e., the complex dielectric permittivity does not depend on laser intensity. The scalar complex dielectric permittivity at frequency ω may be split into real and imaginary parts, and is related to the complex refractive index by

$$\varepsilon_\omega = \varepsilon'_\omega + i\varepsilon''_\omega \tag{1.41}$$

$$\mathbf{n} = c\sqrt{\mu\varepsilon_\omega} \tag{1.42}$$

where c denotes the speed of light and μ is the magnetic permeability of the material. The complex refractive index $\mathbf{n}$ can also be split into a real and imaginary part, $\mathbf{n} = n + i\kappa$, where n is the refractive index and κ is called the extinction coefficient. Knowledge of ε_ω, therefore, allows one to calculate the propagation of laser light through a medium.

In our simulations, an equation for ε_ω is used derived from the Drude model applied to a plasma, which is given by

$$\varepsilon_\omega = 1 - \frac{\omega_{\mathrm{pe}}^2}{\omega(\omega + i\nu_{\mathrm{ei}})} \tag{1.43}$$

where ω_{pe} is the plasma frequency (or resonance frequency) for free electrons (as given before in Eq. (1.1)) and ν_{ei} is the electron–ion collision frequency.

The classical expression for the electron–ion collision frequency, assuming infinitely heavy point-like ions, is given by [45]

$$\nu_{\mathrm{ei}} = \frac{4\sqrt{2\pi}}{3} \frac{e^4 n_{\mathrm{i}} z_{\mathrm{ion}}^2}{m_{\mathrm{e}}^{1/2} T_{\mathrm{e}}^{3/2}} \ln\Lambda, \tag{1.44}$$

where $\ln\Lambda$ denotes the Coulomb logarithm. The Coulomb logarithm, typically $\ln\Lambda \approx 10 - 20$, describes the scattering of particles in the electric field of another particle [46]. As common in plasmas, the cumulative effect of small-angle collisions exceeds the effect of large-angle collisions. The Coulomb logarithm quantifies the effectiveness of small-angle over large-angle collisions.

The Drude model is an application of kinetic theory and describes the behavior of electrons in a metal as a gas of detached free electrons moving on top of a fixed background of ions [32, 47]. The form of Eq. (1.43) can be simplified in the limit $\varepsilon_\omega'' \ll |\varepsilon_\omega'|$, corresponding to $\nu_{ei} \ll \omega$. This results in an equation for the cold-plasma permittivity,

$$\varepsilon_\omega = 1 - \omega_{pe}^2/\omega^2, \tag{1.45}$$

$$= 1 - \frac{n_e}{n_{e,cr}} = 1 - \bar{n}_e. \tag{1.46}$$

1.4.3.b   Geometric optics approach

The geometric optics approximation of ray tracing is adopted in the underdense plasma. More precisely, it is based on the assumptions that, for a given laser wavelength λ (i) the characteristic spatial scale of plasma parameter variation is much larger than λ and (ii) that the attenuation of the laser beam over a distance of λ is weak, i.e., $\kappa \ll 1$. It has several advantages, such as simplicity of implementation, low computational costs, as well as the ability to describe refraction [39].

In the ray tracing model [39, 48], the incident monochromatic laser beam is represented by numerous infinitely thin elementary rays. As the laser enters the underdense region (for a typical case), the geometric optics approximation applies. The geometric-optics trajectory $\vec{x}_r(\xi)$ of a ray r can be found as a solution of the equation

$$\frac{d^2\vec{x}_r}{d\xi^2} = \frac{1}{2}\nabla\varepsilon_\omega, \tag{1.47}$$

$$= -\frac{1}{2}\nabla\bar{n}_e, \tag{1.48}$$

where $\xi = ct$ is a positional parameter along the ray trajectory. In the second line, the cold-plasma permittivity is used, given in Eq. (1.45), in line with the applicability condition of geometric optics. Let $P_r(\xi)$ denote the power carried by a single elementary ray, its attenuation can then be calculated from

$$\frac{dP_r}{d\xi} = -\frac{\omega}{c}\varepsilon_\omega'' P_r, \tag{1.49}$$

which is also based on the approximation that $\nu_{ei} \ll \omega$.

However, the applicability of ray tracing, based on geometric optics, is violated in the vicinity of the critical surface. In more detail, besides the inability to describe diffraction, it does not reproduce reflection, transmission and absorption of laser light by overdense plasma layers. Moreover, it does not distinguish between *s*- and *p*-polarizations for oblique incidence [39]. Therefore, one requires a treatment beyond geometrical optics for the treatment of these physical effects, as will be discussed in the next section.

1.4.3.c   Wave optics approach

The propagation of a monochromatic planar wave across a planar layer with increasing density, in other words, laser beam illumination of a plasma layer, can be described with wave optics theory [39]. For simplicity, assume that the complex dielectric permittivity varies only along the *z* axis, perpendicular to the plasma layer, leading to a 1D wave equation. Upon reaching the plasma layer, the incoming wave is split into a reflected and a transmitted wave. In the following, the propagation through the plasma layer of the transmitted wave is calculated. Importantly, energy is dissipated during the propagation, i.e., laser light is absorbed in the plasma layer. The electromagnetic field splits into two mutually fully independent waves (normal modes): *s*-polarized and *p*-polarized waves. Their propagation is described by the Helmholtz equation, the time-independent form of the wave equation. The permittivity at entrance of the layer is denoted ε_0 and the angle of incidence is denoted θ_0, which is the angle between the incoming wave vector and the *z*-axis. For the *s*-polarized wave, it reduces to the following form in the considered one-dimensional case,

$$\frac{c^2}{\omega^2}\frac{d^2 E}{dz^2} + (\varepsilon_\omega - \varepsilon_0^2 \sin^2\theta_0)E = 0, \tag{1.50}$$

$$H = -i\frac{c}{\omega}\frac{dE}{dz},$$

for electric field strength E and magnetic field strength H, which satisfies $H = B/\mu_0$. For the *p*-polarized wave one can find

$$\frac{c^2}{\omega^2}\frac{d}{dz}\left(\frac{1}{\varepsilon_\omega}\frac{dH}{dz}\right) + \left(1 - \frac{\varepsilon_0^2 \sin^2\theta_0}{\varepsilon_\omega}\right)H = 0, \tag{1.51}$$

$$E = \frac{i}{\varepsilon_\omega}\frac{c}{\omega}\frac{dH}{dz}.$$

In the performed simulations, circularly polarized laser light is chosen by setting the *s*-polarization fraction to one half.

Energy dissipation (absorption) by monochromatic fields, like a laser beam, can be quantified based on the magnitude of the electromagnetic fields. For a quasi-homogeneous medium, one can derive [43] that the Poynting vector of the electromagnetic energy flux $\vec{\mathbf{S}}_\omega$ (in the direction of unit vector $\vec{\mathbf{e}}$) and the rate of energy dissipation per unit volume Q_ω take the form

$$\vec{\mathbf{S}}_\omega = \frac{c}{8\pi} n \left|\vec{\mathbf{E}}\right|^2 \vec{\mathbf{e}}, \tag{1.52}$$

$$Q_\omega = \frac{\omega}{8\pi} \varepsilon''_\omega \left|\vec{\mathbf{E}}\right|^2, \tag{1.53}$$

respectively. Consequently, an expression can be derived for the absorption coefficient,

$$k_{\text{abs}} = \frac{Q_\omega}{\left|\vec{\mathbf{S}}_\omega\right|} = \frac{\omega}{c} \frac{\varepsilon''_\omega}{n} = \frac{2\omega}{c} \kappa, \tag{1.54}$$

which is dependent on the complex dielectric permittivity or, equivalently, the complex refractive index of the medium. In the more general case of an inhomogeneous planar layer, the rate of energy dissipation takes the following forms for *s*- and *p*-polarization, respectively,

$$Q_\omega = \frac{\omega}{8\pi} \varepsilon''_\omega \left|\vec{\mathbf{E}}\right|^2, \qquad\qquad \text{\textit{s}-polarization} \tag{1.55}$$

$$Q_\omega = \frac{\omega}{8\pi} \varepsilon''_\omega \left(\left|\vec{\mathbf{E}}\right|^2 + \varepsilon_0^2 \sin^2 \theta_0 \left|\frac{H}{\varepsilon_\omega}\right|^2 \right), \qquad \text{\textit{p}-polarization} \tag{1.56}$$

for an angle of incidence θ_0 with respect to the *z* axis.

The Kramers inverse-bremsstrahlung absorption coefficient for a plasma of hydrogen-like ions (with charge $z_{\text{ion}}e$) is given by [49]

$$k_\nu(\nu, T_e) = \frac{32\pi^3}{3\sqrt{6\pi}} \alpha a_0^5 \left(\frac{e^2/a_0}{T_e} \right) \left(\frac{e^2/a_0}{h\nu} \right) \left(1 - \exp^{-h\nu/T} \right) n_e n_i z_{\text{ion}}^2 \bar{g}, \tag{1.57}$$

where α is the fine structure constant, a_0 is the Bohr radius and $\bar{g}$ is the mean value of the Gaunt factor. To describe the absorption of laser light, the monochromatic

formula in Eq. (1.57) is used in the limit $hv \ll T$, which becomes [43]

$$k_v = K_{ff} \left(\frac{\rho}{A} \right)^2 \frac{z_{ion}^3 \bar{g}}{T^{3/2} v^2}, \qquad (1.58)$$

where $K_{ff} \approx 0.278 \text{ mg}^2/(\text{mm}^5 \text{keV}^{7/2})$ is a numerical constant and the Maxwellian-mean Gaunt factor $\bar{g}$ in the Born approximation, which in the limit $hv \ll T$ is given by

$$\bar{g} = \max \left[1, \frac{\sqrt{3}}{\pi} \ln \left(2.24584 \frac{T}{v} \right) \right]. \qquad (1.59)$$

Equivalently, the Kramers inverse-bremsstrahlung absorption coefficient [50] can also be simplified to the following form [51] in the limit of $hv \ll T$

$$k = \frac{16\pi \sqrt{2\pi}}{3} \frac{e^6 n_e^2 z_{ion}}{c(m_e T)^{3/2} \omega^2} \ln \Lambda. \qquad (1.60)$$

Here the Coulomb logarithm, $\ln \Lambda = \ln \left(4T/\gamma_E hv \right)$, is obtained from the Gaunt factor in the Born approximation (corresponding to the high frequency limit), where $\ln \gamma_E$ denotes Euler's constant.

Lastly, the classical Kramers inverse-bremsstrahlung absorption coefficient (Eq. (1.57)) can also be recovered from the equations introduced in this section [43], in the limit of $v_{ei} \ll \omega$ (and to the accuracy of the value of the Coulomb logarithm). The absorption coefficient based on extinction coefficient κ, given in Eq. (1.54), can be written in terms of the complex refractive index through

$$k_{abs} = \frac{2\omega}{c} \kappa = \frac{2\omega}{c} \sqrt{\frac{1}{2} \left(\sqrt{\varepsilon_\omega'^2 + \varepsilon_\omega''^2} - \varepsilon_\omega' \right)}. \qquad (1.61)$$

The real and imaginary parts of complex refractive index ε_ω (Eq. (1.41)) assuming the Drude model (Eq. (1.43)) equal

$$\varepsilon_\omega' = 1 - \frac{\bar{\omega}_{pe}^2}{1 + \bar{v}_{ei}^2}, \qquad (1.62)$$

$$\varepsilon_\omega'' = \frac{\bar{\omega}_{pe}^2 \bar{v}_{ei}}{1 + \bar{v}_{ei}^2}, \qquad (1.63)$$

where shortened forms $\bar{\nu}_{\text{ei}} = \nu_{\text{ei}}/\omega$ and $\bar{\omega}_{\text{pe}}^2 = \omega_{\text{pe}}^2/\omega^2 = n_{\text{e}}/n_{\text{e,cr}}$ are used.

In the 2D plasma simulations discussed in this thesis, the introduced 1D wave optics theory is implemented by defining the (imaginary) planar layer perpendicular to the gradient of complex dielectric permittivity ε_ω, which coincides with the direction of $\nabla \bar{n}_{\text{e}}$ based on the simplification introduced in Eq. (1.45). The z-axis, where the introduced equations are defined, is represented by the transmitted ray, i.e., in the direction of $\nabla \bar{n}_{\text{e}}$. Therefore, also the 1D profile of complex dielectric permittivity, $\varepsilon_\omega(z)$, is calculated by tracing the transmitted ray across the 2D numerical grid.

1.4.3.d   Hybrid approach

The hybrid approach implemented in the RALEF-2D simulations [39], as introduced above, is based on switching between geometric optics and wave optics treatments. In a typical case, each incoming ray is described by the geometric approach up to a certain point $\mathcal{O}$ in the vicinity of the critical surface. At the point $\mathcal{O}$, the power assigned to the ray is split into reflected and transmitted contributions, and the Helmholtz equation (Eq. (1.50, 1.51)) is solved for the s- and p-polarized components. The angle θ_0 in the Helmholtz equations is defined as the angle between the incoming and transmitted ray. A reflected ray emerges from $\mathcal{O}$ at an angle $\pi - \theta_0$ with respect to the transmitted ray, and is further calculated through geometric optics.

The applicability of the geometric optics approximation (to the general wave optics approach) can be summarized by the following condition,

$$\frac{c}{\omega} \left| \frac{d}{dz} \left(\varepsilon_{\text{cp}} - \varepsilon_0 \sin^2 \theta_0 \right)^{-1/2} \right| \ll 1 \tag{1.64}$$

where the cold-plasma expression ε_{cp} (Eq. (1.45)) is substituted for ε_ω. As the defined z-direction coincides with the $\nabla \bar{n}_{\text{e}}$ vector and $\varepsilon_0 = 1$ holds in the limit $\bar{n}_{\text{e}} \ll 1$, this condition can be rewritten as

$$\lambda \left| \nabla \left(\cos^2 \theta_0 - \bar{n}_{\text{e}} \right)^{-1/2} \right| \geq a, \tag{1.65}$$

$$\bar{n}_{\text{e}} + \left(\frac{\lambda}{2a} |\nabla \bar{n}_{\text{e}}| \right)^{2/3} \geq \cos^2 \theta_0, \tag{1.66}$$

where $a > 0$ is a dimensionless parameter of order unity. The physical interpretation of this condition is that switching to wave optics is enforced if (i) the singular point $\varepsilon_{\text{cp}} = \sin^2 \theta_0$ is approached, which for $|\theta_0| \ll 1$ corresponds to approaching the critical surface, or (ii) the gradient $\nabla \bar{n}_{\text{e}} = -\nabla \varepsilon_{\text{cp}}$ becomes too steep.

At last, the criterion used in the simulations for switching between geometric and wave optics can be summarized as,

$$\bar{n}_{\mathrm{e}} + \beta_{\mathrm{gw}}\lambda\left|\nabla\bar{n}_{\mathrm{e}}\right| \geq \alpha_{\mathrm{gw}}\cos^2\theta_0, \tag{1.67}$$

which is derived from the previous equation by omitting the power 2/3 and introducing an additional free parameter, α_{gw}. For most practical applications, the two user-defined free parameters $0 < \alpha_{\mathrm{gw}} < 1$ and $\beta_{\mathrm{gw}} \simeq 1$ are typically chosen as [39] $0.8 < \alpha_{\mathrm{gw}} < 0.9$ and $\beta_{\mathrm{gw}} = 1$.

1.5 Equation-of-state

The system of fluid equations employed in RALEF-2D, given in Eq. (1.30 – 1.32), was derived from kinetic theory by taking moments of the Boltzmann equation. Each moment provides a transport equation, but also introduces new variables, e.g., Eq. (1.30) includes $\vec{\mathbf{u}}$ and Eq. (1.31) introduces p. This means that the system of equations is not yet closed. This section will discuss means of closing this system of equations by use of an equation-of-state.

1.5.1 Ideal gas law

The ideal gas law is a well-known equation-of-state, given by

$$pV = Nk_{\mathrm{B}}T, \text{or alternatively} \tag{1.68}$$

$$p = nk_{\mathrm{B}}T = \frac{\rho}{m_{\mathrm{ion}}}k_{\mathrm{B}}T, \text{or} \tag{1.69}$$

$$p/\rho = \frac{k_{\mathrm{B}}T}{m_{\mathrm{ion}}} \tag{1.70}$$

for a volume V, number of particles N and the absolute temperature T. Alternative forms are given in terms of the number density n, mass density ρ and ion mass m_{ion}. It describes a theoretical gas of point particles without inter-particle interactions. A real gas can be approximated as an ideal gas under some simplifying assumptions. It is most accurate for monatomic gases at low densities and high temperatures [52]. Under these conditions, the neglect of particle size (point particles) and interparticle interactions is less important. Moreover, absence of interactions may be relaxed to the assumption of perfectly elastic collisions.

The expansion of a non-viscous fluid without thermal transport or collisional effects can be approximated by an ideal gas undergoing an isentropic process [35], i.e., one that is both adiabatic and reversible. Such a process is described by the following equation,

$$pV^{\gamma} = \text{const., or alternatively} \tag{1.71}$$

$$p\rho^{-\gamma} = \text{const.,} \tag{1.72}$$

where the adiabatic index γ is the ratio of specific heats at constant pressure and constant volume. The adiabatic index is related to the number of degrees of freedom, N, of a monatomic gas as $\gamma = (N + 2)/N$. This equation holds for a calorically perfect gas where γ is constant.

For an ideal gas undergoing an isothermal process, $pV = \text{const.}$ can be seen from Eq. (1.68). The functional form of Eq. (1.71) can even be generalized further to the equation for a polytropic process $pV^{n_{\text{poly}}} = \text{const.}$, with polytropic index n_{poly}. This model therefore includes the isentropic process ($n_{\text{poly}} = \gamma$) and isothermal process ($n_{\text{poly}} = 1$) when the ideal gas law also applies, as well as isobaric (constant pressure, $n_{\text{poly}} = 0$) and isochoric (constant volume, $n_{\text{poly}} \to +\infty$) processes.

1.5.2 Speed of sound

As the equation-of-state provides a relation between pressure and density, expressions can be derived for the speed of sound, c_{s}. It corresponds to the speed with which a sound wave travels inside an elastic medium. The speed of sound can be derived from Newton's second law for a pressure-gradient force. The one-dimensional case of a sound wave traveling at a speed v_{sw} in a fluid is considered for simplicity. By change of reference frame, one can equivalently consider fluid flow propagating at a speed v_{sw}, with the sound wave being stationary. Let us consider a compression wave, where the pressure and density inside the wave are higher than the surroundings. The mass flux $j = \rho v_{\text{sw}}$ is constant at any point along the flow by the continuity equation, e.g., $0 = dj/dt = d\rho/dt v_{\text{sw}} + \rho dv_{\text{sw}}/dt$. Therefore, the velocity inside the sound wave must be lower than outside, and the medium will have to decelerate

and then accelerate. The derivation of the speed of sound is based on this accelera-
tion as a result of the pressure gradient. The result is

$$a = \frac{F}{m}, \tag{1.73}$$

$$\frac{dv_{\text{sw}}}{dt} = -\frac{1}{\rho}\frac{dp}{dz}, \tag{1.74}$$

$$\rho\frac{dv_{\text{sw}}}{dt}\frac{dz}{dt} = -\frac{dp}{dz}\frac{dz}{dt}, \tag{1.75}$$

$$-v_{\text{sw}}^2\frac{d\rho}{dt} = -\frac{dp}{dt} = -\frac{dp}{d\rho}\frac{d\rho}{dt}, \tag{1.76}$$

$$c_{\text{s}} = v_{\text{sw}} = \sqrt{\left(\frac{dp}{d\rho}\right)_{\text{s}}}, \tag{1.77}$$

where the derivative is taken isentropically, i.e., at constant entropy. The reason is
that the propagation of a sound wave can be assumed to be an adiabatic process due
to its high speed.

For an ideal gas described by the equation-of-state in Eq. (1.68), the speed of
sound depends only on the temperature and composition of the material. For an
adiabatic process in an ideal gas, as described by Eq. (1.71), the formula for the
adiabatic speed of sound can be derived, which equals

$$c_{\text{s, adiabatic}} = \sqrt{\gamma\frac{k_{\text{B}}T}{m}}. \tag{1.78}$$

This definition is used in Ch. 5 with an adiabatic index of 1.167 following Ref. [53].
The derivation proceeds as

$$c_{\text{s}}^2 = \left(\frac{dp}{d\rho}\right)_{\text{s}} = \gamma\rho^{\gamma-1} = \gamma p/\rho = \gamma\frac{k_{\text{B}}T}{m}, \tag{1.79}$$

based on Eq. (1.69 and 1.71).

Assuming an isothermal process, i.e., constant temperature, and using the ideal
gas law (Eq. (1.68)), the (isothermal) speed of sound is found to read

$$c_{\text{s, isothermal}} = \sqrt{\frac{k_{\text{B}}T}{m}}. \tag{1.80}$$

Both expressions for the speed of sound must be amended in the context of a plasma,

where the pressure, and therefore the speed of sound, is mainly due to the electron density. Based on the pressure in an ideal gas (Eq. (1.68)) the approximate plasma pressure is derived using the assumptions of (i) single temperature T, (ii) quasi-neutrality $n_e = Zn_i$ and (iii) highly ionized plasma $Z \gg 1$ (e.g., in EUV applications [17] $Z > 8$), where Z denotes the average charge state. The alternative form becomes

$$p = n_e k_B T_e + n_i k_B T_i = (n_e + n_i)k_B T = (Zn_i + n_i)k_B T \tag{1.81}$$

$$\approx Zn_i k_B T = \frac{\rho}{m_{ion}} Z k_B T, \tag{1.82}$$

and the expression for the speed of sound becomes

$$c_{s,\,plasma} = \sqrt{Z}c_s, \tag{1.83}$$

which applies to c_s for both Eq. (1.78 and 1.80).

1.5.3 Frankfurt equation-of-state

In the RALEF-2D simulations presented in this thesis, the Frankfurt equation-of-state (FEOS) [52] is used. As a further development of the MPQeos model [54], it is based on the quotidian equation-of-state (QEOS) model [55]. In the QEOS model, the specific Helmholtz free energy f is used to derive thermodynamic quantities. The Helmholtz free energy measures the work a closed thermodynamic system can perform at a constant temperature (per unit mass) and f is defined in terms of the specific internal energy (ϵ), temperature T and the specific entropy (s). Its definition is $f = \epsilon - Ts$, which can be split into three contributions,

$$f = f_e + f_i + f_b, \tag{1.84}$$

an electronic part, an ionic part and a semi-empirical bonding correction.

After setting up an EOS model, thermodynamic quantities such as pressure, specific internal energy, and specific entropy can be derived from the specific Helmholtz free energy, as captured in

$$p = \rho^2 \left(\frac{\partial f}{\partial \rho} \right)_T, \; s = - \left(\frac{\partial f}{\partial T} \right)_\rho, \; \epsilon = f + Ts, \tag{1.85}$$

which is calculated as function of density ρ and temperature T in the QEOS and FEOS models. Let us now briefly address the three contributions in Eq. (1.84).

1.5.3.a Electronic contribution

The electronic part corresponds to the thermal and cold contributions to the EOS by the electrons, which are described by the simple Thomas–Fermi (TF) statistical model of atoms [56]. The electrons are considered as a degenerate Fermi gas in the self-consistent electrostatic field of the electrons and ions. The main advantage of the simple TF model is that the TF equation must be solved and tabulated only once, for hydrogen, as all thermodynamic quantities scale with atomic number Z. Disadvantages include the exclusion of any quantum and relativistic effects beyond Fermi statistics and quantized phase space, but the main disadvantage is the absence of attractive, bonding forces between neutral atoms. These originate from electron–electron interaction quantum effects, and their absence leads to an overestimation of pressure near normal conditions in a solid body. For example, the calculation of the ionization degree z_{ion} is based on scaling the solution for hydrogen [55]. The expression for hydrogen is based on the number of electrons within the so-called ion sphere: each nucleus is located at the center of a spherical cavity. It contains enough electrons to be electrically neutral, while other ions are assumed to be outside the sphere. The electron density, to find the number of electrons, is determined by the formula for a finite-temperature semiclassical electron gas.

1.5.3.b Bonding correction

The semi-empirical bonding correction, denoted by f_{b}, aims to relieve this (main) disadvantage. It calibrates the EOS based on user-defined values of the density (ρ_0) and the bulk modulus (K_0) at a reference point $(p, T) = (0, T_0)$. The bulk modulus is defined as $K = \rho(\partial p/\partial \rho)_s$ and is related to the sound speed $c_s^2 = (\partial p/\partial \rho)_s = K/\rho$ by Eq. (1.77). For an ideal gas undergoing an adiabatic process, Eq. (1.79) shows that the bulk modulus equals $K = \gamma p$. The reference point is chosen such that the studied material is in the solid state: the reference temperature T_0 is well below the critical temperature.

1.5.3.c Ionic contribution

The thermodynamic contribution of the ions is fully independent of the electrons. It becomes significant at temperatures $T < 10$ eV and densities close to solid density.

At higher temperatures and/or densities, the electron contribution dominates. The ionic part is calculated with the Cowan model [55] in which analytical formulas are employed for smooth interpolation between the states of Debye solid, normal solid and liquid. The ionic internal energy and pressure are of purely thermal nature [52].

1.5.3.d   Implementation in fluid simulations

Moreover, FEOS provides two options for the EOS in the liquid–vapor two-phase region, (i) the metastable EOS featuring Van-der-Waals loops and (ii) the equilibrium EOS calculated by an iterative Maxwell construction scheme. In the region below the critical temperature (more precisely, below the binodal), following the van der Waals EOS leads to a metastable path known as a van der Waals loop. These metastable states are highly unstable, where small perturbations can lead to a transition to liquid or vapor states. Due to the random nature, this process leads to the coexistence of both states in the fluid.

Instead, in the simulations presented here, the equilibrium EOS model is used which is derived by the equality of the chemical potentials in the liquid and vapor phases and can be determined by a Maxwell construction [52]. The results are isotherms (lines of constant T) in the region below the binodal corresponding to isobaric curves (constant pressure). In other words, constant lines in a (p, V) diagram connecting the crossings of this specific isotherm with the binodal.

For the RALEF-2D simulations, the FEOS data is gathered in tabulated form beforehand. In addition to the mentioned pressure $p(\rho, e)$ and temperature $T(\rho, e)$ as function of density ρ and mass-specific internal energy e, the following variables will be provided to the simulation: the average charge state (or mean ionization degree) $z_{\text{ion}}(\rho, e)$, the mass-specific heat capacity at constant volume $c_V(\rho, e)$ and the isentropic sound speed $c_s(\rho, e)$.

1.6   Analytic formulas for plasma expansion

For this last section of the chapter, solutions to the single-fluid, single-temperature equations are discussed for the expansion of a plasma into vacuum. Thereby, it can be seen as a stepping stone for the following two chapters, Ch. 2 and 3, where our simulations are used to investigate laser-produced plasma expansion. Here, two well-known exact analytical solutions of the one-dimensional hydrodynamics equations will be discussed, where the plasma is initially at rest with a certain temperature and corresponding ionization degree. The discussion includes the density and speed profiles of these analytical solutions and the derivation of the kinetic energy distribution

that characterizes them. Importantly, the analytical solutions are based on specific thermodynamic assumptions, for example the assumption of constant temperature in the expansion (isothermal) or the absence of the heat flow (adiabatic).

These analytical solutions have been derived as description of gas dynamics 'toy' problems [49, 57]. The introduced case describes a half-filled gas tube bounded by a membrane. The second analytical solution, the Riemann wave, is a description of the one-dimensional gas flow in the tube if the membrane is punctured at $t = 0$. Such solutions presented here lay the groundwork for more detailed descriptions of gas dynamics, including high-temperature phenomena such as explosions [49], and plasma dynamics [58].

Recent applications and extensions of this literature are developed for laser-produced plasma expansion [20, 58–62]. The characteristics of an expansion are conveniently captured in the distribution of particles over kinetic energy, dN/dE. These characteristics include the number of particles exceeding a certain kinetic energy bound, the maximum particle energy, and the total number of particles emitted as ionic debris. Experimental and numerical results for the dN/dE will be presented in the two upcoming Ch. 2 and 3.

This section will (i) derive the expression of dN/dE for the two analytical solutions and (ii) discuss the applications of analytical results to laser-produced plasma expansion. Looking forward, our own findings will be reported in Ch. 2 and 3.

1.6.1 Planar isothermal expansion

First, let us consider a planar isothermal expansion into vacuum [49]. Initially, the negative half-space is filled with a number density n_0 and the positive half-space is set to zero density, i.e., vacuum. In an isothermal process, the temperature T remains constant, which can be visualized as the system being connected to a heat bath, a thermal reservoir. Let us assume additionally an ideal gas equation-of-state (Eq. (1.68)), $pV = N k_B T = $ const. holds, and the constant speed of sound is given by Eq. (1.80), denoted c_0 in this paragraph. Let us start from the explicit one-dimensional mass conservation equation for the number density n (based on Eq. (1.30)), which is given by

$$\frac{\partial n}{\partial t} + \frac{\partial}{\partial x}(nu) = 0. \tag{1.86}$$

A self-similar solution ansatz is proposed, which is generally characterized by the ratio $\xi = x/t$ of position and time. Self-similarity is based on the existence of a characteristic speed, instead of, e.g., a characteristic length or time. In other words, distributions of quantities like density and velocity change with time without

changing their form: they remain similar to themselves [49]. Therefore, derivatives
of a function $f(x/t) = f(\xi)$ (such as number density or speed) can be simplified to,

$$\frac{\partial f}{\partial x} = \frac{df}{d\xi}\frac{\partial \xi}{\partial x} = \frac{df}{d\xi}\frac{1}{t}, \tag{1.87}$$

$$\frac{\partial f}{\partial t} = \frac{df}{d\xi}\frac{\partial \xi}{\partial t} = -\frac{df}{d\xi}\frac{x}{t^2} = -\frac{df}{d\xi}\frac{\xi}{t}, \tag{1.88}$$

which leads to the following for the mass conservation equation (Eq. (1.86)), where
x and t are eliminated,

$$-\frac{dn}{d\xi}\frac{\xi}{t} + \frac{dn}{d\xi}\frac{1}{t}u + n\frac{du}{d\xi}\frac{1}{t} = 0,$$

$$(u - \xi)\frac{dn}{d\xi} + n\frac{du}{d\xi} = 0. \tag{1.89}$$

For an isothermal planar expansion into vacuum, the following solution ansatz
is proposed for the speed using the self-similar variable ξ,

$$u(x,t) = c_0 + \xi = c_0 + \frac{x}{t}, \tag{1.90}$$

$$= c_0 \left(1 + \frac{x}{c_0 t} \right). \tag{1.91}$$

Note that the expression $x/(c_0 t)$ is dimensionless and that this solution is defined for
$-1 < x/(c_0 t) < \infty$. The corresponding number density is based on an exponential
profile, which becomes

$$n(x,t) = n_0 \exp\left[-1 - \frac{x}{c_0 t}\right], \tag{1.92}$$

$$= n_0 \exp\left[-u/c_0\right]. \tag{1.93}$$

In the above equations, c_0 denotes the (isothermal) speed of sound, introduced in
Eq. (1.80). Fig. 1.2 presents the evolution of the velocity and density profile in time.
One can check that this solution satisfies Eq. (1.89),

$$c_0 n_0 \exp\left[-1 - \xi/c_0\right] \cdot \left(-1/c_0\right) + n_0 \exp\left[-1 - \xi/c_0\right] = 0. \tag{1.94}$$

1.6.1.a   Kinetic energy distribution

Plasma expansion can be quantified by the distribution of particles over kinetic energy. This will be the form of the main results of our work in Ch. 2 and 3. The distribution function, written as dN/dE, can be calculated explicitly for an analytical solution like this. The expression dN/dE can be related to the number density n and speed u. The number of particles dN in an interval dx is equal to $dN = n\,dx$ in this one-dimensional case. For the particle kinetic energy, $E = \frac{1}{2}m_{\text{ion}}u^2$, the expression becomes

$$dE = m_{\text{ion}}u\,du = m_{\text{ion}}u\,\frac{dx}{t}, \tag{1.95}$$

in terms of the interval dx based on Eq. (1.91). The ratio dN/dE is therefore equal to

$$\frac{dN}{dE} = \frac{n\,dx}{m_{\text{ion}}u\frac{dx}{t}} = \frac{nt}{m_{\text{ion}}u}, \tag{1.96}$$

$$= \frac{n_0 \exp\left[-u/c_0\right] t}{m_{\text{ion}}u}, \tag{1.97}$$

where the number density n is written in terms of speed u, as given in Eq. (1.93). The integrated number of particles in the distribution, i.e., the number of particles participating in the expansion, depends on time. Namely, at time t the rarefaction wave into the negative half-space has covered a distance $c_0 t$, as is visualized in Fig. 1.2. So the number of particles participating in the expansion is equal to $N_0 = n_0 c_0 t$. This gives the following expression

$$\frac{dN}{dE} = \frac{\frac{N_0}{c_0 t}\exp\left[-u/c_0\right] t}{m_{\text{ion}}u}, \tag{1.98}$$

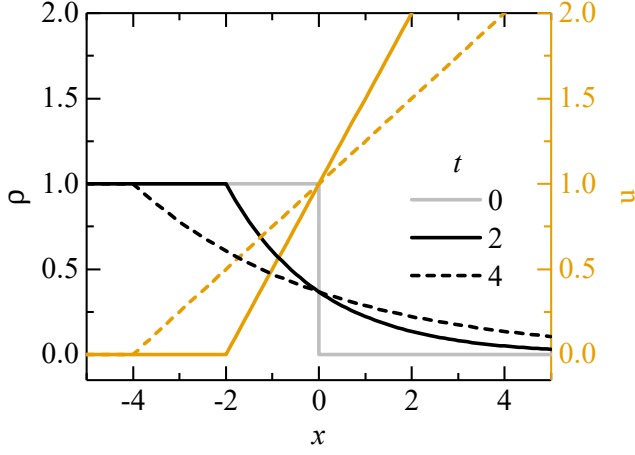$$= \frac{N_0}{c_0 m_{\text{ion}}}\frac{\exp\left[-u/c_0\right]}{u}. \tag{1.99}$$

Figure 1.2: Velocity (yellow) and density (black) profiles of a planar isothermal expansion, resp. Eq. (1.91) and (1.93), for $n_0 = 1$ and $c_0 = 1$.

Now, the expression for the kinetic energy is substituted and the speed of sound for an isothermal plasma is used, given by combining Eq. (1.80) and (1.83),

$$E = \frac{1}{2} m_{\mathrm{ion}} u^2 \longleftrightarrow u = \sqrt{\frac{2E}{m_{\mathrm{ion}}}}, \tag{1.100}$$

$$c_0 = \sqrt{\frac{Z k_{\mathrm{B}} T}{m_{\mathrm{ion}}}} \text{ and } \frac{u}{c_0} = \sqrt{\frac{2E}{Z k_{\mathrm{B}} T}}. \tag{1.101}$$

The result is

$$\frac{dN}{dE} = \frac{N_0}{\sqrt{Z k_{\mathrm{B}} T m_{\mathrm{ion}}}} \sqrt{\frac{m_{\mathrm{ion}}}{2E}} \exp\left[-\sqrt{\frac{2E}{Z k_{\mathrm{B}} T}}\right], \tag{1.102}$$

$$= \frac{N_0}{E_0} \sqrt{\frac{E_0}{2E}} \exp\left[-\sqrt{\frac{2E}{E_0}}\right]. \tag{1.103}$$

where a so-called characteristic energy scale is introduced, equal to $E_0 = m_{\mathrm{ion}} c_0^2 = Z k_{\mathrm{B}} T$. The expression in Eq. (1.103) is shown in Fig. 1.3 as a black curve.

1.6.2 Planar isentropic expansion

Another analytical solution can be found for a planar isentropic expansion, also known as the Riemann wave. It is based on the previously introduced equation-of-state for an ideal gas undergoing an isentropic process. As the isothermal and isentropic processes can be both described in context of a polytropic index, with $n_{\text{poly}} = 1$ and $n_{\text{poly}} = \gamma$ respectively, all expressions given below tend to the isothermal form in the limit $\gamma \to 1$. This self-similar solution ansatz is given by [49]

$$u(x, t) = \frac{2c_0}{\gamma + 1} \left(1 + \frac{x}{c_0 t} \right), \tag{1.104}$$

$$n(x, t) = n_0 \left(\frac{2}{\gamma + 1} - \frac{\gamma - 1}{\gamma + 1} \frac{x}{c_0 t} \right)^{2/(\gamma - 1)}, \tag{1.105}$$

and defined for $-1 < x/c_0 t < 2/(\gamma - 1)$. The speed of sound, c_0, is defined by its isentropic form, Eq. (1.78), again amended by Eq. (1.83).

For this case, the ion energy distribution can be derived similarly and is given by

$$\frac{dN}{dE} = \frac{n_0}{Z k_{\text{B}} T} \frac{\gamma^2 - 1}{4\gamma} \sqrt{\frac{E_{\text{max}}}{E}} \left(1 - \sqrt{\frac{E}{E_{\text{max}}}} \right)^{2/(\gamma - 1)} \tag{1.106}$$

where $E_{\text{max}} = (2\gamma/[\gamma - 1]^2) Z k_{\text{B}} T = (2\gamma/[\gamma - 1]^2) m_{\text{ion}} c_0^2$ denotes the maximum energy in the distribution.

1.6.3 Application to laser-produced plasma expansion

A laser-produced plasma expansion can be approximated by different (analytical) descriptions. The two analytical solutions discussed above provide descriptions of the free expansion of a fluid under stringent assumptions, both thermodynamic and dimensional. An application of the isothermal solution to laser-produced plasma expansion can be understood as replacing the heat bath by uniform energy deposition by a laser. This requires specific conditioning, e.g., a precise temporal laser dependence, which is reported by Murakami *et al.* [59].

Moreover, the discussed adiabatic solution can be used for the free expansion of a hot plasma (such as previously heated by laser irradiation) into vacuum. The adiabatic assumption is applicable to this case lacking laser energy deposition or heat exchange with the vacuum. Murakami *et al.* [59] successfully coupled analytical solutions of isothermal expansion during laser irradiation with adiabatic expansion afterward.
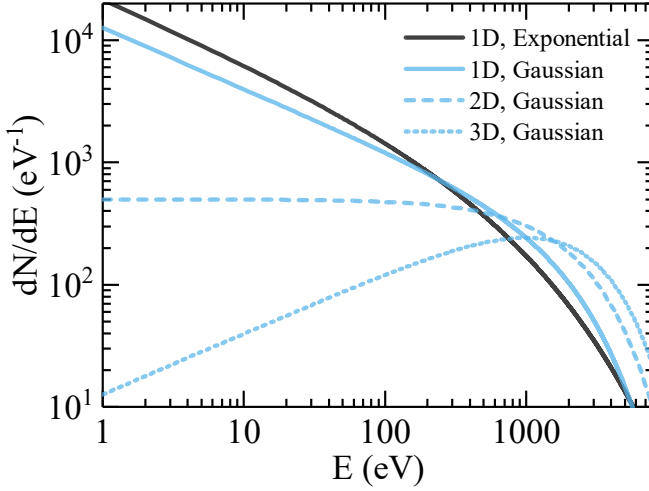
Figure 1.3: Examples of ion kinetic energy distributions resulting from isothermal expansion: Eq. (1.103), for planar (1D) expansion based on an exponential density profile, is shown. The result of Murakami *et al.* [59], based on a Gaussian density profile, is shown for planar, cylindrical and spherical expansion, as given in Eq. (1.107). The characteristic energy of the shown distributions is $E_0 = 1\,\text{keV}$ and the number of ions equals $N_0 = 10^6$.

The discussed one-dimensional solutions may be applicable to flat (solid or liquid) targets with illumination uniform in space. Droplet-based EUV sources lead to expansions in three dimensions. The number of dimensions, in which the expansion is confined, determines the first (energy-dependent) term. Both one-dimensional cases discussed here result in a form of $E^{-1/2}$. This can be generalized to $E^{(\alpha-2)/2}$ with $\alpha = 1, 2, 3$ equal to the number of dimensions [59]. This term determines the slope of the kinetic energy distribution at low kinetic energy for the analytical forms discussed here. The full form of the ion kinetic energy distribution discussed in Murakami *et al.* [59] is given by

$$\frac{dN}{dE} = \frac{N_0}{E_0} \frac{1}{\Gamma(\alpha/2)} \left(\frac{E}{E_0}\right)^{(\alpha-2)/2} \exp\left(-\frac{E}{E_0}\right), \qquad (1.107)$$

where $E_0 = 2zk_{\mathrm{B}}T_{\mathrm{e}} \ln\left(R(t)/R_0\right)$ is a characteristic energy scale, α is the dimensionality of the expansion and N_0 is the total number of ions. The distributions for one-, two-, and three-dimensional expansion ($\alpha = 1, 2$ and 3) are shown in Fig. 1.3(b) as blue curves.

In general, the density profile of the expansion must be corrected for volume

dependence on distance: $V \propto d^{\alpha}$ with $\alpha = 1, 2, 3$. This simple expression holds for an isotropic, radial expansion. In first approximation, this is applicable to the explosion-like expansion of a laser-produced plasma. However, in Ch. 3 our *strongly anisotropic* experimental results are discussed.

The exponential density profile of the presented isothermal solution, Eq. (1.93), is also applied in the context of plasma expansion [58, 60]. The connection lies in the Boltzmann factor, derived in Eq. (1.15), which has an exponential form. It describes the Maxwell–Boltzmann distribution of the electron density. Generally, the functional form of the density profile determines the function of E that is the last term in Eq. (1.103 and 1.106). For example, in the isothermal case, an exponential density profile leads to $\exp\left(-\sqrt{2E/E_0}\right)$, while a Gaussian profile results in $\exp\left(-E/E_0\right)$ instead [59]. This in turn determines the fall-off of the kinetic energy distribution with increasing energy, as is visible in Fig. 1.3 by comparison of the black and blue (solid) curves.

The speed of sound, as introduced in Sec. 1.5.2, plays an important role in the description of gas and plasma dynamics. In the presented analytical solutions, Eq. (1.91) and (1.104), the sound speed determines (up to a constant factor) the flow velocity at $x = 0$, but also the velocity of the rarefaction front moving into the material. Moreover, the characteristic energy scale that is introduced in Eq. (1.103) is directly dependent on the sound speed c_0. Due to its formulation in terms of plasma temperature, Eq. (1.80), the sound speed is often used as the characteristic velocity in a laser-produced plasma expansion. However, it is important to note that a significant amount of particles travels at velocities above the sound speed in the analytical solutions as well as in the presented experimental and numerical results. Only in the case of adiabatic constraints during the full expansion can a maximum kinetic energy be defined, and be related to the sound speed. In Ch. 5 the spatial dependence of the sound speed will be explicitly presented, in conjunction with the fluid flow speed. The sonic surface, where the fluid speed equals the sound speed, occurs close to the critical surface [53]. In other words, subsonic ablation flow occurs between the droplet surface and the critical surface, while the flow becomes supersonic past the critical surface. Therefore, the reported ion kinetic energy distributions in Ch. 2 and 3 are the result of supersonic flow dynamics.

As will become clear in the following chapters, Ch. 2 and 3, it is modeling of the complexity of the actual density profiles that will enable an accurate prediction of the ion kinetic energy distributions.

2

High-energy ions from Nd:YAG laser ablation of tin microdroplets: Comparison between experiment and a single-fluid hydrodynamic model

Diko J. Hemminga, Lucas Poirier, Mikhail Basko, Wim Ubachs, Ronnie Hoekstra, Oscar O. Versolato, and John Sheil

We present the results of a joint experimental and theoretical study of plasma expansion arising from Nd:YAG laser ablation (laser wavelength $\lambda = 1.064\,\mu$m) of tin microdroplets in the context of EUV lithography. Measurements of the ion energy distribution reveal a near-plateau in the distribution for kinetic energies in the range $0.03 - 1\,$keV and a peak near $2\,$keV followed by a sharp fall-off in the distribution for energies above $2\,$keV. Charge-state resolved measurements attribute this peak to the existence of peaks centered near $2\,$keV in the $Sn^{3+} - Sn^{8+}$ ion energy distributions. To better understand the physical processes governing the shape of the ion energy distribution, we have modelled the laser-droplet interaction and subsequent plasma expansion using two-dimensional radiation-hydrodynamic simulations. We

---

[*] Diko Hemminga contributed to this chapter as part of his thesis regarding investigation through performing simulations, visualization, and both writing of the first draft and writing, review and editing of the final draft.

find excellent agreement between the simulated ion energy distribution and the measurements both in terms of the shape of the distribution and the absolute number of detected ions. We attribute a peak in the distribution near 2 keV to a quasi-spherical expanding shell formed at early times in the expansion.

2.1 Introduction

Laser-produced plasmas (LPPs) formed on tin microdroplets are now established as the light source of choice in new-generation lithography machines for high-volume manufacturing of integrated circuits below the 10 nm node [6, 7, 63]. Their incorporation in modern-day lithography machines relies on their ability to provide sufficiently high fluxes of short-wavelength radiation to enable the patterning of nanometer-scale features on integrated circuits.

Under optimum conditions, spectra recorded from tin LPPs exhibit an intense, narrowband emission feature centered near an extreme ultraviolet (EUV) wavelength of 13.5 nm [17, 34, 64–66]. The superposition of millions of lines arising from transitions between complex configurations in $n = 4$ shell Sn^{11+} – Sn^{15+} ions are the atomic origins of this light [16, 18, 67–69]. Importantly, this feature overlaps with the 2% reflective bandwidth (13.5 ± 0.135 nm — the so-called "in-band" region) of molybdenum/silicon multilayer mirrors (MLMs) [13]. Such mirrors are an integral component of EUV lithography (EUVL) tools, transporting EUV photons from the light source to their final destination at the wafer stage.

One key aspect of industrial EUV light source development has focused on optimising the photon output of LPP EUV light sources. To-date, efforts have concentrated on increasing (i) EUV power and (ii) the so-called conversion efficiency (CE — the ratio of in-band EUV energy emitted into the half sphere back towards the laser to input laser energy) of the light source [7, 66]. To meet the high power levels required for industrial applications, a dual-pulse irradiation scheme is employed [70]. First, a low-intensity pre-pulse is used to deform the droplet into an elongated disk-like target. This target is then irradiated by a second, high-energy CO_2 laser pulse ($\lambda = 10.6 \, \mu m$) which generates a hot, EUV-emitting plasma. This EUV light is then focused by an MLM (the collector mirror) to an exit port of the light source vessel whereupon it enters the scanner tool for use in the lithographic process. A second and no-less crucial aspect of EUV light source development has focused on the design and implementation of so-called debris mitigation schemes. In the context of the current application, plasma expansion will lead to the bombardment by tin ions on the plasma-facing collector mirror. The combined effects of sputtering and ion implantation will, over time, degrade the performance of the collector mirror and reduce EUV throughput. In an industrial setting, the light source vessel is typically filled with a background hydrogen gas to stop energetic ions from reaching the collector mirror [7, 22, 23]. One can also introduce a strong magnetic field in the region surrounding the droplet to deflect plasma ions away from the collector mirror [71–73].

A comprehensive understanding of the characteristics of the plasma expansion (distribution of ions over kinetic energy, angular distribution of ions, etc.) can greatly assist the design of effective debris mitigation schemes.

A number of studies examining tin plasma expansion have been performed over the past two decades. In the mid-2000's, Murakami *et al.* [59] and Fujioka *et al.* [20] demonstrated that ion energy distributions recorded from minimum-mass plasmas driven by 10 ns-long Nd:YAG ($\lambda = 1.064\,\mu$m) pulses can be described using a model of isothermal plasma expansion. In this model, the distribution of the number of ions N as a function of kinetic energy E is written

$$\frac{dN}{dE} = \frac{N_0}{E_0} \frac{1}{\Gamma(\alpha/2)} \left(\frac{E}{E_0} \right)^{(\alpha-2)/2} \exp\left(-\frac{E}{E_0} \right), \tag{2.1}$$

where $E_0 = 2zk_{\mathrm{B}}T_{\mathrm{e}} \ln\big(R(t)/R_0\big)$ is a characteristic energy scale dependent on the charge state z, electron temperature T_{e}, initial plasma size R_0 and a time-dependent characteristic system size $R(t)$ (k_{B} denotes the Boltzmann constant). In the above equation α is the dimensionality of the expansion ($\alpha = 1, 2$ and 3 correspond to planar, cylindrical and spherical geometries, respectively), Γ is the gamma function, $N_0 = (\sqrt{\pi}R_0)^{\alpha} n_{\mathrm{i}00}$ is the total number of ions and $n_{\mathrm{i}00}$ is the initial ion number density at the origin of the model, i.e., $n_{\mathrm{i}00} = n_{\mathrm{i}}(r = 0, t = 0)$. Experiments performed by Bayerle *et al.* [61] also qualitatively demonstrate the applicability of Murakami's model (Eq. (2.1)) to Nd:YAG-irradiated (6 ns pulse duration) planar tin targets.

Plasmas driven by shorter, ps-duration pulses [61, 62] exhibit ion energy distributions whose shapes are better described by the planar isothermal expansion model of Mora [60]. In this case the ion energy distribution reads

$$\frac{dN}{dE} = \frac{N_0^*}{E_0^*} \sqrt{\frac{E_0^*}{2E}} \exp\left(-\sqrt{\frac{2E}{E_0^*}} \right), \tag{2.2}$$

where N_0^* is the total number of ions and the characteristic energy scale $E_0^* = zk_{\mathrm{B}}T_{\mathrm{e}}$. The main difference between the two models lies in the choice of the plasma density profile. The model of Murakami *et al.* [59] employs a Gaussian profile for the plasma density $\rho \propto \exp\big(-[r/R(t)]^2\big)$ whereas an exponential density profile is used in the work of Mora [60]. As noted by Murakami *et al.* [59], this latter form for the density profile is better suited for plasmas generated by short pulse lasers or those formed on thick targets.

Other work on the topic of tin plasma expansion has explored, for example, the role of laser pulse duration and laser wavelength on the ion energy distribution [74–

76], the angular distribution of ion kinetic energies [77–81], the suppression of fast ions using a low-energy pre-pulse [82, 83], and the role of electron-ion recombination during the expanding phase of the plasma [84]. It is important to note that the vast majority of these studies have investigated plasma expansion from laser-irradiated planar tin targets rather than from industrially relevant droplet targets. Much work still remains to be done on this latter topic.

The goal of the present study is to investigate plasma expansion in the form of emission of energetic charged particles from Nd:YAG-irradiated tin microdroplet targets. This study serves to complement recent work on photon emission from solid-state laser-driven EUV light source plasmas [66, 85, 86]. In contrast to the current industrial implementation, solid-state laser-driven plasmas may not require the use of a pre-pulse for efficient EUV production [66]. As such, they are a promising candidate for future laser-driven EUV light source plasmas. First we present measurements of the ion energy distributions using an electrostatic analyser (ESA). These measurements reveal the existence of peaks near $2\,\mathrm{keV}$ in the high-energy tails of the Sn^{3+} – Sn^{8+} ion energy distributions. These features combine to yield a peak near $2\,\mathrm{keV}$ in the charge-state integrated ion energy distribution. To elucidate the origin of this peak, we have performed two-dimensional radiation-hydrodynamic simulations of the plasma formation and its subsequent expansion using the RALEF-2D code. The ion energy distribution obtained from the simulations compares favourably to the measurements both in terms of the shape of the distribution and the absolute number of detected ions. We attribute the peak in the ion energy distribution to a high-velocity, quasi-spherical expanding shell formed at early times in the plasma expansion. The current work advances on the work presented in Refs. [34, 61] to provide a quantitative understanding of absolutely-calibrated measurements via radiation-hydrodynamic modelling of the expanding plasma, beyond the aforementioned idealized plasma expansion models.

The layout of this chapter is as follows: In Sec. 2.2 we discuss the experimental setup and provide details of the ion energy distribution measurements. This is followed by a description of the single-fluid, single-temperature model implemented in the RALEF-2D code and a brief discussion of the simulation parameters. In Sec. 2.4 we discuss the results of the simulations, focusing on the temporal and spatial evolution of the speed and ion number density profiles in the expansion. In Sec. 2.5 we compare the ion energy distribution obtained from the simulations with our experimental measurements. Comparisons are drawn with the predictions of well-known analytical models of plasma expansion into vacuum. Finally, we summarise this work in Sec. 2.6.

2

2.2   **Experimental setup, method and results**

In the experiments, tin droplets were dispensed from a droplet generator mounted at the top of a vacuum chamber (backing pressure $\sim 10^{-7}$ mbar). The droplet generator consists of a heated (260 °C) molten tin reservoir connected to a nozzle. The diameter of the tin droplets used in the experiment was 28 μm. Upon crossing the centre of the chamber, the droplets pass through a light sheet created by a He-Ne laser. Light scattered by the droplets was detected by a photo-multiplier tube which triggered the plasma-generating laser pulse and the acquisition apparatus. Plasmas were generated by focusing the output of a commercial Nd:YAG laser system onto the tin droplets. The laser pulses exhibited Gaussian-like temporal and (focused) spatial laser profiles. The temporal full-width at half-maximum (FWHM) was 10 ns and the FWHM of the focused pulses was approximately 60 μm. Employing a laser pulse energy of 60 mJ resulted in a laser power density on the targets of $I_\mathrm{L} \approx 2 \times 10^{11}$ W cm^{-2}. This choice of power density is known to yield optimum CE's for Nd:YAG-driven tin plasmas [66]. We note that this particular choice of laser parameters, combined with the given droplet diameter, will not lead to the full ablation of the tin droplet.

Charge-state resolved ion energy distributions were measured using an electrostatic analyzer (ESA). The opening aperture of this device was located 1.12 m away from the droplet targets and was positioned at 60° with respect to the incident laser axis. The ESA consists of a radial electric field deflection region followed by a calibrated channeltron detector. The radial electric field between the two electrodes of the ESA selects charge states based on the ratio of their kinetic energy E to charge state z according to $E/z = 5 \times U_\mathrm{ESA}$ where U_ESA is the voltage across the ESA electrodes (measured in volts). A time-of-flight (TOF) analysis is used to obtain charge-state resolved ion counts for a given E/z. By scanning the ESA voltage U_ESA over a desired range, one can obtain charge-state resolved ion energy distributions. The ESA-TOF measurements have been benchmarked against charge-state integrated measurements made using a Faraday cup (FC) which was positioned at an angle of −60° with respect to the incident laser axis.

The total ion energy distribution $d^2N/dEd\Omega$ was derived from the measurements via

$$\frac{d^2N}{dEd\Omega} = \sum_z \frac{N_z^\mathrm{m}(E)}{\eta_\mathrm{det}\,\eta_\mathrm{CR}\,\Delta E\,(E)\,\Delta\Omega}, \qquad (2.3)$$

where $\Delta E\,(E)$ is the energy-dependent absolute energy resolution, $N_z^\mathrm{m}(E)$ is the number of tin ions of charge state z having kinetic energy in the range $E \pm (\Delta E(E)/2)$ detected by the channeltron, η_det is the detection efficiency of the channeltron, η_CR ($\leq$
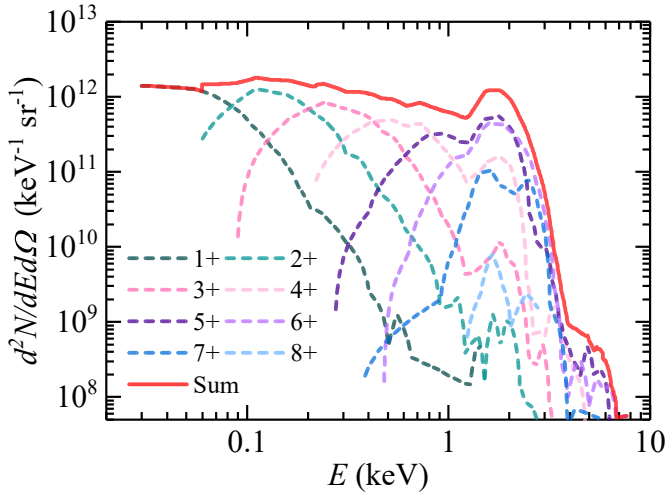
Figure 2.1: Experimental measurements of the distribution of the number of ions over ion kinetic energy is shown. Charge-state resolved ion kinetic energy distributions for Sn^{1+} – Sn^{8+} are shown as dashed colored lines. The total ion energy distribution, shown in red, is obtained by summing the distributions of the individual charge states.

1) is a correction for undetected counts due to high count-rate effects and $\Delta\Omega$ is the solid angle of the input aperture of the ESA device. The absolute energy resolution scales linearly with E according to $\Delta E/E \simeq 10^{-2}$. Further details regarding the ESA calibration can be found in [87].

In Fig. 2.1 we present the results of our charge-state resolved ion energy distribution measurements. Examining this figure, we first note that the distributions associated with Sn^{1+} and Sn^{2+} ions are rather broad, spanning energies in the range $0.05 - 2$ keV. The kinetic energy for which the ion energy distribution peaks, E_{peak}, clearly increases with increasing charge state. Both distributions also exhibit a near-exponential fall-off for $E > E_{\text{peak}}$. While the aforementioned trend in E_{peak} continues for Sn^{3+} and Sn^{4+}, we note the emergence of a second, high-energy peak located just below 2 keV (this peak is also present in the Sn^{2+} distribution although it is less pronounced than in the Sn^{3+} and Sn^{4+} distributions). With increasing charge state this peak grows in intensity until $E_{\text{peak}} \approx 2$ keV in the Sn^{5+} and Sn^{6+} ion energy distributions (we also make a tentative observation of two peaked features in the Sn^{7+} ion energy distribution near 1.6 and 2.5 keV, respectively). While we detect Sn^{8+} ions in the experiments, the amplitude of ion energy distribution is an order-of-magnitude lower than the Sn^{7+} distribution. No traces of higher charge states could be reliably detected. Importantly, the kinetic energy associated with

this high-energy feature is independent of charge state. Shown in red in Fig. 2.1 is the total ion energy distribution obtained by summing the individual Sn^{1+} – Sn^{8+} ion energy distributions. Three distinct regions emerge: (i) a near-plateau in the ion energy distribution between $0.03 - 1$ keV (ii) a peak near 2 keV followed by (iii) a sharp fall-off for $E > 2$ keV. Finally, we note that the EUV-generating tin charge states Sn^{11+} – Sn^{15+}, whilst generated in the hot, dense region of the plasma, are not detected in the measurements. The absence of Sn^{11+} – Sn^{15+} charge states may in part be attributed to the process of recombination, whereby free electrons in the expanding plasma recombine with these ions through processes such as three-body or radiative recombination [84].

2.3   Radiation-hydrodynamic simulations and the RALEF-2D code

In order to elucidate the dynamics of the plasma expansion and its influence on the ion energy distribution, we have undertaken numerical modelling of the plasma formation, growth and subsequent expansion using radiation-hydrodynamic simulations. In the following, we discuss the underlying assumptions of the single-fluid, single-temperature approach adopted in the present work and we provide details of the simulations we have performed with the RALEF-2D code.

2.3.1   Single-fluid single-temperature radiation hydrodynamics

We have chosen to model the plasma formation and its subsequent expansion using a single-fluid, single-temperature hydrodynamic model including the effects of radiation transport and thermal conduction.

In this approach, the free electrons and ions are treated as a single fluid having a single temperature $T_e = T_{ion} = T$. Although more complex approaches such as the two-fluid, two-temperature [36] or single-fluid, two-temperature models [37, 88–90] have been pursued, the single-fluid, single-temperature description should be adequate for the current purposes. For one, simulations of Nd:YAG-irradiated lithium, plastic and gold targets performed by Sunahara *et al.* [37] indicate a rather small difference (less than 20%) between T_e and T_{ion} in the plasma. This behaviour has also been observed in simulations of laser-driven tin plasmas [91]. Second, the moderate ionisation degrees ($z \approx 11 - 15$) found in EUV source plasmas implies that the free-electron contribution to the pressure $p_e = zn_{ion}kT_e$ (in the ideal gas approximation) far outweighs the ion contribution to the pressure $p_i = n_{ion}kT_e$ (n_{ion}

is the ion number density). As such, the ion temperature will play a near-negligible role in the context of the current study.

The equations of single-fluid, single-temperature hydrodynamics take the form

$$\frac{\partial \rho}{\partial t} + \nabla \cdot (\rho \mathbf{v}) = 0 \qquad (2.4)$$

$$\frac{\partial (\rho \mathbf{v})}{\partial t} + \nabla \cdot (\rho \mathbf{v} \otimes \mathbf{v}) + \nabla p = 0 \qquad (2.5)$$

$$\frac{\partial (\rho E)}{\partial t} + \nabla \cdot ((\rho E + p)\mathbf{v}) - (S_{\mathrm{T}} + S_{\mathrm{R}} + S_{\mathrm{ext}}) = 0. \qquad (2.6)$$

In the above equations, ρ is the fluid mass density, $\mathbf{v}$ is the fluid velocity, $p = p_{\mathrm{e}} + p_{\mathrm{i}}$ is the pressure, $E = e_{\mathrm{int}} + |\mathbf{v}|^2/2$ is the mass-specific total energy (sum of the internal and kinetic energy contributions), S_{T} represents thermal conduction, S_{R} is the volume-specific heating rate provided by thermal radiation and S_{ext} represents any external energy sources, e.g., energy deposition from a laser beam, ion beam, etc.

In the single-fluid approach, the plasma is treated as a quasi-neutral fluid, i.e., the electron number density n_{e} is related to the ion number density n_{ion} through $n_{\mathrm{e}} = z n_{\mathrm{ion}}$. It is gradients in the plasma pressure which drives plasma expansion in a quasi-neutral hydrodynamic framework. The principal criterion justifying this approach is that the local Debye length $\lambda_{\mathrm{D}} = [T_{\mathrm{e}}/(4\pi n_{\mathrm{e}} e^2)]^{1/2}$ must be significantly smaller than the scale length of the flow variation $L = n_{\mathrm{ion}}/ \mid \nabla n_{\mathrm{ion}} \mid$. While this condition is typically met in the hot, dense region of the plasma ($\lambda_{\mathrm{D}} < 10\,\mathrm{nm}$), departures from it may exist as the plasma expands and rarefies. In such situations, a kinetic description of the plasma is often employed, where particle-in-cell methods are used to evolve the ion and electron particle distribution functions [70, 92–94]. We will discuss the validity of using the hydrodynamic description of a plasma in the current work in Sec. 2.4.

2.3.2   RALEF-2D

We have performed radiation-hydrodynamic simulations using the Radiative Arbitrary Lagrange-Eulerian Fluid dynamics in two dimensions (RALEF-2D) code. This code was originally developed to provide theoretical support for laser-plasma experiments at GSI Darmstadt under moderate laser intensities $\lesssim 10^{13} - 10^{14}\,\mathrm{W\,cm^{-2}}$ [95, 96]. More recently, the code has found application in modelling laser-driven plasma sources of EUV light [18, 51, 53, 97, 98]. The hydrodynamic component of the

code is based on an upgraded version of the fully-explicit CAVEAT code for ideal hydrodynamics [99, 100]. RALEF-2D solves the single-fluid, single-temperature hydrodynamic equations (Eq. (2.4)-(2.6)) in two spatial dimensions on a structured quadrilateral mesh in either Cartesian (x, y) or axisymmetric (z, r) coordinates using a second-order Godunov-type method [100]. The axisymmetric coordinate system has been used in the present simulations.

In the RALEF-2D code, radiation transfer and heat conduction are coupled into the fluid energy equation using a symmetric semi-implicit method with respect to time discretization [101]. The code solves the LTE radiation transfer equation in the quasi-static approximation using pre-tabulated absorption coefficients generated with the THERMOS code [40, 41]. The equation-of-state (EOS) of tin was built using the Frankfurt equation-of-state (FEOS) model, which can treat both low-temperature liquid-gas phase coexistence regions and high-temperature plasma states [52]. The FEOS model supplies the RALEF-2D code with key thermodynamic quantities such as the pressure, mass-specific internal energy as well as the average charge state of the plasma.

The simulations were performed on a computational mesh shaped in a half-disk consisting of multiple blocks with initially distinct properties. A simplified representation of the mesh is shown in Fig. 2.2. Centered in the origin of the (z, r) coordinate system, we define a tin "droplet" having a mass density of $6.9\,\mathrm{g\,cm^{-3}}$ and a temperature of 592 K (0.051 eV). As in the experiments, the droplet diameter is set to 28 μm. The bulk of the droplet is defined in a mesh section constructed as a rectangle stretched to a half-disk with dimensions of 45×90 mesh cells. As shown in Fig. 2.2, the outer region of the droplet exhibits a more refined mesh structure. Here, the length of each successive mesh cell along the radial direction decreases with increasing r. The mesh cell length on the outer droplet boundary is approximately 10 nm. Outside the droplet the mesh is filled with a tin vapour having a mass density of $10^{-12}\,\mathrm{g\,cm^{-3}}$. This section is divided into quadrilateral cells by approximate concentric and radial edges and extends to a radial distance of 10 mm.

In essence, the experimental laser parameters have been replicated in the simulations. The laser beam is circular and coaxial to the positive z-axis. The simulations have employed unpolarized laser light. Laser energy deposition was modelled using the process of inverse bremsstrahlung.

The ion energy distribution is extracted from the fluid simulation by considering mass flow through the computational mesh. The main fluid variables density and velocity are assigned to each mesh cell throughout the simulation and are converted to the quantities mass and speed (velocity magnitude). These variables are
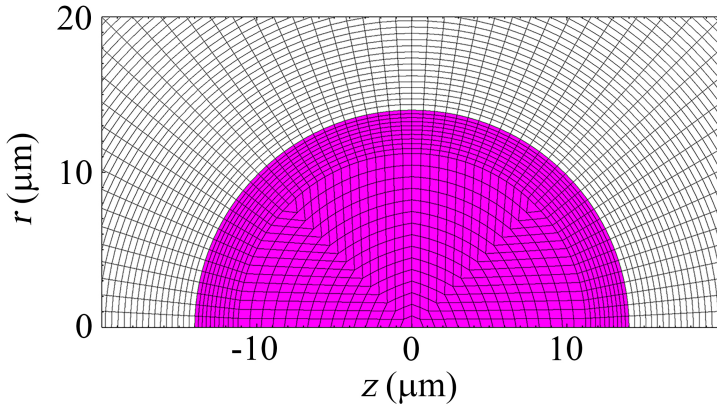
Figure 2.2: A simplified representation of the mesh structure employed in the RALEF-2D simulations. The liquid droplet, shown in purple, is assigned an initial mass density of 6.9 g cm^{-3} and a temperature of 592 K (0.051 eV). The region outside the droplet is filled with a tin vapour having a mass density of 10^{-12} g cm^{-3}.

cell-centered and form the basis of keeping track of the fluid throughout the simulation. As the curved boundary of the computational mesh is defined as a free-outflow boundary, matter flowing out of the mesh leaves the computational domain; it leaves the simulated area in space. This is closely related to the treatment of the ion energy distribution by RALEF-2D. Mass flowing out of the mesh is recorded (i.e., binned) in the (i) energy bin corresponding to its speed and (ii) the angular bin corresponding to the angle between the laser axis and the escape velocity vector. This module is called at every hydrodynamic time step, summing the number of particles equivalent to the out-flowing mass. This procedure explicitly constructs the distribution of the number of particles into 360 predefined discrete energy bins in the range $[1, 20 \times 10^3]$ eV. The bin width increases exponentially with increasing energy. The angular domain is divided into 36 bins (over 180°). In the current simulation we consider mass flow into two angular bins extending over the range [55°, 65°]. The duration of the simulation is 1 µs which allows accounting for ions with energies down to about 70 eV leaving the computational domain in this time window.

2.4 Plasma formation and expansion

In Fig. 2.3 we present the evolution of the plasma expansion through the variables speed and ion number density, where the pseudocolor indicates the magnitude of these variables. At distances larger than 0.5 mm the velocity vector effectively points
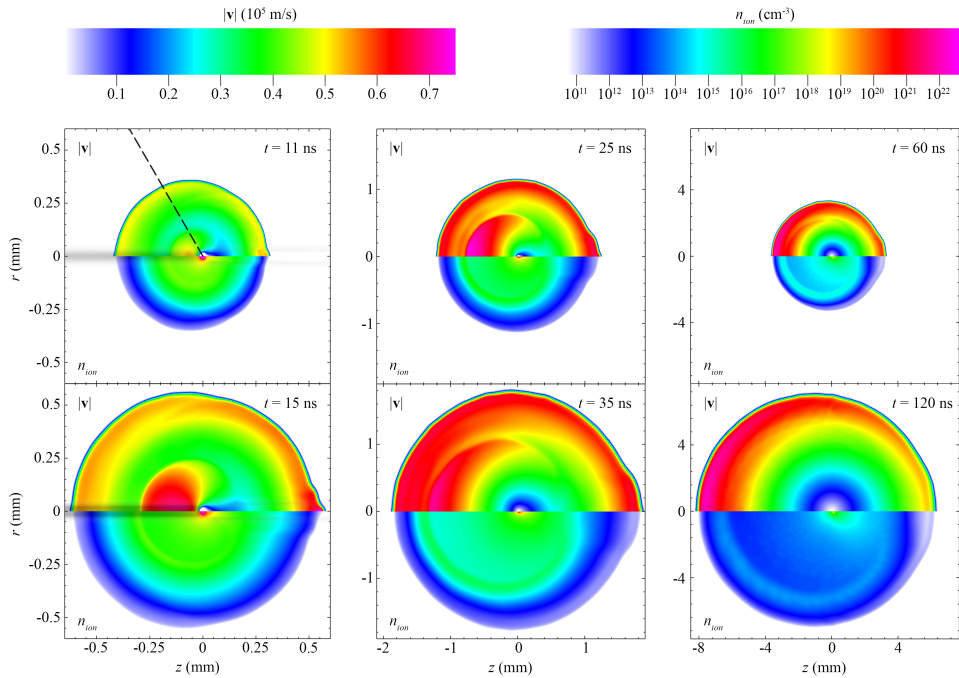
Figure 2.3: Two-dimensional profiles of the speed $|\mathbf{v}|$ and ion number density n_{ion} during laser ablation and subsequent plasma expansion are shown. The color scale represents the size of the variable. The laser illuminates from the left along the z axis, illustrated in the $t = 11/15$ ns frames by the black shaded band. The black dashed line in the $t = 11$ ns frame corresponds to the "lineout" (see main text for description) along which the speed and ion number density profiles shown in Fig. 2.5 and 2.6 are taken.
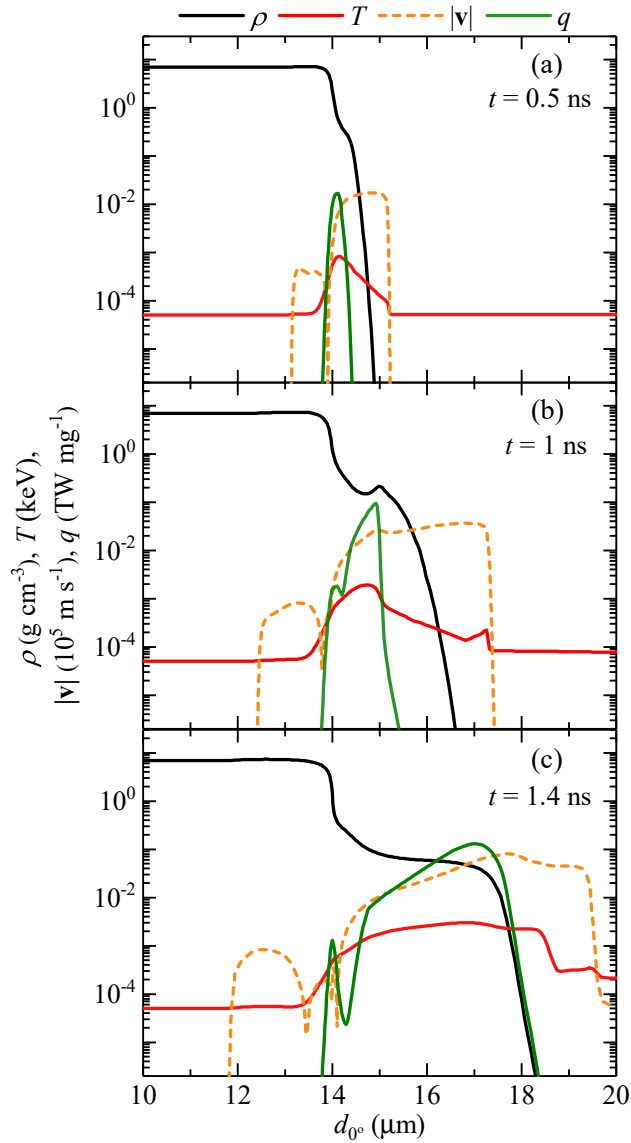
Figure 2.4: One-dimensional profiles of the mass density ρ (black), temperature T (red), speed $|\mathbf{v}|$ (orange dashed curve) and mass-specific laser heating rate q (green) along the negative axial coordinate axis for times $t =$ (a) 0.5, (b) 1 and (c) 1.4 ns.

radially outwards. The ion number density n_{ion} is obtained from $n_{\text{ion}} = \rho N_A / A$, where ρ is the fluid density, N_A is the constant of Avogadro and A is the atomic weight of tin. For visibility, we reflect the ion number density information into the lower plane (this is possible as the simulations were performed using the axisymmetric (z, r) coordinate system). We define $t = 0$ ns as the time that the laser pulse is switched on in the simulations. The left column shows times $t = \{11, 15\}$ ns, the middle column $t = \{25, 35\}$ ns and the right column the late times $t = \{60, 120\}$ ns. The laser propagates along the positive z axis (laser axis) and its (local) intensity is represented by the black shading seen in the $t = \{11, 15\}$ ns frames.

Frames grouped in the same column, e.g., $t = \{11, 15\}$ ns share the same axial and radial domains. In order to follow the plasma expansion in space, we increase the axial and radial coordinate domains in the $t = \{25, 35\}$ and $\{60, 120\}$ ns frames.

The overall dynamics of plasma formation and expansions, as displayed in Fig. 2.3, can be qualitatively described as a succession of two distinct bursts of laser-induced ablation from the droplet surface. These two bursts are clearly identified in the $t = 15$ ns and $t = 25$ ns frames as two concentric red regions exhibiting high velocity magnitude. In the following two subsections we describe the formation and evolution of these two ablation bursts.

2.4.1   Initial burst of laser-induced ablation

The initial burst of laser-induced ablation forms in the first $2 - 3$ ns after the laser pulse is turned on. Initially, the laser pulse has an intensity $I \approx 3 \times 10^8$ W cm^{-2} which lies only moderately above the ablation threshold of liquid tin. In Fig. 2.4 we plot one-dimensional (1D) profiles of the mass density ρ (black), temperature T (red), fluid speed $|\mathbf{v}|$ (orange dashed curve) and mass-specific heating rate of the laser q (green) along the negative laser axis (starting from the droplet center) at times $t = $ (a) 0.5, (b) 1 and (c) 1.4 ns, respectively. These data are extracted along a so-called "lineout" taken at $\theta = 0°$ with respect to the axial coordinate (laser) axis.

As is evident from Fig. 2.4 (b), the temperature of the ablated plasma $T \approx 1 - 2$ eV exceeds the critical temperature of tin ($T_{\text{critical}} \approx 0.5$ eV) by only a moderate factor. In addition, we notice the emergence of a hump in the speed profile at $d_{0°} \approx 15$ µm which is coincident with the location of the peak value of q, the mass-specific laser heating rate. Material associated with this hump accelerates and eventually "catches up" with the initially-ablated material. By $t \approx 2.5$ ns, the speed profile exhibits a near-linear dependence on distance d, i.e., $|\mathbf{v}| \propto d$ and the speed of the front edge of the plasma cloud stabilizes to $|\mathbf{v}_{\text{front}}| \approx 33$ km s^{-1}. This expanding plasma cloud

drives a shock into the low-density ($\rho = 10^{-12}\,\mathrm{g\,cm^{-3}}$) ambient gas which, however, has a negligible effect on the overall expansion dynamics.

2.4.2 Second burst of laser-induced ablation

The increase in laser intensity (and subsequent increase in the mass-specific laser-heating rate q) as $t \to 15\,\mathrm{ns}$ generates a second burst of ablation visible in the upper halves of the $t = 11, 15$ and $25\,\mathrm{ns}$ frames in Fig. 2.3. This second burst is characterized by a significantly higher ablation rate, density and temperature ($T > 30\,\mathrm{eV}$) of the ejected plasma whose leading edge quickly reaches a speed $|\mathbf{v}_{\mathrm{front}}| \approx 60\,\mathrm{km\,s^{-1}}$.

To better understand the dynamics of this ablation burst along the line-of-sight of the ESA and FC devices, we show in Fig. 2.5 the (a) speed and (b) ion number density profiles along a lineout taken at $\theta = 60°$ with respect to the laser axis at times $t = 5$ (black), 10 (red), 15 (blue), and 20 ns (green), respectively. This lineout is shown as a black dashed line in the $t = 11\,\mathrm{ns}$ frame in Fig. 2.3. The shaded vertical bars indicate the location of local maxima in the number density lineouts and serve to guide the eye between both variables. From Fig. 2.5 we see that as the second and more powerful ablation burst rams into the background plasma (left behind by the initial ablation burst), it rakes up material into a quasi-spherical expanding shell. This shell is evident as a hump in the $t = 15$ and 20 ns n_{ion} profiles in Fig. 2.5(b). The deposition of energy (via laser absorption) and the expansion that follows can be likened to the effects of a fast piston pushing a gas; the shockwave launched by the piston effectively sweeps up material in front of it, driving a compression wave.

In Fig. 2.6 (a) and (b) we plot the speed and ion number density profiles along the $\theta = 60°$ lineout at times $t = 30$ (orange), 50 (light blue), 80 (purple) and 120 ns (dark green). As the plasma expands, we note that the two speed profiles merge to form a single profile exhibiting a near-linear dependence of the on distance. A linear dependence of speed on distance, i.e., $|\mathbf{v}| = d/t$ is exactly the asymptotic $t \to \infty$ behaviour of any explosion-like expansion [49]. Our simulations therefore recover the late-time behaviour expected from such an expansion. The evolution of the ion number density profiles over time and space is less dramatic. First, we note that the quasi-spherical expanding shell observed in Fig. 2.5 (b) persists throughout the expansion. As time evolves the shell is observed to broaden, a direct consequence of the non-constant speed profile across the shell. It is interesting to note that the spatial variation of the ion number density up to the quasi-spherical shell appears to follow a power law of the form $n_{\mathrm{ion}} \sim d^{-n}$ where $2 < n < 3$. Unlike the speed profile, a universal analytic form for n_{ion} as $t \to \infty$ does not exist for an explosion-like expansion. As discussed by Zel'dovich and Raizer [49], the asymptotic solution
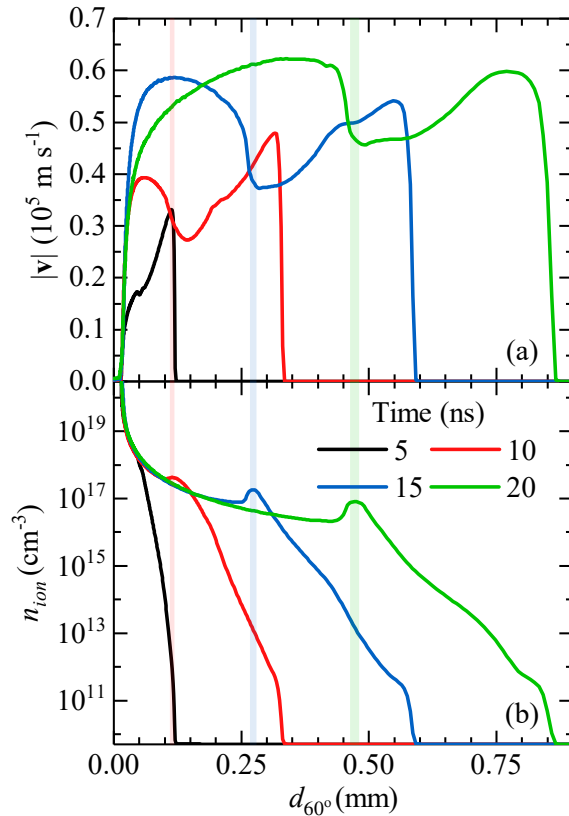
Figure 2.5: One-dimensional profiles of the (a) speed and (b) ion number density along the lineout shown in Fig. 2.3 at $t = 5$ (black), 10 (red), 15 (blue) and 20 ns (green).
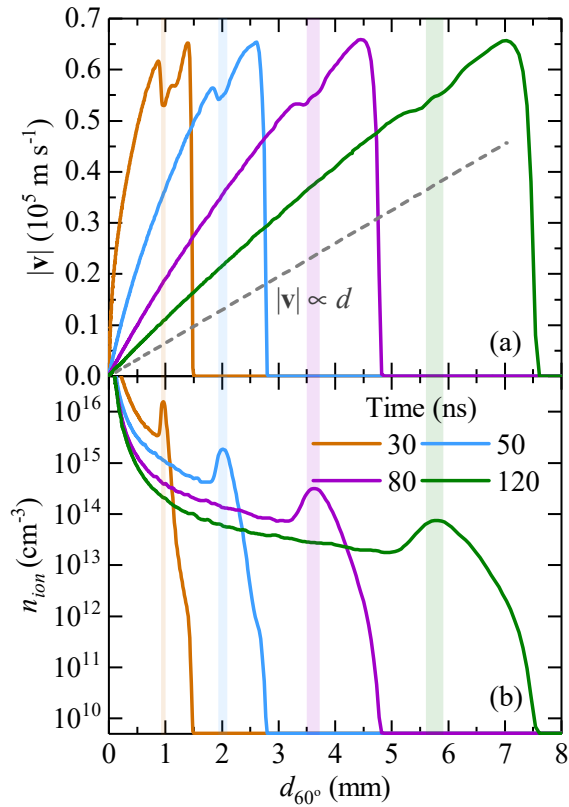
Figure 2.6: One-dimensional profiles of the (a) speed and (b) ion number density along the lineout shown in Fig. 2.3 at $t = 30$ (orange), 50 (light blue), 80 (purple) and 120 ns (dark green). The gray dashed line illustrates an analytic form for the speed $|\mathbf{v}| \propto d$.

$|\mathbf{v}| = d/t$ is satisfied for $n_{\text{ion}} = \phi(d/t)/t^3$ where $\phi(d/t)$ is an arbitrary function of d/t. This function can only be evaluated through numerical simulations of the system and is case-specific.

Before proceeding with the comparison of experimental and simulated ion kinetic energy distribution, we wish to make two remarks. First, recall that the validity of the single-fluid description of a plasma relies on the condition $\lambda_{\text{D}} \ll L$ where λ_{D} is the Debye length and L is the characteristic flow length. We have calculated λ_{D} and L for the late time case $t = 120\,\text{ns}$ and have found that $\lambda_{\text{D}} \approx 1 - 10\,\mu\text{m}$ and $L \approx 500\,\mu\text{m}$ in the vicinity of the density hump. These results validate the use of the quasi-neutral hydrodynamic approach in the current context. It is important to mention that the mechanism of ion acceleration in the other extreme case, i.e., plasmas in which $\lambda_{\text{D}} \gg L$ is often referred to as Coulomb explosion [36]. Second, recall that in the simulations the region outside the droplet is filled with a low-density tin vapour having $\rho = 10^{-12}\,\text{g\,cm}^{-3}$. The experiments, on the other hand, have been performed in a near-vacuum environment. This choice of density is sufficiently low as not to distort the vacuum-like expansion we wish to emulate in our simulations. This is evident in Fig. 2.6 where we do not observe a slowing-down of the peak velocity/shock front as the fluid propagates through the low-density background gas.

2.5   Ion kinetic energy distributions: experiment and simulation

We now wish to compare our measured ion energy distribution with that obtained from the simulations. These two quantities are compared in Fig. 2.7. The experimental data, shown in red, corresponds to the total ion energy distribution (also shown in red in Fig. 2.1) and the solid black curve is the ion energy distribution obtained from the RALEF-2D simulations. As described in Sec. 2.3.2, the RALEF-2D ion energy distribution is obtained by recording mass flow into two angular bins subtending an angle $55° < \theta < 65°$ with respect to the laser axis. From the two-dimensional computational mesh we have calculated the three-dimensional solid angle $\Omega_{\text{S}} \approx 0.95\,\text{sr}$ by revolving the arc length in the mesh around the laser axis. The RALEF-2D ion energy distribution, once corrected for this solid angle, is then convolved with bin-specific Gaussian functions having full width at half-maxima equal to 5% of the lower boundary of the energy bin. The purpose of this convolution is to account for processes which may broaden the distribution, e.g., mass distribution of tin isotopes.
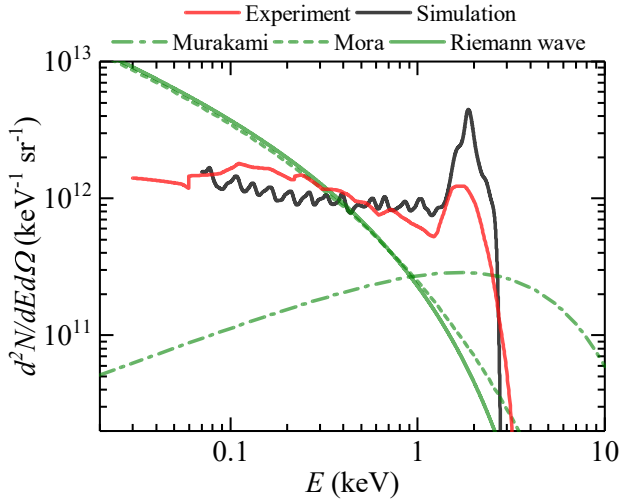
Figure 2.7: The distribution of the number of ions over ion kinetic energy. The experimental ion energy distribution is shown in red (solid curve) and the RALEF-2D ion energy distribution is shown in black (solid curve). Also illustrated are the predictions of the analytic models of Murakami (green dash-dot) [59], Mora (green dash) [60] and the Riemann wave (green solid) [49].

It is clear from Fig. 2.7 that the RALEF-2D ion energy distribution closely resembles the experimental measurements. First, the simulation reproduces the high-energy peak observed in the experimental data near 2 keV. This high-energy feature originates from fast-moving material associated with the quasi-spherical expanding shell (a tin ion with $|\mathbf{v}| = 57\,\mathrm{km\,s^{-1}}$ has a kinetic energy $E \approx 2\,\mathrm{keV}$).

Second, the simulations reproduce the near-constant behaviour of the experimental ion energy distribution in the $0.03 - 1\,\mathrm{keV}$ range. Fluctuations observed in the RALEF-2D ion energy distribution most likely arise from spatial fluctuations in the density and speed during the expansion (visible in Fig. 2.6 for $t = 120\,\mathrm{ns}$). Above 2 keV, both the simulations and experimental data exhibit a sharp fall-off with increasing kinetic energy. This fall-off is sharper in the case of the simulations, which does not predict any ions having kinetic energies above 3 keV. It is also interesting to note that, within the limits of the experimental uncertainties, the simulations provide a reliable prediction for the absolute number of ions detected in the experiments.

We show in Fig. 2.7 the predictions of the models of Murakami (Eq. (2.1)) and Mora (Eq. (2.2)). Guided by the work of Torretti *et al.* [18], we have taken $z = 12$, $k_B T = 35\,\mathrm{eV}$ and $N_0 = 2 \times 10^{12}$. For the model of Murakami we have chosen a spherical expansion ($\alpha = 3$) and a value $\ln\left(R(t)/R_0\right) = 4$. We also provide in Fig. 2.7 the ion energy distribution arising from a planar isentropic expansion, better

known as the Riemann wave [49]:

$$\frac{dN}{dE} = \frac{N_0}{zk_B T_e}\frac{\gamma^2 - 1}{4\gamma}\sqrt{\frac{E_{max}}{E}}\left(1 - \sqrt{\frac{E}{E_{max}}}\right)^{2/(\gamma-1)}. \tag{2.7}$$

Here γ is the adiabatic index (we select $\gamma = 4/3$ [102]) and $E_{max} = 2zk_B T_e\gamma/(\gamma-1)^2$ is the maximum ion kinetic energy. Both the planar isothermal expansion model of Mora and the Riemann wave solution predict a similar monotonic decrease in dN/dE with increasing E which is not observed in the experimental measurements. The shape of the experimental data is qualitatively better described by the spherical isothermal expansion model of Murakami, which exhibits a slow rise in dN/dE up to a peak at $E_{peak} = E_0/2 \approx 1.7\,\text{keV}$. The fall-off in dN/dE at energies above E_{peak} is far less steep compared to the experimental data.

The reason why the models of Murakami, Mora and the Riemann wave solution cannot be expected to reproduce the current experimental distribution ultimately lies in the plasma density profiles adopted in these analytic models.

The function $\phi(d, t)$ obtained with the RALEF-2D simulation is significantly more complex than the Gaussian or exponential density profiles assumed in the models of Murakami and Mora, respectively. It is the interaction of many complex processes (2D expansion of a non-uniformly heated, non-planar (radiating) plasma) that ultimately determines the function $\phi(d, t)$.

Four possible causes have been identified which may contribute to the observed differences between the experimental and simulated ion energy distributions. The first cause is the effect of numerical diffusion in the large mesh cells at larger mesh radii. This has been partly tackled by increasing the radial detail in the mesh at larger distances. The three other causes are inherent to the ansatz of the simulation code. As mentioned in Sec. 2.3.2, RALEF-2D uses Godunov's method for the Lagrangian phase of each hydrodynamic cycle. As the internal energy component of the total energy determines the pressure, rounding errors can propagate especially if the internal energy is small. A third possible cause is related to the EOS model employed by RALEF-2D. The EOS model adopted in this work assumes LTE ionization throughout the entire simulation. This assumption breaks down at late times in the expansion when ionization and recombination processes cease to exist, leading to the well-known "freezing" of charge states [84].

We note that the simulated domain (10 mm) is much smaller than the experimental flight path (~ 1 m) and the assumption is made that neither the experimental or simulated ion energy distributions change significantly between the two distances. This assumption is supported by two arguments: (1) Within the simulated spatial

scale the velocity profile attains its asymptotic, triangular shape before leaving the mesh, having converged to the late-time behaviour; (2) On the experimental side the aforementioned freezing of charge states will occur on a length scale similar to that of the simulation spatial scale [84] and, thus, that in our high-vacuum environment no significant changes over the remaining flight path will occur.

Keeping these remarks in mind, the results presented in this chapter demonstrate that the single-fluid single-temperature approach implemented in RALEF-2D can (i) reproduce the general shape of the experimental ion energy distribution and (ii) provide a reliable prediction for absolute number of ions detected in the experiments.

2.6 Conclusion

We have undertaken a joint experimental and theoretical study of plasma expansion arising from Nd:YAG laser irradiation of tin microdroplets. The experimentally-recorded ion energy distribution is found to exhibit a complex, non-monotonic dependence on ion kinetic energy. Charge-state resolved measurements of the ion energy spectra reveal the existence of peaks centered near $2\,\text{keV}$ in the Sn^{3+} – Sn^{8+} distributions. Two-dimensional radiation-hydrodynamic simulations performed using a single-fluid single-temperature approach are shown to reproduce the overall shape of the experimentally-recorded ion energy distributions and provide a reliable prediction for the absolute number of ions detected in the experiments. The existence of a peak in the experimental ion energy distribution near $2\,\text{keV}$ is attributed to the formation of a quasi-spherical expanding shell at early times in the plasma expansion. Our interpretation of the plasma dynamics in terms of two distinct bursts of laser-induced ablation indicates that the observed ion energy distribution would in general be sensitive to the temporal profile of the laser pulse. The results of the present work are therefore specific for a Gaussian temporal profile with a laser intensity varying on the timescale of about $10\,\text{ns}$.

Acknowledgements

3

Strongly anisotropic ion emission in the expansion of Nd:YAG-laser-produced plasma

Lucas Poirier[†], Diko J. Hemminga[†], Adam Lassise, Luc Assink, Ronnie Hoekstra, John Sheil, and Oscar O. Versolato

We present results from a combined experimental and numerical simulation study of the expansion of a laser-produced plasma into vacuum. Plasma is generated by Nd:YAG laser pulse impact (laser wavelength $\lambda = 1.064\,\mu$m) onto tin microdroplets under conditions relevant for extreme ultraviolet lithography. Measurements of the ion kinetic energy distributions under a multitude of angles reveal strongly anisotropic emission characteristics, in close agreement with two-dimensional radiation-hydrodynamic simulations. The angle-resolved ion spectral measurements further enable the accurate prediction of the plasma propulsion of the laser-impacted droplet.

[†] Lucas Poirier and Diko Hemminga contributed equally to this chapter as part of their PhD theses.

[*] Diko Hemminga contributed to this chapter as part of his thesis regarding conceptualization, formal analysis, investigation through performing simulations, visualization, and both writing of the first draft and writing, review and editing of the final draft.

3.1 Introduction

State-of-the-art nanolithography relies on 13.5 nm extreme ultraviolet (EUV) light that is generated from laser-produced tin plasma (LPP) [17, 28, 34]. Expansion of the hot and dense tin plasma may hinder EUV source operation in several ways, notably in the form of fast plasma ions that may damage or coat EUV optics [6]. Effective mitigation schemes are required to rid the EUV generation of such adverse processes. These mitigation schemes may, e.g., involve buffer gases aimed to stop and remove the ionic debris, or use strong magnetic fields to guide the tin ions [6, 103]. Designing such mitigation strategies benefits from the understanding of the driving mechanisms of the plasma expansion in the absence of any such mitigation effects.

Analytical models of plasma expansion into the vacuum have previously been developed [36, 58, 60], also were applied to the specific case of tin laser-produced plasma [59, 61]. More recently, two-dimensional radiation-hydrodynamic simulations, using a single-fluid single-temperature approach, were performed with the aim of further clarifying the expansion physics as it was found that the strongly simplified analytical models were unable to fully capture the expansion. The simulations were shown to accurately reproduce the ion energy distributions as obtained from experiments in a single direction: under a 60° angle backwards towards the laser [104]. A prominent peak in the experimental ion energy distribution was attributed to the formation of a quasi-spherical expanding shell at early times in the plasma expansion [104]. The interpretation of the plasma dynamics in terms of a complex interplay between two directional bursts of laser-induced ablation [104], requiring that the plasma expansion and the resulting ion kinetic energy spectra are highly anisotropic.

The importance of a thorough understanding of tin LPP angular ion emission motivated several detailed experimental studies on the topic, using electrostatic probes [105, 106], Faraday cups [20, 84], electrostatic analyzers [81, 84, 107], retarding field analyzers[108], and Thompson parabolas [20]. Many studies observed anisotropy in the charge-integrated [20, 84, 105, 109, 110] and in the charge-resolved ion emission into a buffer gas [81, 107]. Kools *et al.* [109] and others[111, 112] produced analytical expressions for the integral ion current, which were later built upon [113] to derive the angular dependence of the ion charge yield. This angular dependence was found to resemble a cosine power law [84, 113] (also see Qin *et al.* [110]). Brandstatter *et al.* [105], O'Connor *et al.* [80], and Giovannini *et al.* [81] found clear dependencies of the charge-resolved average ion energy and of the average peak velocity on the emission angle, providing important insights. Thus far, however, no

combined absolute angle- and charge-state-resolved kinetic energy measurements have been performed on a tin-microdroplet-based plasma freely expanding into the vacuum.

We present a study of angle-, energy-, and charge-resolved absolute ion yields, using compact retarding field analyzers (RFAs) set up under several angles. Our measurements are compared to single-fluid radiation-hydrodynamic simulations performed using the RALEF-2D code. In the following, first, we briefly describe the experimental setup and methods used as well as the corresponding RALEF-2D simulations. This is followed by a detailed discussion of the ion emission anisotropy and the features and trends observed in the ion spectra comparing the experiments with simulations supported by analytical theory. We define several relevant metrics related to the ion emission (ion number, momentum, energy), and report their value. Lastly, we utilize the measured ion momentum to accurately predict the propulsion speed of the laser-impacted droplets over a wide experimental parameter range.

3.2 Experiments

3.2.1 Experimental setup

The experimental setup is described in detail in earlier work [25]. Here, we recall the main elements. A tin tank is mounted on top of a vacuum chamber ($\sim 10^{-7}$ mbar), and is kept at 260°C — above the melting temperature of tin. The tank is pressurized with argon gas to push the molten tin through a nozzle. Tin droplets with a well-defined diameter of $d_{\mathrm{drop}} = 27\,\mu\mathrm{m}$ are dispensed by the nozzle at kHz frequencies (in Sec. 3.4.3 also $d_{\mathrm{drop}} = 17\,\mu\mathrm{m}$ droplets are discussed). The microdroplets next intersect a horizontal laser sheet produced by a helium-neon laser beam coupled into a cylindrical lens. Light scattered by the droplet when traversing the laser sheet is collected by a photomultiplier tube (PMT). The PMT signal is down-converted to 10 Hz; this down-converted signal is used as trigger to synchronize the impact of a seeded 10 Hz Nd:YAG laser pulse with the droplets. The laser pulses have a wavelength of 1064 nm, a Gaussian spatial profile with a full width at half maximum (FWHM) of 100 μm, and a Gaussian temporal profile with a FWHM of 10 ns. The pulse energy can be tuned using a $\lambda/2$ waveplate in combination with a polarizer.

FC73-A Faraday cups (FCs) from Kimball Physics were used to characterize the charge and energy of the ions emitted from the LPP. FCs record the ion current as a function of the time of flight (ToF). Ion kinetic energies are calculated using the time of flight and the length of flight d of ions, assuming ballistic motion. The time-of-flight ion current is converted to a time-dependent voltage thanks
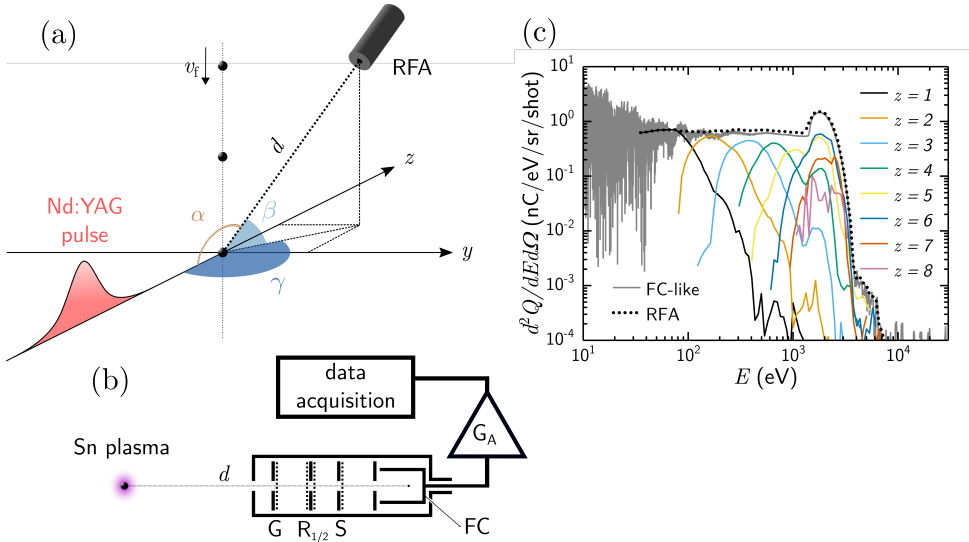
Figure 3.1: Sketch of experimental setup. (a) Droplets travel with velocity v_f until they are illuminated by the Nd:YAG laser pulse. The position of a RFA is defined by its distance to the LPP (d) and the angle (α) between the direction towards the RFA and the negative z-axis, the symmetry axis of the incoming laser pulse. This angle α calculated from the azimuth (γ) and the elevation (β) of the RFA with respect to the laser axis. (b) The main elements of the RFA are shown; four grids (G, R_1, R_2 and S) are located in the path of the tin ions. The ion current in the Faraday cup (FC) is amplified (denoted by G_A) and recorded by an oscilloscope. (c) A sample charge-resolved ion energy spectrum taken with an RFA is presented; the sum of the different charge states (z = 1–8, black dotted line) overlaps with a charge-integrated spectrum (gray line; "FC-like" [114]) taken at the same position as the RFA spectrum.

to a trans-impedance amplifier (600 MHz Keysight Infiniium) with a broad bandwidth of 25 MHz (G_A in Figure 3.1(b)). When the output impedance of our oscilloscope is matched with that of the amplifier (50 Ω), the amplifier gain becomes 25 kV/A. Further information can be found in Poirier *et al.* [114]. The detectors feature four grids, namely a reference grounding grid G, two retarding grids R_1 and R_2, and a suppressing grid S (see Figure 3.1(b)). The suppressing grid is biased negatively ($U_{supp} = -100$ V) in order to repel back into the Faraday cup any secondary electrons produced from the surface of the Faraday cup. The cup itself is biased ($U_{bias} = -30$ V) to prevent plasma electrons from entering the cup. The electrostatic field applied to the retarding grids of the device is scanned to unravel the charge state of detected ion, in the so-called "retarding field analysis" (RFA) mode. The two retarding grids share the same positive potential U_{ret} and are separated by a 500 μm gap. Scanning U_{ret} from 0 V up to 1 kV, an increasing amount of positively charged ions with charge ze and energy E emanating from the plasma are repelled when $E < zeU_{ret}$. An iterative post-processing of the ion currents allows for the unravelling of charge-resolved ion energy spectra. The post-processing scheme was explained in detail in Ref. [114], an earlier study in a very similar context.

Seven RFAs were placed at various angular positions around the plasma. The angular position of the RFAs with respect to the vacuum chamber is described by their elevation (β) and azimuth (γ) with respect to the laser axis, as illustrated in Figure 3.1(a) and listed in Table 3.1 in the Appendix. The cylindrical symmetry of the laser-droplet system enables defining the direction of the RFAs by a single angle α through $\alpha = \cos^{-1}(\cos(\gamma)\cos(\beta))$. The aperture of an RFA has a diameter of 5 mm and is located at a distance d from the point-like plasma, defining the solid angle of the aperture $\Delta\Omega$ (see Table 3.1 in the Appendix). It was shown previously in Ref. [87] that an RFA with four maximally misaligned grids has a transmission of 41%. We later obtained from detailed simulations [115], that the transmission of the four-grid stack intricately depends on the co-alignment of the grids, the energy of the ions, and the electrostatic bias on each grid. From our simulations, stack transmission was found to range between 41% (in case of maximally misaligned grids, consistent with our previous results [87, 114]) and 82% (in case of geometrically overlapping grids with maximum alignment). In the following, we therefore take a representative and average transmission of 60% for all RFAs, with a systematic error of 20% covering the range of possible extreme cases of grid alignment.

3.2.2 Experimental methods

The so-called bottom-up method is used to derive charge-resolved ion spectra from ion time-of-flight current traces via a retarding voltage scan. The process is described in detail by Poirier *et al.* in Ref. [114]. Here, U_{ret} is set to 61 equally spaced values between $U_{\text{ret,min}} = 0\,\text{V}$ and $U_{\text{ret,max}}$, depending on the maximum retarding voltage required to negate the total ion current. Indeed, $U_{\text{ret,max}}$ must be at least equal to $E_{\text{max}}/z_{\text{max}}$, where E_{max} and z_{max} are, respectively, the highest ion energy and charge state detected for a given experiment. In the presented experiment, a maximum retarding voltage of $1\,\text{kV}$ was found to be adequate. We record ion currents for several hundred laser shots for each of the retarding voltages and use the average ion current throughout the analysis, as to enhance the signal-to-noise ratio. Outlying single-shot ion currents are discarded when the velocity of the leftover liquid tin target observed via simultaneous single-shot shadowgraphic imaging falls beyond $\pm 5\%$ of the average observed target velocity (cf. Ref. [25, 98]).

A typical ion energy distribution measured with the aforementioned experimental parameters is presented in Figure 3.1(c); here the laser energy was set to $99\,\text{mJ}$ and the droplet size to $27\,\mu\text{m}$. The laser transmission of the vacuum chamber input window was measured to be 97%. The charge-state-resolved distributions ($z = 1\text{--}8$) of charge $d^2Q_z/dEd\Omega$ are presented and the sum of contributions from all charge states (black dotted line) overlaps with a Faraday-cup-like charge-integrated measurement (gray line) recorded separately, but at the same detection angle α. In the following, we present the total ion energy number distributions $d^2N/dEd\Omega$ — representing the hydrodynamic mass flow — by accounting for the individual charge states Q, using the charge-state-resolved data [104]. A confidence interval is introduced to account for the systematic errors in estimating ion measurements. A first contribution to this confidence interval covers the influence of late-time baseline subtraction, where we follow Ref. [114]. A second contribution accounts for the 20% systematic error on the transmission of the four RFA grids (cf. Sec. 3.2.1). In the following, the confidence interval based on these two effects is displayed in figures and taken into account wherever relevant metrics are presented.

3.3 Radiation-hydrodynamic simulations

3.3.1 RALEF-2D

The RALEF-2D code and its application to the case of tin laser-produced plasma was presented in detail in earlier publications on plasma expansion [104] and propulsion

of the remaining mass [116]. RALEF (Radiation Arbitrary Lagrange–Eulerian Fluid dynamics) is a two-dimensional (2D) radiation-hydrodynamic finite element solver fit for the simulation of laser-produced plasmas. The code solves the single-fluid and single-temperature hydrodynamic equations with inclusion of energy transport by thermal conduction and radiation.

The solution of the radiation transport equation is based on spectral absorption coefficients generated with the THERMOS code [40] and the equation-of-state (EOS) of tin used is known as the Frankfurt EOS (FEOS) [52]. In the presented simulations the so-called hybrid model for laser light propagation is employed [39]. It accounts for laser absorption, reflection, and refraction in the corona of the plasma. With this choice we operate a model of laser propagation that is identical to our last work, on droplet propulsion and deformation [116], but one that is more complete when compared to our previous work on plasma expansion [104].

3.3.2   Application of RALEF-2D

The experimental laser-droplet parameters serve as input to the radiation-hydrodynamic simulations with RALEF-2D. The presented simulations are performed using a 1064 nm laser pulse with a Gaussian temporal profile with a FWHM of 10 ns, similar to the simulation presented in Hemminga *et al.* [104]. In this work, the spatial laser profile is modeled by a Gaussian of 100 μm (FHWM) and the droplet diameter is set to 27 μm. In fact, the experimental spatial profile of the laser is an Airy disk, which we approximate to be a Gaussian profile in the simulation; we set the simulated pulse energy to be 90 mJ so that the simulated laser pulse has the same energy within a radius of FWHM/2. The radiation-hydrodynamic simulations are performed on a two-dimensional computational mesh of quadrilateral cells. We chose a domain similar to our previous work [104]: a half-disk geometry with a radius of 10 mm. The cylindrical symmetry axis is defined as reflective, while the curved boundary of the half-disk allows for free-outflow of material. This outflow is used for extraction of the numerical ion energy distributions in this work.

3.3.3   Ion distributions from simulation

The method for extracting ion energy distributions $d^2N/dEd\Omega$ from the simulated hydrodynamic mass flow is based on allocating the outflowing mass to predefined kinetic energy and angle intervals. It has been detailed in Ref. [104]. This allocation is based on the magnitude and direction of the velocity of the outflowing mass, as related to kinetic energy and angle, respectively. In the presented simulations, 360
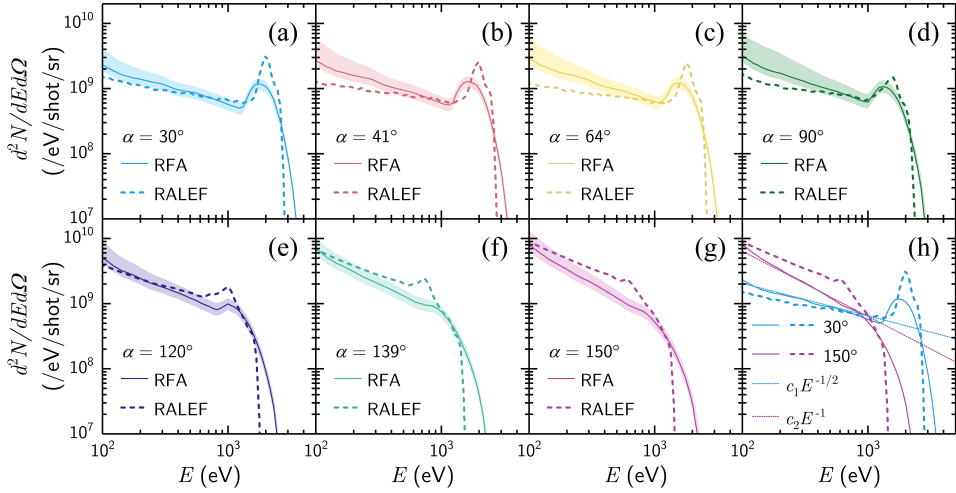
Figure 3.2: Ion energy distributions measured by the RFAs (solid lines), and modeled by RALEF-2D (dashed lines) are separately shown for each of the seven measurement angles (a–g). Error bars discussed in Sec. 3.2.1 are depicted by the colored shading. In the bottom-right panel (h), the RFA and RALEF-2D spectra are overlapped for a small and large angle to emphasize the shifting spectral features; the dotted lines show power laws for the front ($\alpha = 30°$) and back ($\alpha = 150°$) side (see main text).

3

exponentially scaling energy bins are used over the interval between 1 and 20 keV. In angular space, 180 equally sized bins are used over 180°. The angularly resolved ion kinetic energy distributions are processed in three steps. Supplementing the analysis in our previous work [104], we first take an average over a set of nine simulation runs with identical input parameters. Secondly, similar to our previous work, we average the distributions over an angular range of 10° around the experimental angles, i.e., $\alpha \pm 5°$. We weight the average calculation with the respective solid angles of each bin. The angular distributions are based on these data and have an effective 10° running average applied. Thirdly, we apply a convolution by the experimental energy resolution. The energy resolution used matches that of the RFA detectors and is equal to $\Delta E/E = 8\%$, as determined in an earlier study [114]. The calculation is based on a convolution of the ion kinetic distribution histogram with a Gaussian function with FWHM $= \Delta E$ and an area of unity.
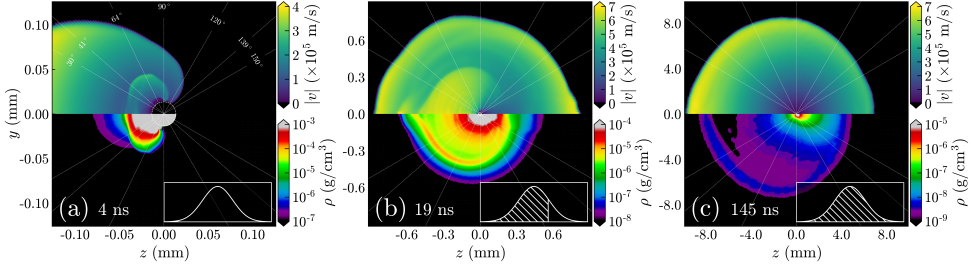
Figure 3.3: Two-dimensional profiles of ion speed $|v|$ (upper-half panel) and mass density ρ (lower-half panel) are presented for different time steps throughout the LPP expansion. The fraction of absorbed laser light at each time step is pictured in the bottom-right corner inset. White dotted lines indicate the positions of the seven RFAs.

3.4   Results and discussion

3.4.1   Ion emission anisotropy

Total ion energy distributions $d^2N/dEd\Omega$ by RFAs at seven different angles with respect to the laser axis, are presented in Figure 3.2 (solid lines in (a–g)). First, a high-energy peak can be identified in the experimental distributions in Figure 3.2, as also previously reported [87, 104, 114]. The local maximum of this peak lies between 500 and 1000 eV depending on the detection angle α and is most prominent in the spectra from the front side ($\alpha \leq 90°$). Spectra at the back side ($\alpha > 90°$) do not strongly feature a peak and instead exhibit a near-monotonic decrease of ion number for increasing energy. In relative terms, the front side experiences the emission of a higher number of high-energy ions ($E > 400\,\text{eV}$) than the back side, which collects a higher number of low-energy ions ($E < 400\,\text{eV}$). For all angles, the spectra exhibit a power-law type fall-off up to the peak feature.

Results from RALEF-2D simulations are presented in Fig. 3.2 alongside the experimental data. With the results in Figure 3.2 the comparison between experimental and simulated ion energy spectra is extended from 60° in Hemminga *et al.* [104] to a multitude of measurement angles. The resemblance is similar: the general shapes of the experimental front-side spectra are reproduced by the simulations, including the peaked high-energy feature [104]. In addition, the simulated spectra follow a similar angular trend where the position of the high-energy peak shifts to lower energy while reducing in amplitude. The overall agreement between simulations and experiment in Fig. 3.2 validates use of the single-fluid approach [104] for the full 3D expansion.

The spectral shape with a high-energy peak was investigated in Hemminga *et al.* [104] for a single, 60° measurement angle. The peak was associated with a density shell forming during the expansion. In the following we argue, using our simulations, that the observed ion emission anistropy can be explained by the fact that this density shell is intrinsically anisotropic.

In Figure 3.3, we present the ion speed $|v|$ (upper panel) and mass density ρ (lower panel) profiles for three time steps in the simulation. These time stamps (4, 19, and 145 ns) refer to the time since the beginning of the simulation which is chosen 15 ns prior to the occurrence of the laser intensity maximum. As inset in each panel the temporal profile of the laser pulse is sketched; the hatched area represents the portion of laser energy added to the system up to that time. The angular positions of the seven RFAs used in the experiment are indicated by radial white dashed lines.

At $t = 4$ ns, only a small fraction of the Gaussian temporal pulse has illuminated the droplet, as shown in panel (a). The high-density burst close to the droplet surface, for $d < 0.05$ mm, is equivalent to the initial burst of ablation described in our previous work [104]. We note an angularly directed flow around the droplet. It is the first indication of the continuous flow of laser-ablated material around the droplet. This is the result of the pressure gradient from the laser-produced plasma to the vacuum behind the droplet, and the phenomenon continues for the subsequent expansion.

At $t = 19$ ns, as shown in Figure 3.3(b), the main feature is a high-density shell. As previously described by the authors [104], such a density shell is formed by the interaction of two ablation bursts. The first burst is that of the aforementioned initial ablation, and the second is formed by the hot and dense plasma generated by the laser pulse near peak intensity, producing high speeds. This second ablation burst interacts with material from the initial ablation, and forms a density shell at its front. While the initial ablation burst is expanding radially outwards in all directions, this second ablation is highly direction, mainly expanding towards the $\alpha = 0 - 90°$ half-plane. As a result, the density shell inherits this angular dependence, and becomes *quasi*-spherical. In comparison to the simulation presented in Ref. [104], the current inclusion of laser beam refraction leads to minor spatial fluctuations in the formed plasma ($d < 0.15$ mm), both in speed and density. However, at late time ($t = 145$ ns, panel (c) of Figure 3.3), these fluctuations in the region of the high-speed density shell have faded out and we find convergence to a similar expansion profile as in Ref. [104].

Next, profiles (lineouts) of speed and density are extracted from the two-dimensional simulation data along radial lines towards the seven RFA positions at $t = 145$ ns, as presented in Figure 3.4. The angular dependence of the quasi-spherical density shell
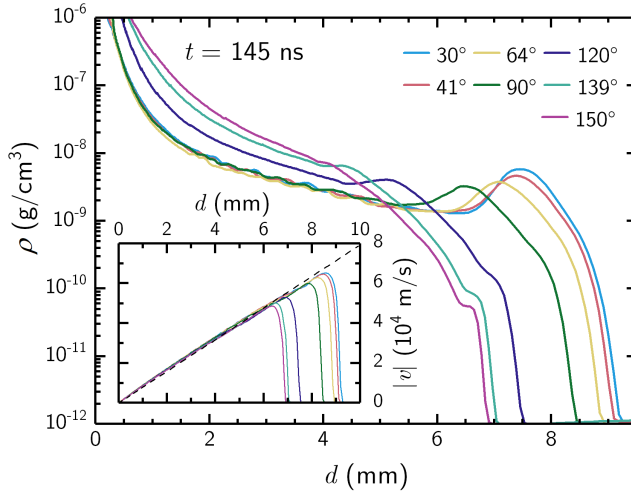
3

Figure 3.4: Radial lineouts of the ion density profiles calculated by RALEF-2D are shown for the angles at which RFAs were placed in the experiment, 145 ns after the start of the simulation. The inset shows the complementary velocity profiles, exhibiting their characteristic linear behaviour, which is exemplified by a ballistic curve shown as reference by the dashed line.

is clearly visible: the peak in the density profiles decreases in height and shifts to shorter distances with angle. The linear dependence of the local flow speed on distance (inset Fig. 3.4) follows the relation $v/d = 1/(t-t_0) \approx 7.7 \times 10^6$ s^{-1} (evaluated at $t = 145$ ns with $t_0 = 15$ ns set at the maximum laser intensity).

Combining density and speed profiles enables obtaining, and explaining the ion energy distributions. In particular, we can interpret the power-law type behavior (up to the peak feature) seen in the spectra in Fig. 3.2 in terms of the underlying density profile. Figure 3.2(h) presents power-law fits $d^2N/dEd\Omega \propto E^\eta$ to two selected observation angles. The sole free parameter in the fit is the overall amplitude (offset in log-log representation). For the $\alpha = 30°$ angle a power $\eta = -1/2$ is seen to accurately capture the power-law fall-off, whereas $\eta = -1$ recovers the behavior for $\alpha = 150°$. We note that the distributions at intermediate angles can be described by intermediate powers η.

The origin of these power laws can be understood from an analytical ansatz based on a linear speed profile and an inverse power law density profile in three dimensions: $v \propto r$, $\rho \propto r^{-n}$, with radial coordinate r, and volume $V \propto r^3$. Omitting the explicit solid angle dependence, the expression for the ion energy distribution

dN/dE becomes

$$\frac{dN}{dE} \propto \frac{\rho dV}{v dv} = E^{(-n+1)/2}, \tag{3.1}$$

where the relation $r \propto v \propto E^{-1/2}$ is applied. The experimental power laws can be related to analytical density profiles in the following way: $\eta = -1/2$ ($\alpha = 30°$) corresponds to $n = 2$ and $\eta = -1$ ($\alpha = 150°$) to $n = 3$. This suggests that towards $\alpha = 150°$ the tin fluid rarefies according to its increase in volume $\propto r^3$ with time. For purely radial flow described by a linear speed profile (cf. inset Fig. 3.4), the density profile $\rho \propto 1/r^3$ is a time-independent solution of the continuity equation, conserving the product $\rho v r^2$. Towards $\alpha = 30°$ the behavior is consistent with that observed in Ref. [51] where $\rho \propto 1/r^2$ is associated with a steady spherical flow for constant v near the critical surface [51].

Finally, we may partially attribute the remaining differences between experiment and simulation to the completeness of the employed simulation model, which cannot fully capture imperfect experimental conditions. The experimental spectra consistently exhibit a more gradual fall off towards higher kinetic energies than is seen in the simulations, which may be caused by high-intensity regions in the laser beam profile or incompleteness of the RALEF-2D physical model. Further study is required to address these points.

3.4.2 Angular distributions of number, momentum, and energy

The overall number of ions, and the total momentum and energy balance of an LPP are important metrics, especially in the industrial context of the production of debris in the EUV light generation process. For the experiment, we use our angular coverage of the axisymmetric LPP to interpolate the captured data, in order to provide an estimate of the total ion emission in 4π sr. For this purpose we work with energy-integrated spectra. In the spectral integration the low-energy integration boundary $E_{\min}$ is set to $60\,\text{eV}$ to match the lower bound of the simulation. Per unit solid angle, the total ion number, total radial ion momentum, and total ion energy are calculated using

$$\frac{dN_{\text{tot}}}{d\Omega} = \int\limits_{E_{\min}}^{\infty} \frac{d^2N}{dEd\Omega} dE', \tag{3.2}$$
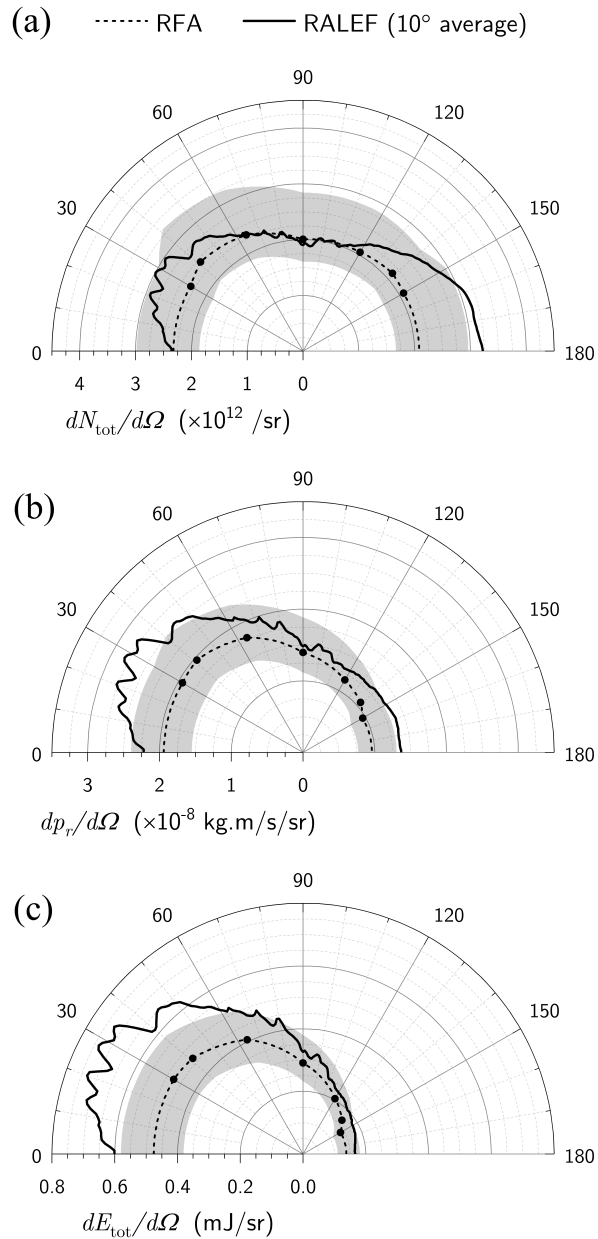
Figure 3.5: Angular distributions of ion (a) number, (b) momentum and (c) total energy, as calculated using the ion energy spectra from RFA measurements (black circles) and from RALEF-2D simulations (solid black line). In the three panels, the seven-point RFA data sets were interpolated and extrapolated as a guide to the eye (black dashed line). The gray bands around the RFA distributions represent the confidence intervals (see Sec. 3.2.1). The RALEF-2D distributions include a 10° running average.

$$\frac{dp_r}{d\Omega} = \int\limits_{E_{\min}}^{\infty} p_r(E') \frac{d^2N}{dEd\Omega} dE', \tag{3.3}$$

$$\frac{dE_{\text{tot}}}{d\Omega} = \int\limits_{E_{\min}}^{\infty} E' \frac{d^2N}{dEd\Omega} dE', \tag{3.4}$$

where $p_r(E) = \sqrt{2mE}$ is the momentum of a single tin particle with mass m, assumed to move only in the radial direction. Since tin has ten stable isotopes, we use the abundance-weighted average mass of 118.71 amu for m.

The angular distributions of N_{tot}, E_{tot}, and the magnitude of the momentum vector, p_r, are shown in Figure 3.5. The gray bands surrounding the RFA data delineate the confidence intervals of the distributions. These confidence intervals are derived from uncertainties in the transmission of the RFA grid configuration and in the choice of the baseline subtraction method. For the numerical counterpart, the values defined in equations (3.2 – 3.4) are calculated in the same manner, for every 1° α-wise bin. All three distributions underwent a 10° running average, but non-physical features remain visible in the angular distributions. Numerical velocity fluctuations in the vicinity of the droplet – both in magnitude and direction – impact the expansion further radially outwards. At such distances these velocity fluctuations lead to angular density fluctuations. For example, this is visible inside the quasi-spherical density shell visible in Figure 3.3(c). However, the remaining features have little impact on the overall size and shape and we conclude that the numerical distributions are in good agreement with the experimental distributions.

Next, the 4π-integrated metrics are calculated using interpolated data, integrating over the entire sphere exploiting the cylindrical symmetry. The required extrapolation of the distributions below $\alpha = 30°$ and above 150° assumes constant values, equal to the closest measurement entry. For the RFA measurements presented in Figures 3.2 and 3.5, we estimate the total number of ions to be $N_{\text{tot}} \approx 2.7 \times 10^{13}$. The fraction f_N of the measured number of ions to the total number of ion atoms present in the initial droplet is 7.4%. The total energy carried by ions with $E > 60$ eV in the experiment is $E_{\text{tot}} = 3.8$ mJ. From the RALEF-2D simulations we find a total ion number of 3.0×10^{13}, that is a fraction $f_N = 8.1\%$ of the total tin atoms, closely matching the experimental value. The total kinetic energy of 4.9 mJ is slightly higher than the experimental value, but well within the uncertainty limits. The momentum imbalance is discussed separately in the following section.

3.4.3 Droplet plasma propulsion

The net momentum imbalance p_z in the ion emission, oriented along the z-axis given the cylindrical symmetry, equals the momentum imparted on the remaining liquid mass noting that the momentum carried by the incident laser photons is only a small fraction of this momentum imbalance [25]. Thus, our ion emission measurements enable the prediction of the plasma propulsion velocity of the liquid drop that was previously studied by Kurilovich *et al.* [25].

For the experiment presented in Figures 3.2 and 3.5, the net projected momentum is $p_z = 2.4 \times 10^{-8}$ kg m/s. With the estimate of the remaining molten tin mass, using our RFA data to assess the mass loss (thereby implicitly excluding mass loss in the form of neutral atoms), we obtain a propulsion velocity of the target $v_{\mathrm{t,RFA}}$ of 360(70) m/s as inferred from the ion momentum imbalance. Integrating the experimental values to 30 eV instead yields a similar velocity of 348(70) m/s. In the same manner for the numerical modelling, we find a momentum imbalance of 3.3×10^{-8} kg m/s leading to a propulsion speed of 449 m/s.

The target velocity is also assessed directly by recording a high-resolution single-shot shadowgraphy image of the target a few μs after the laser-droplet impact. The shadowgraphy imaging scheme and methods are outlined in detail in the Refs. [25, 98, 117, 118]. The target propulsion velocity v_{t} is assessed stroboscopically by scanning the delay Δt and obtaining the position of the center of mass, Δx, such that assuming ballistic motion, we find $v_{\mathrm{t}} = \Delta x / \Delta t$ [25, 98]. This technique yields an average propulsion velocity of 337 m/s, in excellent agreement with the ion momentum balance approach.

In the RALEF-2D simulation, the shadowgraphy measurement of velocity is best compared to the center-of-mass (COM) velocity of the tin fluid 300 ns after the start of the simulation. Only mesh cells with a density in excess of the threshold value $\rho_{\mathrm{thr}} = 1$ g/cm^3 are taken into account for the COM velocity calculation. This method yields a velocity of 435 m/s, close to the 449 m/s value from the momentum imbalance approach above. The simulations thus predict a propulsion velocity somewhat larger than found in the experiment (consistent with Refs. [25, 98, 116]). We note that the accuracy of the prediction of the droplet propulsion by simulations using RALEF-2D was validated separately over a large parameter space in previous works [25, 116–118].

Now that we have established the accuracy of the ion measurements for a single experimental parameter set through the accurate prediction of the propulsion speed of the laser-impacted droplet using momentum conservation we next vary the laser pulse energy and droplet size in the experiments. Specifically, laser pulse energies
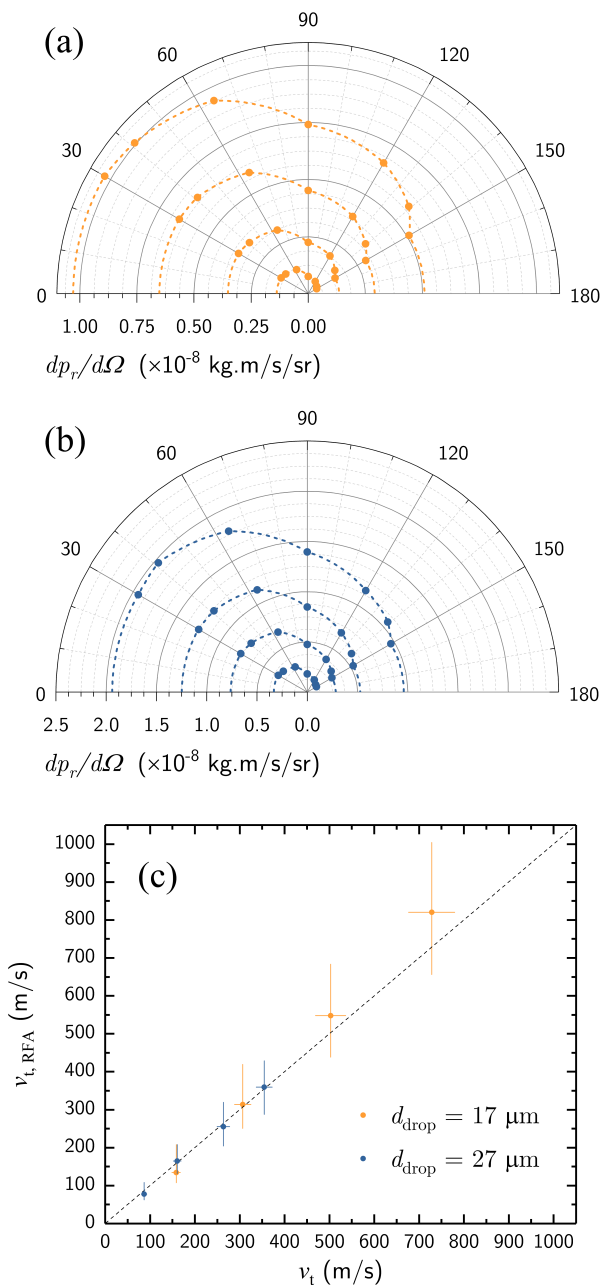
Figure 3.6: Angular dependence of the momentum carried by ions for a small [(a) $d_{\mathrm{drop}} = 17\,\mu\mathrm{m}$, orange markers] and a large [(b) $d_{\mathrm{drop}} = 27\,\mu\mathrm{m}$, blue markers] droplet. The four data sets correspond, with increasing momentum, to laser pulse energies equal to 8, 26, 60, and 100 mJ. Droplet velocities measured through shadowgraphy (v_{t}), and calculated using the momentum imbalance ($v_{\mathrm{t,RFA}}$), are compared in panel (c). The dashed diagonal line denotes $v_{\mathrm{t,RFA}} = v_{\mathrm{t}}$.

of 8, 26, 60, and 100 mJ are used to irradiate droplets with sizes $d_{\mathrm{drop}} = 17$ and 27 µm. Figures 3.6(a,b) present the momentum anisotropy for the various laser energies separately for each droplet size case. Figure 3.6(c) compares the results of the propulsion speed inferred from the momentum balance $v_{\mathrm{t,RFA}}$ with the propulsion speed obtained from shadowgraphy v_{t}. We find that the excellent agreement holds over the full probed experimental parameter space, which includes settings directly relevant for the industrial use case. Momentum imbalance measurements may thus be applied to serve as diagnostics for droplet propulsion and, the strongly correlated [116], deformation in state-of-the-art nanolithography tools.

3.5 Conclusion

We presented results from experimental and numerical studies of the anisotropy in the expansion of a tin-microdroplet-based laser-produced plasma into vacuum. Plasma was generated by nanosecond Nd:YAG laser pulse impact (laser wavelength $\lambda = 1.064$ µm) onto tin microdroplets. Measurements of the ion kinetic energy distributions were performed using retarding field analyzers set up under several angles. These measurements revealed strongly anisotropic emission characteristics, in close agreement with two-dimensional radiation-hydrodynamic simulations that we performed using the RALEF-2D code. The ion emission spectrum features a high-energy peaked that was previously explained in terms of a complex interaction between two ablation fronts. In the present work, this interaction was shown to lead to highly anisotropic features. A monotonic decrease visible in the emission spectra right up to the high-energy peak was explained in terms of a power-law drop in density with the radial coordinate, consistent with existing models of rarefaction. The angle-resolved ion spectral measurements were further shown to provide a very precise prediction of the propulsion of the droplet by the plasma generated from laser-pulse impact.

Acknowledgements

Appendix

The position of and the solid angle covered by the seven RFAs are summarized in Table 3.1 in terms of their elevation (β) and azimuth (γ) with respect to the laser axis (see Fig. 3.1(a)). The cylindrical symmetry of the laser-droplet system defines the angular position of any RFAs by a single angle α (see main text).

Table 3.1: RFA position and coverage. Elevation angle (β) and azimuth (γ) with respect to the laser axis yield the angular position by a single angle α (see main text). RFAs are placed at a distance d from the plasma, and cover a solid angle $\Delta\Omega(d)$.

α (°)	β (°)	γ (°)	d (mm)	$\Delta\Omega$ (μsr)
30	0	30	420	111
41	-30	330	420	111
64	30	60	420	111
90	30	270	420	111
120	0	120	296	224
139	-30	210	296	224
150	30	180	296	224

3

4

Early-time hydrodynamic response of a tin droplet driven by laser-produced plasma

Javier Hernandez-Rueda, Bo Liu, Diko J. Hemminga, Yahia Mostafa, Randy A. Meijer, Dmitry Kurilovich, Mikhail Basko, Hanneke Gelderblom, John Sheil, and Oscar O. Versolato

We experimentally and numerically investigate the early-time hydrodynamic response of tin microdroplets driven by a ns-laser-induced plasma. Experimentally, we use stroboscopic microscopy to record the laser-induced dynamics of liquid tin droplets and determine the propulsion speed (U) and initial radial expansion rate ($\dot{R}_0$). The ratio of these two quantities is a key parameter to be optimized for applications in nanolithography, where laser-impacted tin droplets serve as targets for generating extreme ultraviolet light. We explore a large parameter space to investigate the influence of the tin droplet diameter, laser beam diameter and laser energy on the $\dot{R}_0/U$ ratio. We find good agreement when comparing the experimentally obtained U and $\dot{R}_0$ values to those obtained by detailed radiation-hydrodynamic simulations using RALEF-2D. From the validated simulations, we extract the spatial distribution of the plasma-driven pressure impulse at the droplet-plasma interface to quantify its

4

---

[*] Diko Hemminga contributed to this chapter as part of his thesis regarding formal analysis, investigation through performing simulations, and both writing of the first draft and writing, review and editing of the final draft.

influence on the partitioning of kinetic energy channeled into propulsion or deformation. Our findings demonstrate that the width of the pressure impulse is the sole pertinent parameter for extracting the kinetic energy partitioning, which ultimately determines the late-time target morphology. We find good agreement between our full radiation-hydrodynamic modeling and a generalized analytical fluid-dynamics model [Gelderblom *et al.*, J. Fluid Mech. **794**, 676 (2016)]. These findings can be used to optimize the kinetic energy partition and tailor the features of tin targets for nanolithography.

4.1 Introduction

Today, state-of-the-art nanolithography machines employ liquid tin microdroplets as mass-limited targets to generate extreme ultraviolet (EUV) light, which is then used to produce semiconductor devices with unprecedented spatial resolution [6, 34, 119–121]. In this context, the generation of EUV light is based on a two-step process, where a first laser pulse (prepulse) shapes an initially spherical droplet into a thin layer of tin (target) [7]. This target is then illuminated by a second pulse (main pulse) to produce a dense and hot tin plasma, where several of its charge states (Sn^{10+} Sn^{14+}) preferentially emit EUV radiation with a wavelength centered around 13.5 nm [17–19, 69, 122, 123]. A full understanding and control of the (prepulse) laser-induced tin droplet dynamics over different timescales is key to optimize EUV source operation [21, 104, 124–126].

The interaction of a nanosecond laser prepulse with a spherical tin microdroplet can be separated into three main phases: (i) the initial laser-tin interaction and plasma generation and expansion on a nanosecond timescale, followed by (ii) an early deformation of the droplet lasting hundreds of nanoseconds and a subsequent (iii) fluid dynamic response of the system on a microsecond timescale, where surface tension plays a central role in shaping the target morphology. The characteristic times of these stages are illustrated on a logarithmic timeline in Fig. 4.1(a), more details of the timescale separation can be found in Refs. [25, 127, 128]. During the *first stage*, the laser-tin interaction drives the generation of a plasma whose rapid expansion imprints a pressure impulse at the droplet-plasma interface, radially expanding the droplet and propelling it along the laser propagation direction. The initial expansion rate $\dot{R}_0$ and the ballistic propulsion velocity U are on the order of 100 m/s [25, 26, 98, 117, 127, 128]. Any plasma onset effects are short, on the hydrodynamic time scale $\tau_h \sim 0.1$-1 ns [25, 53, 127] — much shorter than the laser pulse length τ_p, so $\tau_h \ll \tau_p$ such that an ablation front is established providing plasma pressure over the full $\tau_p \sim 10$ ns time scale. In the *second stage*, the droplet starts to deform into a circular thin sheet. This early deformation takes place during the inertial time $\tau_i = R_0/\dot{R}_0 \sim 100$ ns, for a droplet radius $R_0 \sim 10$ μm. As deformation progresses towards the *third stage*, a rim forms at the periphery of the sheet, where surface tension causes a deceleration of the sheet's radial expansion rate on the capillary timescale $\tau_c = [\rho D_0^3/(6\sigma)]^{1/2} \sim 10$ μs[†], with the droplet diameter D_0, the liquid density $\rho = 6900$ kg m^{-3} and the surface tension $\sigma = 0.55$ N/m [25, 26,

---

[†]The definition of the capillary time in this chapter is different from that used in Refs. [26] and [117] where $\tau_c = (\rho R_0^3/\sigma)^{1/2}$.

117, 127–130]. The surface tension drives the radial contraction of the sheet and fluid dynamic instabilities both on the sheet [26, 131] and at the rim [130, 132]. The instabilities at the rim, in turn, form ligaments that eventually shed fragments via pinch-off processes [131, 132]. Given the complexity of this dynamic deformation process, controlling the $\dot{R}_0/U$ ratio is crucial to tailor the precise target morphology. In an industrial setting, a specific target size is obtained by expanding at a rate $\dot{R}_0$ over a preset time interval. In this context, the propulsion speed U can be identified as a side-effect from obtaining $\dot{R}_0$, essentially a loss channel of kinetic energy. Therefore, it is highly relevant to elucidate the physics that dictates how much of the deposited laser energy is channeled to radial deformation kinetic energy $E_{k,d}$ and forward propulsion kinetic energy $E_{k,cm}$ of tin targets and enable optimization thereof [128].

To understand the kinetic energy partitioning in the current problem, we can draw upon well-established analogies with droplet impact upon a rigid substrate, where the impact velocity U is identified as the characteristic speed to describe the hydrodynamic response and sets the kinetic energy as the initial condition of the process [129, 133–138]. However, in the classical case of drop impact onto a pillar, the late hydrodynamic response may further depend on the initial expansion rate $\dot{R}_0$ of the droplet, which deviates from U when varying the relative size of the drop with respect to the pillar diameter [129, 139, 140]. In case of droplets irradiated by pulsed lasers (be it vapor-propelled water [127] droplets or plasma-propelled tin droplets [25]), there is no rigid body and instead the impact process is governed by the laser-matter interaction, which requires a more complex description of the mechanisms involved in the impact. The relation between a predefined pressure pulse and the fluid dynamic response of a droplet has been analytically described in Ref. [128]. In that work, the initial velocity field inside a droplet was derived by considering inviscid and incompressible flow after applying an instantaneous pressure impulse at a liquid droplet surface. In Ref. [128], the full hydrodynamic response (early and late stages) is then solely and fully determined by the ratio of kinetic energy initially channeled to deform the droplet and the kinetic energy to propel its center-of-mass. Although this work established a solid link between the partitioning of kinetic energy $E_{k,d}/E_{k,cm}$ in the droplet and a given analytical (and instantaneous) pressure impulse, a detailed description and understanding of the pressure impulse generated by the expanding plasma cloud itself is lacking. Moreover, the validity of the aforementioned assumptions (i.e., instantaneous, inviscid, incompressible) remain to be ascertained for the current, rather extreme case of a laser-impacted tin droplet.

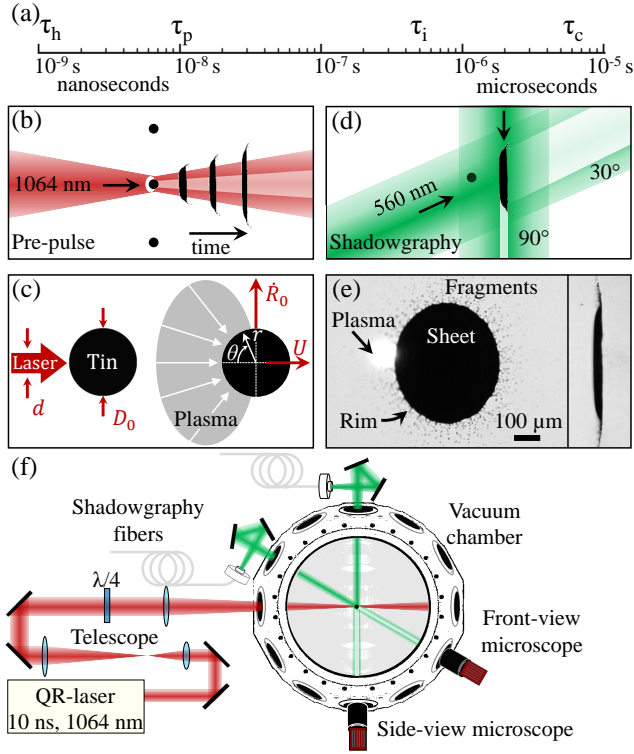In this work, we combine experiments and radiation-hydrodynamic simulations

Figure 4.1: Schematics of laser-tin droplet interaction. (a) Characteristic times during and after the laser-droplet interaction. (b) Schematic of the irradiation geometry (side view). A liquid tin microdroplet is irradiated using a single focused ns-laser beam. The black circles represent the tin droplets and the elongated shadows illustrate the expanding tin target. (c) Schematic of the laser-droplet system with the most relevant parameters, including the laser beam d and droplet D_0 diameters and the propulsion U and radial $\dot{R}_0$ velocities. The cartoon on the right-hand side illustrates the momentum transfer to the droplet mediated by the laser-induced plasma expansion recoil. The cartoon also shows the polar coordinate system (r,θ) with its origin at the droplet center. (d) Schematic representation (top view) of the shadowgraphy illumination at 30° and 90° used to image the deforming droplet target. (e) Experimental front-view (left) and side-view (right) shadowgraphy images of an expanding sheet of tin. (f) Schematic of the top view of the experimental system.

to investigate the ns-laser-induced early-time fluid dynamic response of liquid tin microdroplets. First, we experimentally record the evolution of the liquid tin morphology using stroboscopic shadowgraphy, from which we extract both the propulsion velocity U and expansion velocity $\dot{R}_0$. We systematically investigate the influence of the droplet diameter D_0, beam diameter d and laser energy E on U and $\dot{R}_0$. The

experimental U and $\dot{R}_0$ velocities agree well with those obtained from radiation-hydrodynamic simulations performed with the RALEF-2D code. The simulations further allow us to extract the pressure impulse at the droplet-plasma interface. We identify the width of the pressure impulse as the crucial characteristic length governing the kinetic energy partitioning $E_{k,d}/E_{k,cm} = f(\sigma)$. Thus, we describe the balance of kinetic energy channeled to the deformation or propulsion of the droplet using a single parameter that comprises the effect of all the experimental parameters: d, D_0 and E. Finally, this energy partition is compared with the predictions of a purely fluid dynamic model developed in Ref. [128].

4.2 Experiment

Figure 4.1(b) illustrates the tin droplet irradiation geometry, where a single laser prepulse illuminates a tin micro-droplet. The recoil pressure exerted by the expansion of the laser-produced plasma gives rise to a propulsion and a radially symmetric deformation characterized by the center-of-mass velocity U and the radial velocity $\dot{R}_0$, as shown in Fig. 4.1(c). In the current experiments, these velocities are on the order of 100 m/s. To study the expansion and propulsion dynamics, we use a strobo-scopic shadowgraphy system as depicted in Fig. 4.1(d). This system provides front- and side-view images as a function of the time between the laser prepulse and the shadowgraphy probe pulse. In Fig. 4.1(e) we provide an example of shadowgraphy images and illustrate the main constituents of the expanding tin target.

4.2.1 Experimental setup

In the following, we explain the experimental system illustrated in Fig. 4.1(f); more details can be found in Ref. [141]. A vertical train of spherical liquid tin droplets (260 °C) is dispensed using a piezo-electric-driven droplet generator, which is mounted on a motorized assembly that adjusts the direction of the train. Its repetition rate ranges from 5 kHz to 65 kHz, which allows for accurate control of the droplet diameter D_0 from 55 μm to 25 μm. The droplets have a speed of 11 m/s while they pass through the center of a vacuum vessel (10^{-7} mbar). The droplets are illuminated using a light sheet generated by a He-Ne laser combined with a cylindrical lens. The scattered light is collected by a photo-multiplier tube, down-converted to 10 Hz and used to trigger a Nd:YAG laser and the imaging systems.

For the laser experiments, we use a Nd:YAG laser system (Quanta-Ray, Spectra-Physics) that delivers linearly polarized pulses at a central wavelength of 1064 nm,

with a repetition rate of 10 Hz. The laser has a Gaussian temporal profile with a pulse duration of $\tau_p = 10$ ns (FWHM). From this point forth, we simply refer to the prepulse laser as laser. The laser passes through a quarter-wave plate to attain circular polarization at the droplet surface, which allows us to attain cylindrical symmetry of the laser energy deposition at the surface of the droplets, thus leading to an axisymmetric expansion. We use two telescopes to provide beam diameters of either 1 or 4 cm before passing through our focusing optics. We then focus the laser beam using a lens with a focal distance of 300 mm and a diameter of 7.5 cm. The full width at half maximum (FWHM) of the focused laser beam at the droplet location was adjusted in the range 15–130 μm by carefully modifying the position of the lens. The 1 cm and 4 cm input beam diameters enable us to scan ranges of 40–130 μm and 15–50 μm, respectively. Before the laser-tin interaction experiments, the laser Gaussian spatial distribution was characterized using a beam profiler by recording images of the attenuated laser beam while changing the distance between the lens and the center of the vacuum chamber. These images were used to characterize the beam diameter and the laser energy fraction impinging on the droplet surface.

The laser-induced dynamics of the irradiated droplets were recorded using a stroboscopic shadowgraphy imaging system. This system uses incoherent light pulses at 560 nm with a pulse duration of 5 ns to illuminate the expanding tin target by imaging it onto the chip of a CCD camera using a long-distance microscope (K2 Distamax, Infinity). Two twin shadowgraphy systems are used to record the dynamics at 30° (front view) and 90° (side view) with respect to the laser beam propagation axis. These imaging systems provide a spatial resolution of 5 μm. The time delay between the prepulse laser and the shadowgraphy pulses was set to start at $t = $ -500 ns extending up to 4000 ns.

4.2.2 Experimental results

In the following, we will examine the laser-induced target morphology, propulsion speed U and the initial expansion rate $\dot{R}_0$ of the droplet and their dependence on the variables of E, d and D_0 for a large parameter space. The droplet response is also influenced by the polarization state [142] and the temporal intensity distribution of the laser [118, 143], which we set to be constant here.
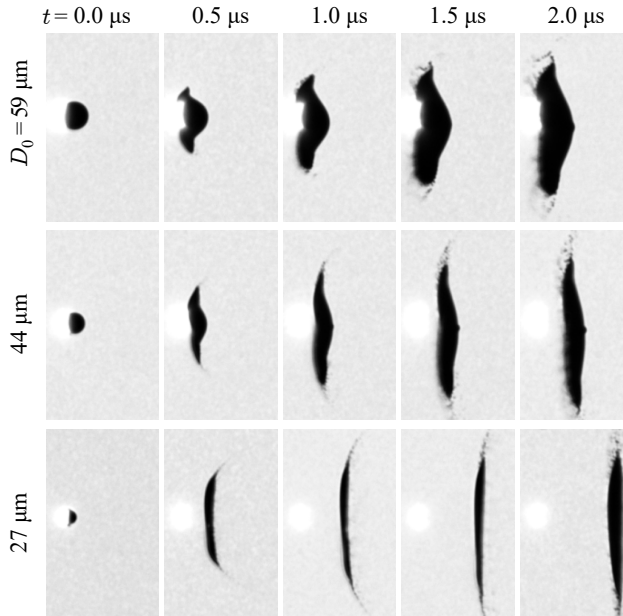
Figure 4.2:   Set of representative side-view shadowgraphy images. Each image illustrates the target morphology considering different droplet diameters (rows) and time delay after laser illumination (columns). Note that the laser beam propagates from left to right in the images and thus impinges on the left side of the droplets. Here, we set $d = 20\,\mu m$ and $E = 0.8\,mJ$. The bright spot in all images corresponds to the laser-induced plasma emission. The images capture an area of 425 µm by 270 µm.

4.2.2.a   Target morphology

In Fig. 4.2, we show a set of representative shadowgraphy images of the expanding tin target at several time delays (columns). These images illustrate a variety of morphologies that are the result of irradiating droplets with three different diameters (D_0 rows), while keeping a constant laser beam diameter and energy ($d = 20\,\mu m$ and $E = 0.8\,mJ$). The ablation of smaller droplets leads to flatter tin morphologies forming an axisymmetric thin sheet (see bottom row with $D_0 = 27\,\mu m$). For larger droplets, morphologies with a smaller radius of curvature are observed. This curved morphology is caused by a non-homogeneous (but cylindrically symmetric) laser energy deposition at the droplet surface, as the beam is much smaller than the droplet and a certain area of the droplet surface remains unaltered. The top row exemplifies this effect, where the beam diameter ($d = 20\,\mu m$) is approximately one third of the droplet diameter $D_0 = 59\,\mu m$. This case shows a partial ablation of the droplet

surface around its pole, which resembles the ablation of a flat liquid pool as it generates a similar crown-shaped splash [144]. In contrast, the bottom row illustrates an experiment where the whole left hemisphere of the droplet is illuminated by the laser and, therefore, is ablated more homogeneously.

In addition to the morphology, the shadowgraphy images in Fig. 4.2 illustrate a change in propulsion speed and expansion rate when varying the droplet size. This becomes evident when comparing the sheet positions at $t = 2\,\mu s$ (rightmost column) between the $D_0 = 59\,\mu m$ and $D_0 = 27\,\mu m$ cases, where a faster propulsion speed for smaller, and thus lighter, droplets is observed. Furthermore, smaller droplets exhibit a faster initial expansion rate, which can be seen by comparing the sheet diameters at $t = 0.5\,\mu s$ for different droplet sizes. Next, we will quantitatively explore the propulsion and expansion rates and their dependence when varying E, d and D_0.

4.2.2.b   Laser-induced propulsion of liquid tin droplets

The acceleration of the droplet to a center-of-mass velocity U takes place in the short timescale of $\tau_p \sim 10\,ns$, after which U remains constant. This velocity can be described by a function of several laser and geometrical parameters $U = f\left(d, D_0, E\right)$ as shown in Refs. [26, 98, 127]. Our current work explores this dependence for a much larger parameter space, in which we explicitly consider the case where the beam size is smaller than the droplet size $d < D_0$ (see full data sets provided in the Appendices). Figure 4.3 presents U as a function of E, D_0, and d as independent variables. The data indicate that the propulsion velocity increases with increasing laser energy in panel (a) and decreasing droplet (b) and beam diameters (c). These observations agree well with our previous study in Ref. [98], where the *energy-on-droplet* E_{od} was identified as the principal parameter determining U (considering a single D_0 value). The E_{od} is defined as the incident laser energy illuminating the droplet surface, i.e., it accounts for the geometrical overlap of the laser beam profile and the spherical droplet surface as

$$E_{od} = E\left(1 - 2^{-D_0^2/d^2}\right). \tag{4.1}$$

A power-law dependence of U with E_{od} has been established by Kurilovich *et al.* [98] as

$$U = K_U E_{od}^{\alpha}, \tag{4.2}$$

with $K_U = K_U'(50\,\mu m/D_0)^{1+2\alpha}$, where K_U' is a proportionality factor that does not depend on D_0 [98]. The exponent α originates from the correlation between the
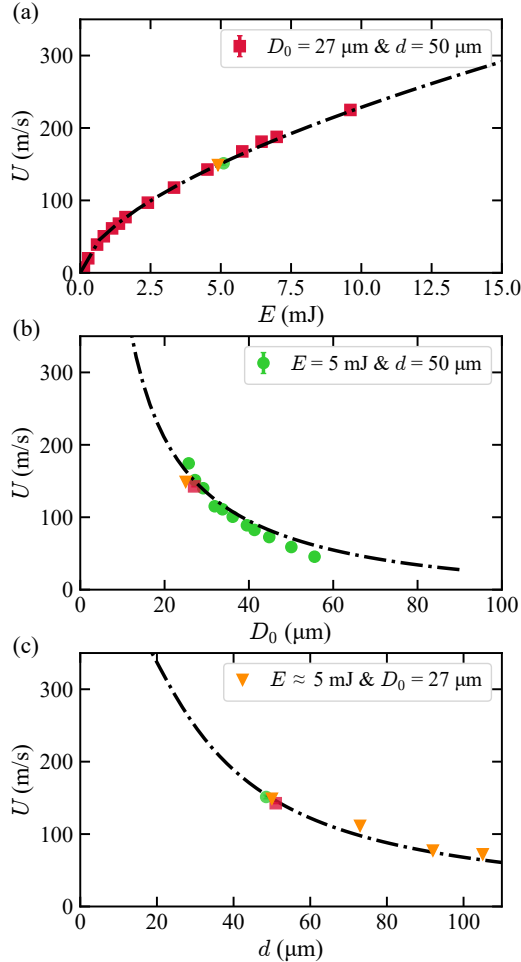
Figure 4.3: Experimental center-of-mass velocity U. Graphs of U as function of (a) the laser energy E, (b) droplet diameter D_0 and (c) beam diameter d. In (a), the droplet and beam diameters were set to $D_0 = 27$ μm and $d = 50$ μm, respectively. In (b), the beam diameter and the energy were set to $d = 50$ μm and $E = 5$ mJ. In (c), the droplet diameter and the energy were set to $D_0 = 27$ μm and $E \approx 5$ mJ. In all graphs the dash-dotted lines are the result of a global fit of Eq. (4.2) to the data. Overlapping symbols are horizontally offset for visibility.

plasma pressure and the laser pulse intensity and was determined to be $\alpha = 0.6$ in Refs. [25, 98]. Naturally, an increase in pulse energy leads to a higher E_{od}, which yields a higher propulsion velocity, as seen in Fig. 4.3(a). On the one hand, a larger droplet size increases the overlap with the incident beam, leading to a larger E_{od} and

to a larger impulse exerted by the plasma pressure. On the other hand, the mass of the droplet and hence the momentum corresponding to a certain propulsion velocity increases following $P \sim D_0^3 U$. As a result, the propulsion velocity is expected to decrease with increasing droplet size, which is consistent with our observations in Fig. 4.3(b). As for the beam size, a tightly focused beam, while keeping a constant $E-D_0$ combination, leads to a higher E_{od}, which therefore results in a larger U as shown in panel (c). Equation (4.2) is then fitted to our data in Fig. 4.3 with (a) E, (b) d and (c) D_0 as independent variables. We perform a global fit to all data in Fig. 4.3 with the power α fixed to 0.6 while leaving K'_U as a free fitting parameter. The fit yields a sole prefactor equal to $K'_U = 41(5)\,\mathrm{m\,s^{-1}\,mJ^{-0.6}}$, which agrees well with a value $K'_U = 36(3)\,\mathrm{m\,s^{-1}\,mJ^{-0.6}}$ obtained in Refs. [25, 98]. The specified uncertainty is dominated by the error in characterizing the beam diameter d at the location of the droplet. Moreover, the global fit shown here is consistent with the fit presented in Fig. 4.8(a) in the Appendices, which also yields $K'_U = 41\,\mathrm{m\,s^{-1}\,mJ^{-0.6}}$. In Fig. 4.8(a), Eq. (4.2) is fit to the combined U, E_{od} data that collapses onto a single curve for seven beam diameters that scale from $17\,\mu\mathrm{m}$ up to $100\,\mu\mathrm{m}$.

Our study validates the applicability of Eq. (4.2) over a wide range of $d-D_0-E$ combinations including the case where the laser focus is smaller than the droplet. For the case of $d < D_0$ we have no grounds to assume that the coefficient K_U is a function of D_0 only, and one should explicitly account for the dependence on d as well. In this case the imparted momentum would scale with d^2, following the intersecting beam-droplet area. However, the precise scaling is influenced by (i) the reduction of the fraction of propelled mass, as a result of employing a beam size that is smaller than the droplet ($d < D_0$), and (ii) plasma expansion from the illuminated droplet area, increasing the intersecting beam-plasma absorption area (see the following discussion in Sec. 4.3). Our results suggest that these effects compensate divergence in this $d < D_0$ case from the momentum scaling $P \sim D_0^2$ found in the $d > D_0$ case [98]. We emphasize here that the propulsion velocity U can be elegantly determined by $U = f(E_{od}, D_0)$ with all data shown to collapse onto a single curve, see Fig. 4.8 in the Appendices. Such an independence of U on the beam size, when E_{od} and D_0 are given, however is not applicable to define the initial expansion rate $\dot{R}_0$, as we discuss in Sec. 4.2.2.c.

4.2.2.c Expansion dynamics of liquid tin droplets

The ns-laser-induced expansion dynamics of liquid tin microdroplets has been studied previously in Refs. [117, 128–131]. As discussed in Sec. 4.1, these works established how the radial trajectory $R(t)$ can be well described on a microsecond
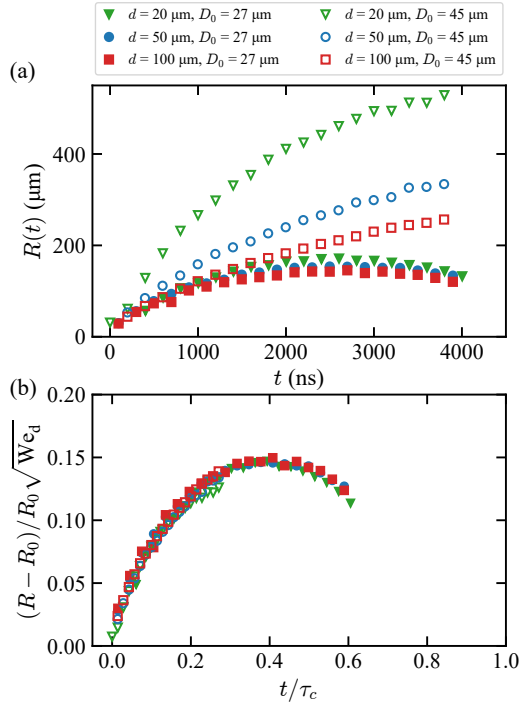
Figure 4.4:   Sheet radius $R(t)$ from experiment as a function of time. (a) These experiments were performed using three beam diameters and two droplet diameters while keeping a constant propulsion velocity of 80 m/s. (b) Dimensionless sheet radius $(R - R_0)/R_0 \sqrt{\mathrm{We_d}}$ as a function of the time relative to the capillary time τ_c. Open and solid markers indicate results for tin droplet diameters of 45 μm ($E_{od} \approx 2.8$ mJ) and 27 μm ($E_{od} \approx 0.3$ mJ), respectively.

timescale by fluid-dynamics models in analogy to a droplet-pillar impact case that considers incompressible flow. After a rapid radial acceleration due to the impulse imparted by the impact, the droplet primarily deforms into a thin sheet delimited by a rim. The radial expansion hence undergoes an initial laser-driven acceleration and a subsequent deceleration due to the surface tension. In this way, the radius of the sheet increases, at an initial expansion rate of $\dot{R}_0$, reaches a maximum radius and then contracts. The maximum sheet size and the expansion trajectory $R(t)$ are determined by the deformation Weber number $\mathrm{We}_d = \rho D_0 \dot{R}_0^2 / \sigma$ with the liquid density $\rho = 6900$ kg m^{-3} and the surface tension $\sigma = 0.55$ N/m [26, 127]. In Fig. 4.4(a), the radius of the sheet $R(t)$ as a function of time is plotted for several combinations E, d and D_0, which all lead to the same propulsion velocity of $U = 80$ m/s. We choose

data sets with the same U in order to discuss the origin of different expansion-to-propulsion ratios. Our data clearly illustrates (i) the initial radial expansion of the sheet and (ii) the effect of the surface tension that causes the gradual decrease of the expansion rate leading to the observation of an apex radius and a subsequent decrease of $R(t)$.

Figure 4.4(b) presents the dimensionless sheet radius $(R - R_0)R_0^{-1}We_d^{-1/2}$ following Villermaux *et al.* [129], using the deformation Weber number We_d [131] as a function of the scaled time t/τ_c. Considering the droplet sizes used in the experiments (27 μm and 45 μm), we obtain capillary times of 6.5 μs and 14 μs[‡], respectively. Figure 4.4(b) shows that all the data collapse onto a single curve upon use of the scaled parameters. Such a collapse is consistent with the findings reported in Refs. [128, 129, 145].

As mentioned above, the initial expansion rate $\dot{R}_0$ has been identified as a crucial variable to characterize the fluid dynamic response that dictates the radial expansion. Therefore, we limit our analysis here to $\dot{R}_0$, which is obtained by a linear fit to the $R(t)$ data up $t = 300$ ns. In analogy to $U(E_{od}, D_0)$ in Eq. (4.2), we first seek an expression of the form $\dot{R}_0 = f(E_{od}, D_0)$. A quantitative study of the response of a droplet to laser impact for various laser parameters, but keeping U constant (see Fig. 4.4 and also the Appendices) shows that unlike the propulsion speed U, there is an additional, explicit dependence of $\dot{R}_0$ on the beam size d and, thus, $\dot{R}_0 = f(E_{od}, D_0)$ is not complete. As predicted in Ref. [128], experiments performed using a tighter focused beam result in a larger $\dot{R}_0$. This effect can be seen in Fig. 4.4(a) by comparing the data obtained by using beam sizes $d^\triangledown = 20$ μm and $d^\square = 45$ μm, where $\dot{R}_0^\triangledown > \dot{R}_0^\square$ for equal U.

The nontrivial dependence of $\dot{R}_0$ on the laser beam size d and its relevance to explain the fluid dynamic response inspired us to numerically investigate the plasma pressure and its spatial profile at the droplet surface. In the next section, we will discuss the precise way in which momentum is transferred at the plasma-droplet interface through the use of radiation-hydrodynamic simulations.

[‡]In the published work [Physical Review Research **4**, 013142 (2022)] that corresponds to this chapter, these two values for the capillary time for $D_0 = 27$ and 45 μm were wrongly written. These values are corrected now in this chapter. We note that in the published work, the capillary time τ_c used in the relevant Fig. 4.4 followed the correct values (i.e., 6.5 μs and 14 μs for $D_0 = 27$ μm and 45 μm, respectively).
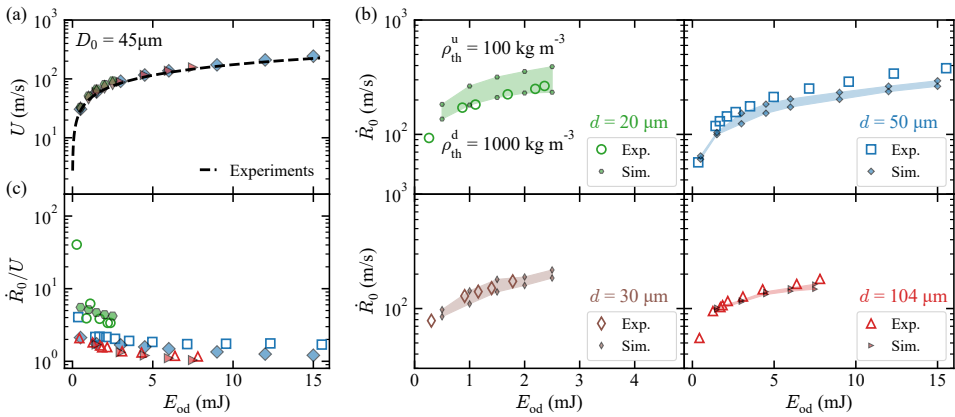
Figure 4.5: Comparison between experiments and simulations. In the $D_0 = 45$ µm case, the filled and empty markers represent the simulation and experimental results, respectively. Graphs of (a) the propulsion velocity, (b) the initial radial velocity and (c) the ratio $\dot{R}_0/U$ as a function of E_{od}. In (a) the dashed line represents the fit of the experimental data presented in Fig. 4.8(b). The shaded areas in panel (b) present the estimated $\dot{R}_0$ ranges using RALEF-2D, where the upper and lower limits correspond to the values calculated using density thresholds of 100 and 1000 kg m^{-3}, respectively.

4.3 Simulation

4.3.1 Code description

We have performed simulations of the laser-droplet interaction and subsequent droplet deformation and expansion using the two-dimensional (2D) radiation-hydrodynamic RALEF (Radiation Arbitrary Lagrange–Eulerian Fluid dynamics) code [146, 147]. The code was originally developed to model high-temperature laser-plasma experiments conducted at GSI Darmstadt [95, 96]. In more recent times, however, the application domain of the code has shifted to the modeling of laser-driven tin plasmas in the context of EUV light sources for nanolithography [18, 51, 53, 97, 98, 148].

The hydrodynamic module of RALEF-2D is based on an upgraded version of the 2D CAVEAT code developed at Los Alamos National Laboratory [100]. The code solves the single-fluid single-temperature hydrodynamic equations on a structured quadrilateral mesh using a second-order Godunov-type scheme, see Ref. [104] for more details. Algorithms for thermal conduction and radiation transport have been implemented using the symmetric semi-implicit method with respect to time discretization [101, 149]. Energy transport via thermal radiation is described by

the quasi-static LTE (local thermodynamic equilibrium) radiation transport equation [53], and its solution is obtained using the method of short characteristics [150]. The angular dependence of the radiation intensity is modelled using the S_n quadrature method with $n = 6$ [151]. In order to obtain a solution of the LTE radiation transfer equation, one must have information on the radiative properties, i.e., the *spectral absorption coefficients* of the plasma. These data were generated with the THERMOS code [40, 41] and are imported into RALEF-2D in tabular format. For a given density-temperature (ρ, T) pair, the THERMOS code solves the system of collisional-radiative level population equations (in steady-state equilibrium) from which the spectral absorption coefficients are obtained. These data are discretized into 28 spectral groups for use in the simulations. The equation-of-state (EOS) of tin was obtained from the Frankfurt EOS (FEOS) package [52] which is based on the original QEOS model [55] and is an extension of the MPQeos code [54]. A very attractive feature of the FEOS model is its ability to model the low-temperature liquid-gas phase coexistence regions, which is enabled through fully-equilibrium calculations with Maxwell's construction in the two-phase region. We note that the code does not take into account the effects of surface tension, whose influence during the early expansion phase is negligible considering that $\tau_i \ll \tau_c$.

We performed two sets of simulations for spherical tin droplets having diameters $D_0 = 27\,\mu$m and $45\,\mu$m. Our simulations were performed in the axisymmetric (z, r) geometry, where the symmetry axis of the tin sheet coincides with the laser propagation direction and passes through the center of the initially spherical droplet. As detailed in Ref. [98], we construct a polar coordinate system with its origin at the initial position of the droplet center. We adopted a detailed mesh structure of 1 mm radius exhibiting 360 zones over the π interval of the polar angle θ (defined with respect to the z axis pointing toward the incoming laser direction, see Fig. 4.1(c) and Ref. [98]). The mesh is progressively refined towards the initial droplet surface such that the thickness of the outermost cell is approximately 10 nm. The initial density of the liquid tin targets was set to $\rho_0 = 6900$ kg m^{-3}. The region outside the droplet was filled with a low-density tin vapour having $\rho = 10^{-7}$ kg m^{-3}. In the simulations, we employed a $\lambda = 1064$ nm laser pulse with a Gaussian temporal profile of $\tau_p = 10$ ns (FWHM). For both droplet diameter cases, simulations were performed with Gaussian laser beams with FWHM diameters $d = 20, 30, 50$ and $100\,\mu$m. The laser beam employed in the simulations was unpolarized. Laser light propagation and absorption in the plasma was treated using a hybrid model accounting for the effects of laser reflection and refraction in the corona of plasma [39]. The simulations were run up to a time $t_f = 300$ ns, where the center-of-mass speed has become insensitive to the choice of t_f. We note here that we do not adjust any parameters

4

within our simulations to reproduce the experimental observations.

4.3.2   Simulation results

4.3.2.a   Numerical validation: droplet propulsion and the expansion speed

In this Section, we will validate our simulations by comparing the propulsion speed U and the radial expansion rate $\dot{R}_0$ from RALEF-2D to the values determined in our experiments. The determination of U from the RALEF-2D simulations is straightforward and follows that outlined in Ref. [98]. This quantity is defined as the velocity of the center-of-mass (comprising all material having a density greater than 1000 kg m^{-3}) 300 ns after the laser pulse is switched on in the simulations. In Fig. 4.5(a) we present the U values as a function of E_{od}. The black dashed line corresponds to a fit of Eq. (4.2) (with $\alpha = 0.6$) to all the obtained experimental data with a droplet size $D_0 = 45$ μm (see Fig. 4.8 in the Appendices). The symbols represent the RALEF-2D predictions for laser beam diameters $d = 20$ (green hexagons), 30 (brown diamonds), 50 (blue squares) and 100 (red triangles) μm, respectively. The simulated data clearly follows the power-law dependence established in the experimental data.

The evaluation of the radial expansion velocity $\dot{R}_0$ from the RALEF-2D simulations is more complicated than that of U, mainly due to the difficulties in defining the liquid density at the boundary of the droplet and therefore $R(t)$ over time. From the simulations we extracted the radius that corresponds to a density of (i) $\rho_{th}^u = 100$ kg m^{-3} and (ii) $\rho_{th}^d = 1000$ kg m^{-3}. We extracted the value of $R(t)$ every 10 ns within the time interval $100 \leq t \leq 300$ ns. We then fit a linear function to the $R(t)$ data, from which $\dot{R}_0$ was obtained.

In Fig. 4.5(b) we plot the experimental observations and RALEF-2D predictions for $\dot{R}_0$ as a function of E_{od}. The upper bound $\dot{R}_0$ simulated data correspond to a $\rho_{th}^u = 100$ kg m^{-3} reference density and the lower bound data points correspond to $\rho_{th}^d = 1000$ kg m^{-3}. It is clear that the largest spread in simulated $\dot{R}_0$ values is attributed to the $d = 20$ μm case, where best agreement with experimental data can be found for the $\rho_{th}^d = 1000$ kg m^{-3} reference density. With increasing beam diameter, this spread is observed to decrease. An interesting behaviour is observed for the $d = 50$ μm case where the experimental data predicts a higher radial expansion velocity than both reference densities. Overall, our simulation results of U and $\dot{R}_0$ are in good to excellent agreement with our experimental findings, as shown in Figs. 4.5(a)-(b). Moreover, the $\dot{R}_0/U$ ratios in panel (c), calculated for several example cases, are also in good agreement with the experiments considering the
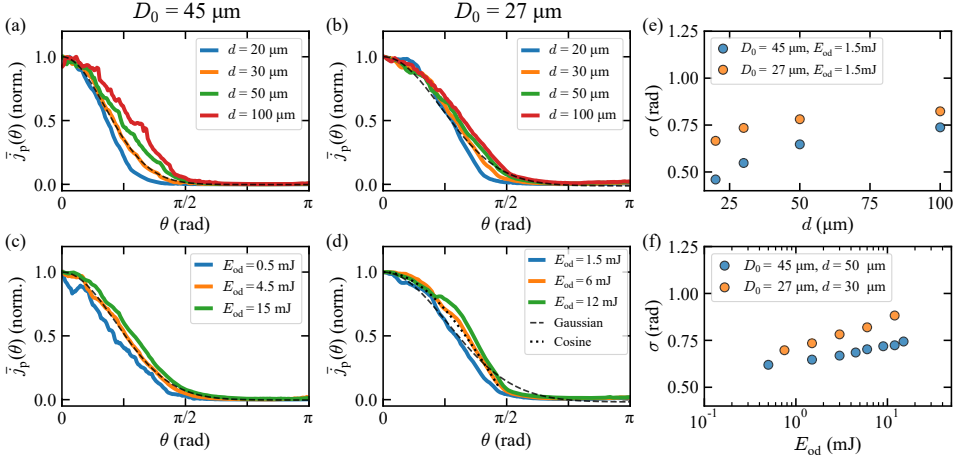
Figure 4.6: Normalized pressure impulse at the surface of a tin droplet extracted from our RALEF-2D simulations. Graphs in panels (a)-(b) present results considering a constant $E_{od} = 1.5$ mJ and four beam sizes while the results in panels (c)-(d) consider constant beam sizes of $d = 50$ μm in (c) and $d = 30$ μm in (d) and three energy-on-droplet values. The simulations were performed for two droplet sizes $D_0 = 27$ and 45 μm. The dashed lines in (a)-(d) illustrate Gaussian fits that enable characterizing the angular size σ. For comparison purposes, the dotted line in (d) shows a fit to a cosine function. Graphs of the angular size σ extracted from the pressure impulse profiles as a function of the d and E_{od}, are shown in (e) and (f), respectively.

reference density $\rho_{th}^d = 1000$ kg m^{-3}. We note that this ratio is larger than one in all instances. This good agreement validates the capability of RALEF-2D in simulating the laser-droplet impact under the current numerical settings, which emulate the experimental conditions in this study. Next, we will present numerical results on the pressure profile.

4.3.2.b   Pressure impulse distributions

As discussed above, the recoil pressure exerted by the expanding plasma imparts forward momentum, P, to the droplet and hence sets the propulsion and expansion behavior. The plasma pressure is related to the forward momentum obtained by the target through

$$P = \int_0^{t_f} \iint_A p_a(t, \theta) \, \mathbf{e}_z \cdot d\mathbf{A} dt, \tag{4.3}$$

where $p_a(t, \theta)$ is the plasma pressure at the droplet surface as a function of time t and polar coordinate θ [128]. We define the local impulse as the time integral of

the local pressure $j_p(\theta) = \int_0^{t_f} p_a(t, \theta)dt$, which is therefore only a function of angle. This integration ends at 95 ns [152]. We note that 90% of the full pressure impulse is imparted within $\sim$ 10 ns from the time at which the peak intensity of the laser pulse is achieved, which is set to 15 ns in this work. The momentum imparted to the droplet thus can be described by the spatial shape of $j_p(\theta)$ [152]. Figures 4.6(a)-(d) illustrate profiles of the normalized pressure impulse $\bar{j}_p(\theta) = j_p(\theta)/j_p(0)$ at the droplet-plasma interface, where $j_p(0)$ corresponds to the pressure impulse at the droplet pole $\theta = 0°$. These profiles are associated with two droplet sizes, namely $D_0 = 45$ and 27 µm. We seek the dependence of $j_p(\theta)$ on the droplet size D_0, beam size d and energy-on-droplet E_{od}.

Figures 4.6(a) and (b) present $j_p(\theta)$ profiles for increasing beam sizes d, with a constant $E_{od} = 1.5$ mJ. The top panels illustrate how tighter laser foci lead to narrower pressure impulse distributions, e.g., see the blue curve in Fig. 4.6(a) with $d = 50$ µm. This observation is expected as the ablation and the consequent plasma generation follow the local intensity of the incident beam [25, 153]. We also observe that the irradiation of larger droplets, considering a constant beam size d, results in narrower impulse distributions, as shown for instance by comparing the blue curves in Figs. 4.6(a) and (b). The bottom panels (c) and (d) present graphs of $j_p(\theta)$ for increasing E_{od} values for a given beam size of $d = 20$ µm. Our data indicate that a higher E_{od} slightly broadens the pressure profile, creating a more uniform distribution. This is due to the faster expansion of the plasma (induced by the increased intensity),which wraps around the droplet, as was also reported in Refs. [98, 118].

We use the data shown in Figs. 4.6(a)-(d) to quantify the angular size of the pressure pulse at the droplet surface. We find that our data can be well described by a Gaussian distribution. This resemblance, along with the function employed in Gelderblom *et al.*, motivated us to fit a Gaussian function to our pressure curves as $j_p(\theta) = j_p(0) \exp(-\theta^2/(2\sigma^2))$ [128]. The fits provide the angular size σ (i.e., standard deviation) of the pressure distributions that we later use to calculate the size of the arc at the droplet surface $\sigma \times D_0$. Following Ref. [128], this angular size sets the late-time target morphology. We illustrate examples of these fits to the orange profiles as dashed lines in Figs. 4.6(a)-(d). Cosine-shaped pressure impulses, observed here for particularly large fluence cases in Fig. 4.6(d), constitute the limiting case in Ref. [128] projecting a flat momentum impulse distribution onto a spherical surface. Figures 4.6(e) and (f) show σ as a function of the beam size d and E_{od}, respectively. The data indicate wider pressure impulse profiles when using both a larger beam size and a higher energy-on-droplet, consistent with aforementioned observation in panels (a)-(d).

4.4   Discussion

Thus far, we have seen how varying the droplet diameter D_0, beam size d, and laser pulse energy E will influence the droplet expansion speed $\dot{R}_0$ and the propulsion speed U. The magnitudes of these speeds, and their ratio, provide valuable insight into the balance of kinetic energy channeled either to the radial deformation, $E_{k,d}$, or to accelerating the center-of-mass of the droplet, $E_{k,cm}$. As mentioned in the Introduction, in Ref. [128], the energy ratio $E_{k,d}/E_{k,cm}$ was identified as the pertinent quantity to describe the late-time evolution of the droplet morphology, e.g., at times $t \sim \tau_c \sim \mu$s. In Refs. [128, 131] direct estimates of the energy partitioning were retrieved from experimentally obtained velocities by using the relation $E_{k,d}/E_{k,cm} \propto \dot{R}_0^2/U^2$ (also see the Appendices). The calculation of the prefactors that accompany this power law relation depends on the assumptions made about the late-time geometry of the target. For instance, a 1/2 prefactor results from considering a thin disk, i.e., a sheet of uniform thickness [128]. A 1/3 prefactor was obtained in Ref. [131] assuming a thickness $h \sim 1/(rt)$, following Ref. [129]. In reality, the sheet thickness changes in a more complex manner with the radial coordinate (over time) [26]. Even with a validated model of the late-time sheet thickness for the current case [26], no reliable predictions for early-time morphology can be extrapolated from it and instead we use RALEF-2D to determine the early-time kinetic energies and their ratios and compare the results with the model from Ref. [128].

   In our simulations, the total kinetic energy of the liquid body is determined by the sum of the discretized kinetic energies corresponding to each cell with a volume δV_i and a velocity vector $\mathbf{u}_i$

$$E_k = \sum_i \frac{1}{2} \rho_i \, \delta V_i |\mathbf{u}_i|^2, \tag{4.4}$$

with the liquid body containing all tin with a density larger than $1000 \, \text{kg m}^{-3}$, i.e., the reference density used for the center-of-mass speed U and expansion velocity $\dot{R}_0$ in Sec. 4.3. Following Ref. [128], we identify the kinetic energy of the center-of-mass as

$$E_{k,cm} = \frac{1}{2} U^2 \left(\sum_i \rho_i \, \delta V_i \right), \tag{4.5}$$

also over a region with $\rho_i > 1000 \, \text{kg m}^{-3}$. Next, the *deformation kinetic energy* is defined as the remaining kinetic energy obtained when subtracting $E_{k,cm}$ from E_k, namely

$$E_{k,d} = E_k - E_{k,cm}. \tag{4.6}$$

The energy partitioning between the deformation and the propulsion of the droplet can thus be quantified by $E_{k,d}/E_{k,cm}$. Although we have shown that U can be described by a function that solely depends on E_{od} and D_0, $\dot{R}_0$ cannot, and is a function of E_{od}, D_0 and d. Therefore, we initially assume here that the energy partition follows $E_{k,d}/E_{k,cm} = f(E_{od}, D_0, d)$. We further seek for a representative parameter that incorporates these three variables to simplify the expression for $E_{k,d}/E_{k,cm}$.

We first investigate the dependence of the energy partition on the beam-to-droplet size ratio d/D_0, the only *a priori* known dimensionless length scale in our system. Figure 4.7(a) shows $E_{k,d}/E_{k,cm}$ as a function of d/D_0, where data for two droplet sizes and multiple E_{od} (color bars) are presented. The graph illustrates that more tightly focused beams, with respect to the droplet size (i.e., smaller d/D_0), lead to a higher kinetic energy channeled to deform the droplet, $E_{k,d}$, instead of propelling it. This observation can be expected from Fig. 4.5(c) where $\dot{R}_0$ increasingly exceeds U when ever-smaller beams are employed. However, the beam-to-droplet size ratio d/D_0 cannot fully account for the effect of the E_{od} on the energy partition as illustrated in Fig. 4.7(a). Furthermore, it fails to capture the change in energy ratio comparing the two droplet sizes for any pulse energy. We thus conclude that d/D_0 is not the pertinent length scale for the problem at hand.

In Fig. 4.6, we describe the pressure impulse $j_p(\theta)$ using a Gaussian function, which provides an angle σ and hence a characteristic arc length σD_0 for each $d - D_0 - E_{od}$ combination. This length defines the actual width of the pressure field at the droplet surface. According to Figs. 4.6(e)-(f), for a given D_0, the width σD_0 increases with the size of the beam d and with the laser energy E_{od}. Therefore, the width of the pressure field σD_0 is a better choice of a characteristic length scale to determine the expansion response of the droplet as it comprises the effect of all experimental parameters.

Next, we describe the energy partition $E_{k,d}/E_{k,cm}$ as a function of σ, i.e., the ratio between the arc length of the pressure field and the droplet diameter $(\sigma D_0)/D_0 = \sigma$. Figure 4.7(b) presents $E_{k,d}/E_{k,cm}$ as a function of σ with the same data shown in panel (a). All the data fall onto a single curve, suggesting that σ is indeed the relevant dimensionless length scale, that simultaneously incorporates the effect of E_{od}, d and D_0 on the energy partition. In this way, we simplify the expression of the kinetic energy partitioning to: $E_{k,d}/E_{k,cm} = f(\sigma)$.

Reference [128] provides an analytical model that can predict the $E_{k,d}/E_{k,cm}$ ratio for any pressure impulse and studies in particular detail the response to a Gaussian-shaped pressure impulse. The close approximation of our $j_p(\theta)$ by a Gaussian function (see Fig. 4.6) hence enables our data to be directly compared to the results obtained from the fluid dynamic model using the very same definition of σ.
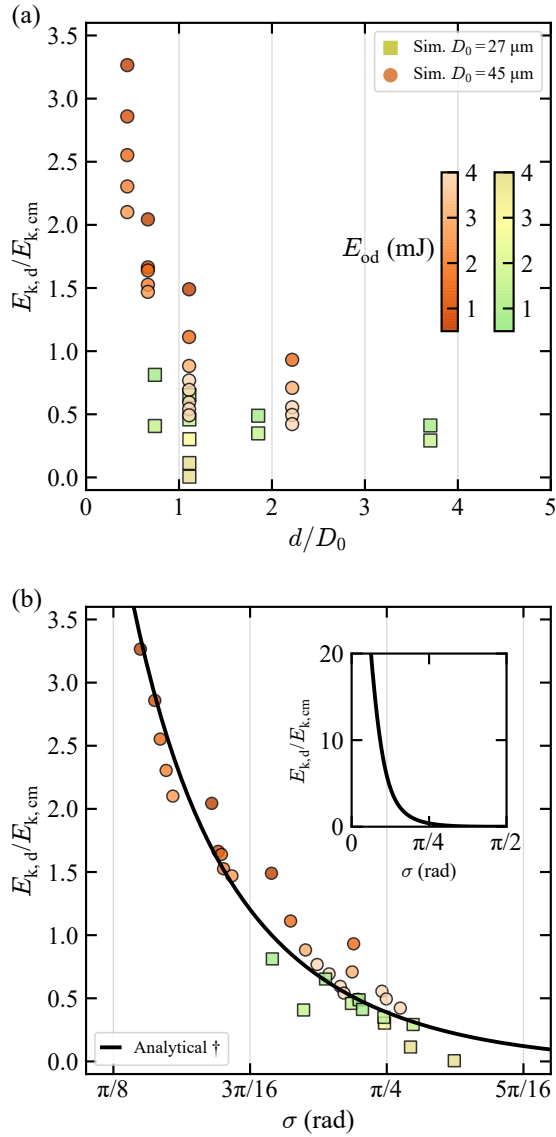
Figure 4.7: Simulated kinetic energy partition $E_{k,d}/E_{k,cm}$ as a function of (a) the size ratio d/D_0 and (b) the pressure impulse width σ. The black solid line † in (b) was calculated following the analytical expression proposed by Gelderblom *et al.* in Ref. [128].

This comparison is presented in Fig. 4.7(b), which shows an excellent agreement between our simulations and the model. We note that the most extreme cases, i.e., those with the largest σ values, correspond to scenarios where the dominant fraction of the initial droplet mass is ablated whereas the model assumes that a negligible mass fraction is ablated (for non-extreme cases this mass loss fraction is at the ~10% level in line with Ref. [98]). At these large values of σ also the largest relative deviations between model and simulations are observed. These deviations should not be interpreted as a breakdown of the model, but instead as the limit of the range of validity of the current comparison. Considering the complexity of our RALEF-2D simulations, which include a plethora of physics aspects, the agreement shown between the simulation and the analytical model [128] is remarkable. This agreement validates the key model [128] assumptions of (i) an instantaneous pressure impulse causing an (ii) inviscid, (iii) incompressible flow. The assumption (i) is valid for the cases in the current work, where the liquid velocity field is established well before significant deformation occurs as $\tau_p \ll \tau_i$. The next model assumption (ii) of inviscid flow is valid as the typical Reynolds number is of order Re $\sim$ 10 000. Finally, assumption (iii) on incompressibility is partially validated in the present study. The fluid dynamic response of a droplet is dominated by incompressible flow when the $\tau_p/\tau_a \gg 1$ (the St number) and $p_a/\rho c_s^2 \ll 1$ (the Ma number) [143, 152]. Here, $\tau_a = R_0/c_s$ is the acoustic time, which accounts for the time that an acoustic wave takes to travel half the droplet diameter at the speed of sound $c_s \sim 2500$ m/s [154]. In our current study, the pulse duration $\tau_p/\tau_a \approx$ 1–2, which was shown in Ref. [143] to be sufficient to assure that the flow is dominated by compressible flow. The plasma pressure p_a differential is indicated by our simulations to be smaller, at $\sim$ 100 kbar, than the base pressure of liquid tin at 430 kbar, thus satisfying the condition $p_a/\rho c_s^2 < 1$ to a sufficient degree.

The level of agreement between our simulations and the analytical theory [128] suggests that approximating $j_p(\theta)$ by the Gaussian function is indeed an appropriate measure to characterize the pressure impulse profile in our context. More importantly, the agreement indicates that the combined effect of laser ablation and the dynamics of the plasma impacting droplet can be captured by a single dimensionless quantity σ that uniquely sets the energy partition, which in turn [128] determines the late-time response of the droplet target. The droplet response to laser impact can be accurately described by the incompressible hydrodynamic response of an initially undeformed droplet to an instant pressure impulse. These findings assist in the robust prediction of final target morphology in industrial sources of EUV light.

4.5 Conclusion

In this chapter, we investigate the early hydrodynamic response of liquid tin microdroplets upon nanosecond laser irradiation. Both experimental and numerical methods were employed to explore and understand the influence of the laser energy E, beam diameter d and droplet diameter D_0 on the laser-induced dynamics of tin droplets. Experimentally, we recorded the expansion and propulsion of tin droplets using stroboscopic microscopy, which aids to determine the propulsion speed U and the initial radial expansion rate $\dot{R}_0$. Our results show that the irradiation of smaller droplets, while keeping constant E and d, leads to flatter morphologies and faster expansion and propulsion velocities, when compared to their larger counterparts. Moreover, we show how the propulsion velocity can be accurately described — for a large set of experiments with different E, d and D_0 combinations — using a function of $U = f\left(D_0, E_{\mathrm{od}}\right)$ that was introduced in Ref. [25] for a single D_0. Our results also reveal a more complex behaviour of the radial expansion rate with an explicit dependence on the beam size $\dot{R}_0 = f\left(D_0, E, d\right)$.

To be able to predict and fully understand the dependence of $\dot{R}_0$ on E, d and D_0 and its balance with U, we employed radiation-hydrodynamic simulations using RALEF-2D. The comparison between the experimental and numerical U and $\dot{R}_0$ results shows good agreement, which supports the validity of RALEF-2D in this context. In order to quantify the kinetic energy partition channeled to deform or propel laser-irradiated tin droplets, we retrieved the spatial distribution of the plasma-driven pressure $\bar{j}_p(\theta)$ at the droplet-plasma interface from our simulation. We found that $\bar{j}_p(\theta)$ profiles can be well approximated by a Gaussian function, from which we identify a dimensionless length scale σ to characterize the width of the pressure field.

The unique combination of experiments and simulations used here reveals that σ can be used as the sole relevant parameter to extract the kinetic energy partition $E_{\mathrm{k,d}}/E_{\mathrm{k,cm}}$ that further determines the target morphology on a microsecond timescale. Our description of the energy partition $E_{\mathrm{k,d}}/E_{\mathrm{k,cm}} = f(\sigma)$ using radiation-hydrodynamic modelling is in excellent correspondence with the generalized fluid-dynamics model of instantaneous pressure-driven droplet dynamics proposed by Gelderblom *et al.* [128]. These findings support the separation of characteristic timescales, reconciling the generation of the laser-driven pressure impulse (tens of nanoseconds) and the early hydrodynamic deformation during the inertial time τ_i (hundreds of nanoseconds). Following the conclusions from the here validated theoretical work [128], an optimized scheme for deforming a droplet without losing energy to propulsion is to employ the tightest possible laser focus. Naturally, any

gains from such a scheme need to be balanced against increases in sensitivity to laser-to-droplet alignment as is elucidated in, e.g., Refs. [155, 156]. Furthermore, the final morphology, which is uniquely set by the choice of σ [128], may impact the obtainable conversion efficiency of drive laser light into in-band EUV photons. Our results thus contribute to further the development of laser-driven plasma sources for EUV nanolithography by aiding to accurately attain the desirable features and morphology of tin targets.

Acknowledgements

Appendix I: Scaling of U and $\dot{R}_0$ with laser energy on droplet

Figure 4.8 illustrates several panels with graphs of experimental U, $\dot{R}_0$ and $\dot{R}_0/U$ data as a function of the E_{od} for two different droplet diameters, namely $D_0 = 27\,\mu\mathrm{m}$ (top panels) and $45\,\mu\mathrm{m}$ (bottom panels). In Figs. 4.8(a) and (b), we present a large set of experimental $U - E_{\mathrm{od}}$ curves for several beam diameters and two different droplet diameters. We find that the experimental data collapse onto a single $U - E_{\mathrm{od}}$ curve for a given droplet size. The black dashed lines illustrates fits to Eq. (4.2), which shows good agreement with the experimental observations when considering $\alpha = 0.6$ and $K'_U = 41\ \mathrm{m\,s^{-1}\,(mJ)^{-0.6}}$. In Fig. 4.8(c) and (d), we present the radial velocity $\dot{R}_0$ as a function of the E_{od}. As a reference, we also plot the fits obtained in panels (a) and (b) to illustrate that the radial velocity is in most cases larger than the propulsion velocity. We also observe that the $\dot{R}_0 - E_{\mathrm{od}}$ curves do not overlap for the whole E_{od} range. Considering a constant D_0 and E_{od}, the laser-induced radial
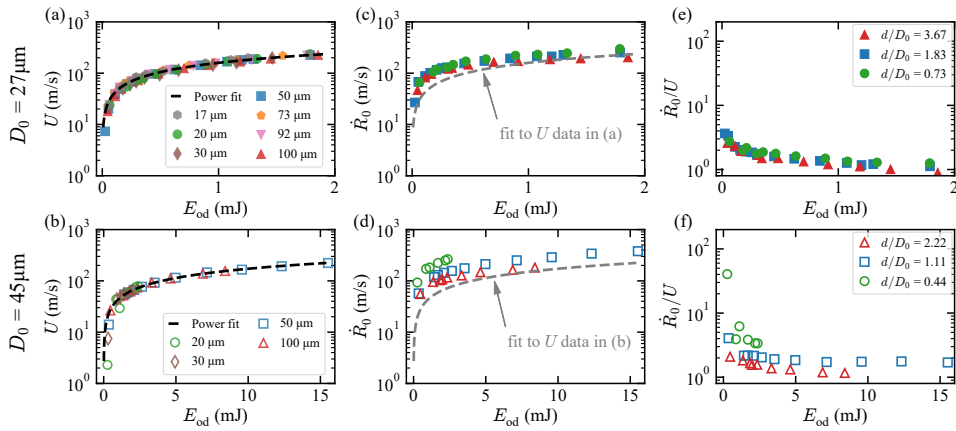
Figure 4.8: Experimental $\dot{R}_0$ and U for a large variety of $d - D_0 - E_{od}$ combinations. Graphs of the experimental propulsion velocity U, (a) and (b), and the radial velocity $\dot{R}_0$, (c) and (d), as a function of the energy-on-droplet E_{od}. The graphs on the top and bottom rows present the results that correspond to experiments carried out using two droplet diameters, namely $D_0 = 27$ μm (filled markers) and 45 μm (empty markers), respectively. Different colors represent the data acquired using different beam diameters, ranging from 17 μm up to 100 μm. The dashed lines are fits to the experimental data in (a) and (b) using Eq. (4.2). (e)-(f) Ratio between the radial velocity and propulsion velocity as a function of the energy-on-droplet. Different colors represent data for several d/D_0 ratios as shown in the legend, which are consistent with the colors assigned to the beam diameters.
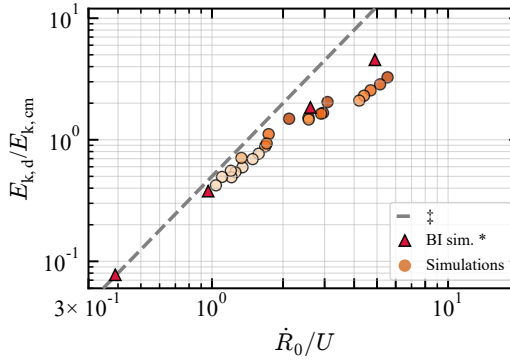
Figure 4.9: Simulated kinetic energy partition $E_{k,d}/E_{k,cm}$ as a function of the velocity ratio $\dot{R}_0/U$. The simulation data shown here as orange circles corresponds to that of Fig. 4.7. The dashed line ‡ were calculated using Eq. (4.7), as proposed by Gelderblom *et al.* in Ref. [128]. The red triangles are the boundary integral (BI) simulations extracted also from Ref. [128].

velocity is larger when using tightly focused beam than a loosely focused beam, see for instance the data markers near $E_{od} = 2\,\mathrm{mJ}$ in panels (c) and (d). We also note here that the differences in $\dot{R}_0$ are more pronounced for the $D_0 = 45\,\mu\mathrm{m}$ case. These observations confirm that the expansion velocity depends not only on D_0 and E_{od}, like U, but also depends on the beam size d, as $\dot{R}_0 = f(D_0, d, E_{od})$, see Sec. 4.3.2.a. Consequently, overall the $\dot{R}_0/U$ ratios are larger for a larger droplet size as shown in panels (e) and (f).

Appendix II: Kinetic energy partition versus velocity ratio

Figure 4.9 presents the energy partition $E_{k,d}/E_{k,cm}$ obtained by RALEF-2D as a function of the velocity ratio $\dot{R}_0/U$. By assuming that the droplet ultimately deforms into a sheet with an uniform thickness, i.e., the velocity field of the liquid in the sheet linearly follows $u \sim r\dot{R}/R(t)$, Gelderblom *et al.* [128] elucidates an instantaneous energy partition for a well-deformed sheet as $E_{k,d}/E_{k,cm}(t) = \dot{R}(t)^2/(2U^2)$. Extrapolating this equation to the onset of the impact at $t = 0$ gives

$$\frac{E_{k,d}}{E_{k,cm}} = \frac{\dot{R}_0^2}{2U^2}. \tag{4.7}$$

Equation (4.7) is plotted as a dashed line in Fig. 4.9. It is shown that with a larger $\dot{R}_0/U$, Eq. (4.7) increasingly overestimates the energy partition from our simulation. This discrepancy might in part be due to a more curved sheet shape when employing a tighter laser beam (see Fig. 4.2 and the discussion in Sec. 4.2.1), leading to a larger deviation of the target morphology from the assumption of a uniform sheet. We also plot the results of boundary integral (BI) simulations extracted from Ref. [128] (red triangles).

4

5

Simulations of plasmas driven by laser wavelengths in the 1.064 – 10.6 μm range as future extreme ultraviolet light sources

Diko J. Hemminga, Oscar O. Versolato, and John Sheil

We characterize the properties of extreme ultraviolet (EUV) light source plasmas driven by laser wavelengths in the $\lambda_{\mathrm{laser}} = 1.064 - 10.6$ μm range and laser intensities of $I_{\mathrm{laser}} = 0.5 - 5 \times 10^{11}$ W cm^{-2} for $\lambda_{\mathrm{laser}} = 1.064$ μm. Detailed numerical simulations of laser-irradiated spherical tin microdroplet targets reveal a strong laser-wavelength dependence on laser absorptivity and the conversion efficiency of generating EUV radiation. For $\lambda_{\mathrm{laser}} = 1.064$ μm irradiation, the increase in in-band radiation with increasing laser intensity is offset by only a minor reduction in conversion efficiency. Radiative losses are found to dominate the power balance for all laser wavelengths and intensities, and a clear shift from kinetic to in-band radiative losses with increasing laser wavelength is identified. Yet, with increasing laser intensity, such a shift is absent. We find that the existence of a maximum conversion efficiency, near $\lambda_{\mathrm{laser}} = 4$ μm, originates from the interplay between the optical

---

[*] Diko Hemminga contributed to this chapter as part of his thesis regarding formal analysis, investigation through performing simulations, visualization, and both writing of the first draft and writing, review and editing of the final draft.

depths of the laser light and the in-band EUV photons for this specific droplet-target geometry.

5.1 Introduction

Extreme ultraviolet lithography (EUVL) is driving mass production of today's most advanced integrated circuits (ICs) [6, 157]. Crucial to the success of this technology has been the development of a sufficiently powerful, stable and "clean" source of EUV radiation [7] concentrated in a narrow 13.5 nm ± 1% region where molybdenum/silicon multilayer mirrors exhibit high reflectance (the so-called "in-band" region) [13, 14]. This radiation is most efficiently generated in a laser-produced plasma (LPP) formed when high-intensity CO_2 laser light (laser wavelength λ_{laser} = 10.6 μm) is focused onto pre-shaped tin microdroplet targets [21, 25, 34, 70, 116, 158, 159]. This plasma contains large populations of $Sn^{11+} - Sn^{15+}$ ions which generate intense, narrowband EUV radiation through bound-bound atomic transitions [15–18, 64, 69, 160].

Nowadays, industrial EUV sources generate a remarkable 250 W of in-band EUV power [161]. Efforts to increase source powers beyond 600 W are now underway to facilitate increased wafer throughput [162]. While CO_2 laser-driven plasmas are the backbone of current EUV sources for high-volume manufacturing [7, 163], rapid developments [27] in solid-state lasers (which typically operate in the near- to mid-infrared wavelength range) make them a viable alternative [121, 148, 164] in the future due to their high efficiencies in converting electrical power to laser light and their potential for scaling to high average powers [27, 165]. These developments have sparked significant interest in the study of short-wavelength laser-driven plasmas for nanolithography [121, 148, 164].

Two crucial topics to be addressed in such studies are the impact of (i) laser wavelength λ_{laser} and (ii) laser intensity I_{laser} on the radiative and kinetic properties of the plasma. The kinetic properties are especially important in the context of debris generation [20, 104] which may limit the lifetime of optical components. The laser wavelength sets the critical electron density (the density at which the plasma becomes opaque to incident laser radiation) according to $n_{e,cr} \propto \lambda_{laser}^{-2}$. This determines the densities for which EUV radiation is generated and must propagate through. High plasma densities or long path lengths generate large optical depths which redistribute in-band energy into other channels, e.g., via spectral broadening [85]. While this effect can be negated by moving to long laser wavelengths, [166], the presence of steep electron density gradients in the plasma can lead to significant laser reflection from the critical surface and a loss of input laser energy [51, 53]. Efficiency at different laser wavelengths is therefore determined by a trade-off in numerous underlying physical processes. The goal of the present work is to quantify this trade-off for laser wavelengths lying in the largely unexplored region between

5

$\lambda_{\text{laser}} = 1.064\,\mu\text{m}$ (Nd:YAG laser) and $10.6\,\mu\text{m}$, although the existence of an optimum laser wavelength has been suggested previously in the EUV source community [167, 168]. Furthermore, we aim to quantify the effect of a second trade-off between absolute power output and the efficiency of generating in-band radiation during illumination by a range of laser intensities.

In this article, we present a comprehensive characterization of the properties of laser-produced EUV source plasmas. The parameter space encompasses (i) laser wavelengths in the $1.064 \leq \lambda_{\text{laser}} \leq 10.6\,\mu\text{m}$ range coupled with an optimum intensity scaling $I_{\text{laser}} \propto \lambda_{\text{laser}}^{-1}$ and (ii) laser intensities in the $0.5 \times 10^{11} \leq I_{\text{laser}} \leq 5 \times 10^{11}\,\text{W cm}^{-2}$ range for $\lambda_{\text{laser}} = 1.064\,\mu\text{m}$. We identify a strong laser-wavelength dependence on laser absorptivity and EUV generation efficiency, and, moreover, report on the early-time establishment of steady-state plasma flows. The partitioning of laser power into plasma components (kinetic, internal and radiated power) is quantified. In our case study, we delve into the factors underlying a maximum in the conversion efficiency (ratio of in-band power radiated into the laser-illuminated half-sphere to laser power) for $\lambda_{\text{laser}} \approx 4\,\mu\text{m}$ laser irradiation, a promising wavelength region indicated previously [167]. It should be emphasized that this is *not* a global optimum; higher conversion efficiencies may be achieved at longer wavelengths by optimizing laser absorption by intricate target preparation [161], which is not discussed in the presented case study. The partitioning of laser power into the plasma components is also quantified as a function of the laser intensity, where only weak dependencies are found for the kinetic and radiated power. Moreover, we report on the spatial profiles of various plasma parameters (temperatures, electron densities, etc.) while the plasma exhibits steady-state flow. Finally, we observe an increase in in-band radiative power with increasing laser intensity at only a small cost to the overall efficiency.

5.2 Numerical simulations

We have performed numerical simulations of laser-produced tin plasmas using the two-dimensional radiation-hydrodynamics code RALEF-2D [95, 146, 147]. It has proven to be a powerful modeling capability for EUV source plasmas, providing useful insights on various topics such as tin droplet fragmentation [97], droplet propulsion and deformation [98, 116], plasma properties [18, 51] and late-time plasma expansion [104]. In the following, we provide details of the code and the simulation parameters used in this study.
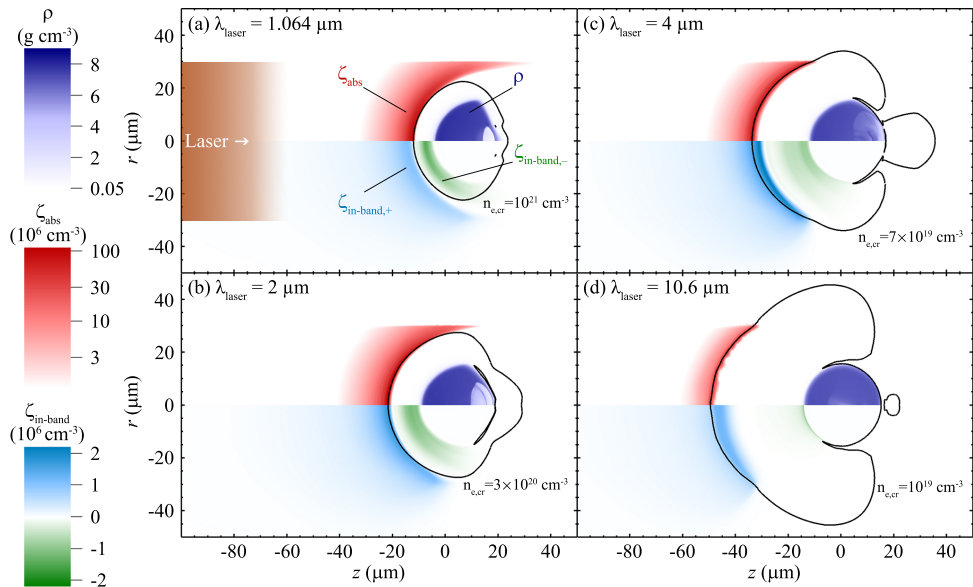
Figure 5.1: The instantaneous (at $t = 18\,\mathrm{ns}$) volume-specific laser deposition rate [39] ζ_{abs} (red) and in-band radiative power $\zeta_{\text{in-band}}$ (light blue – green) normalized by the input laser power for $\lambda_{laser} =$ (a) 1.064, (b) 2, (c) 4 and (d) 10.6 µm. The critical electron density (black contour) and fluid density ρ (dark blue) are indicated.

5.2.1 Code description

RALEF-2D solves the equations of single-fluid, single-temperature hydrodynamics including the processes of radiation transfer and thermal conduction. The hydrodynamic component of RALEF-2D is based on an upgraded version of the 2D CAVEAT code [100], where the hydrodynamic equations are solved on a structured quadrilateral mesh using a second-order Godunov-type scheme. Radiation transfer, which is implemented using a symmetric semi-implicit method with respect to time discretization [101, 149], is modelled using the quasistatic, local thermodynamic equilibrium (LTE) radiation transport equation [51]. As in our previous work [104, 116], the angular dependence of the radiation intensity is modelled using the S_n quadrature method with $n = 6$. The spectral absorption coefficients required to solve this equation are derived from steady-state collisional-radiative modeling using the THERMOS code [40, 169].

The equation-of-state of tin was constructed using the Frankfurt equation-of-state (FEOS) model [52, 54, 55], which can model both low-temperature liquid-gas phase coexistence regions and high-temperature plasma states [51]. Laser light absorption and reflection are treated using a hybrid model combining a geometrical-optics ray-tracing approach in low-density plasma regions and a wave-optics approach in regions near and beyond the critical electron density [39]. Laser absorption coefficients are derived from the complex dielectric permittivity of the plasma as per the Drude model [32].

5.2.2 Simulation parameters

The simulated cases consider laser irradiation of 30-μm-diameter liquid tin droplets, close to the industry standard, with spatially constant laser fluences of 60 μm in width. The laser pulses are temporally trapezoidal shaped with pulse lengths of 20 ns (rise and fall times of 0.2 ns). These experimental parameters are prototypical for recent simulation and experimental works alike (see, e.g., Refs. [25, 38, 51, 53, 66, 81, 85, 90, 148, 170–172]). The laser wavelengths considered in the first part of this work are $\lambda_{\text{laser}} = 1.064, 2, 3, 4, 5, 7$, and 10.6 μm. This encompasses two distinct regimes of laser absorption, where absorption occurs primarily in the (i) underdense corona (for small λ_{laser}) or (ii) a narrow region near the critical surface (for long λ_{laser}) [53]. The laser intensity is scaled according to $I_{\text{laser}} = (1.4 \times 10^{11})/\lambda_{\text{laser}} \, \text{W cm}^{-2}$, an experimentally-motivated scaling which yields high conversion efficiencies for the laser wavelengths considered in this study [66, 86, 148]. We note the close similarity between this scaling and the optimum

laser intensity $I_{\text{laser}} \propto \lambda_{\text{laser}}^{-1.2}$ proposed by Nishihara *et al.* [173]. In the second part of this study, we keep the laser wavelength fixed at $\lambda_{\text{laser}} = 1.064\,\mu\text{m}$ and vary the laser intensity in the range $I_{\text{laser}} = 0.5 - 5 \times 10^{11}\,\text{W}\,\text{cm}^{-2}$ to probe its effect on the radiative and kinetic properties of the plasmas.

5.3 Wavelength-dependent plasma dynamics

In Fig. 5.1, we provide a still of the plasma formation induced by the four laser wavelengths $\lambda_{\text{laser}} = 1.064, 2, 4, 10.6\,\mu\text{m}$ at the time $t = 18\,\text{ns}$ after the laser pulse is switched on. The absorbed laser power per unit volume normalized by the input laser power, denoted ζ_{abs}, is shown in the upper halves of the panels. We find that with increasing λ_{laser}, the laser absorption zone moves further away from the droplet (dark blue region) due to the inverse square dependence of $n_{\text{e,cr}}$ (black contours) on λ_{laser}, and that the electron density closely follows the profile $n_e \propto d^{-2}$ (where $d = \sqrt{r^2 + z^2}$) associated with steady spherical flow [51]. Moreover, the spatial extent over which the laser light is absorbed reduces with increasing λ_{laser}, a direct result of the aforementioned transitioning between the two distinct regimes of laser absorption. The steep electron density gradient precludes efficient absorption of long-wavelength laser light. In panel (d), we see that CO_2 laser absorption is restricted to a narrow region in front of the critical surface. Adopting the Kramers cross section for inverse bremsstrahlung and assuming a (i) constant-temperature laser absorption zone and a (ii) $n_e \propto d^{-2}$ profile, the optical depth of laser light τ_{laser} can be written [51]

$$\tau_{\text{laser}} \approx 4 \times 10^{-3} \frac{Z \ln(\Lambda)}{T^{3/2} \lambda_{\text{laser}}^2} \frac{R_{mc}}{a_{uv}^3} \tag{5.1}$$

where Z, $\ln(\Lambda)$, T, R_{mc} and a_{uv} are the charge state, Coulomb logarithm, temperature (in hundreds of eV), radius of the critical surface and a dimensionless parameter determining the position of laser absorption. Inferring appropriate values from our simulations, we estimate $\tau_{1.064\mu\text{m}} \sim 10$ and $\tau_{10.6\mu\text{m}} \sim 1$ for the present illumination geometry.

   In the bottom halves of Fig. 5.1, we show the net in-band radiated power per unit volume normalized by the input laser power, denoted $\zeta_{\text{in-band}}$ and labeled $+$ for net emission and $-$ for net absorption. This provides a local measure of the efficiency of converting laser light to in-band radiation. Of the four cases shown, the $4\,\mu\text{m}$-driven plasma exhibits the highest $\zeta_{\text{in-band},+}$ due to an optimum combination of intermediate laser optical depth and intermediate optical depth of EUV photons
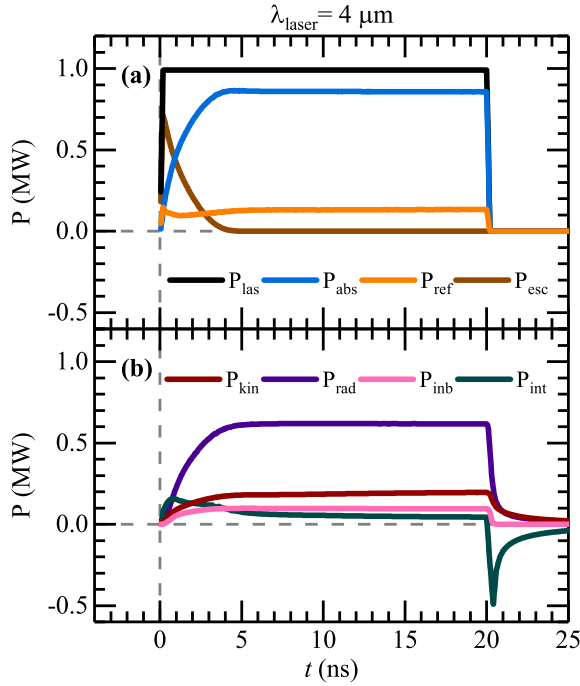
Figure 5.2:   Time-dependent partitioning of laser power into (a) laser- and (b) plasma-based components for $\lambda_{laser} = 4\,\mu m$ irradiation of a 30-μm-diameter tin droplet.

(see discussion below). We see that with increasing λ_{laser}, the region of net in-band emission $\zeta_{in\text{-}band,+}$ (light blue regions) moves from regions with $n_e < n_{e,cr}$ to regions with $n_e > n_{e,cr}$. Furthermore, the regions of net absorption of in-band radiation (dark green regions) are located close to the droplet (a region with high density and low temperature). As discussed by Sunahara *et al.* [37], the long mean free paths associated with such radiation can heat the high-density region and enhance the mass ablation rate [174, 175].

5.3.1   Establishment of steady-state plasma flow

The instantaneous partitioning of laser power during $\lambda_{laser} = 4\,\mu m$ illumination is shown in Fig. 5.2. In Fig. 5.2(a), we show the input P_{las} (black), absorbed P_{abs} (blue), reflected P_{ref} (orange) and "escaped" P_{esc} (brown) laser power components. The escaped component represents laser radiation that initially misses the target, a
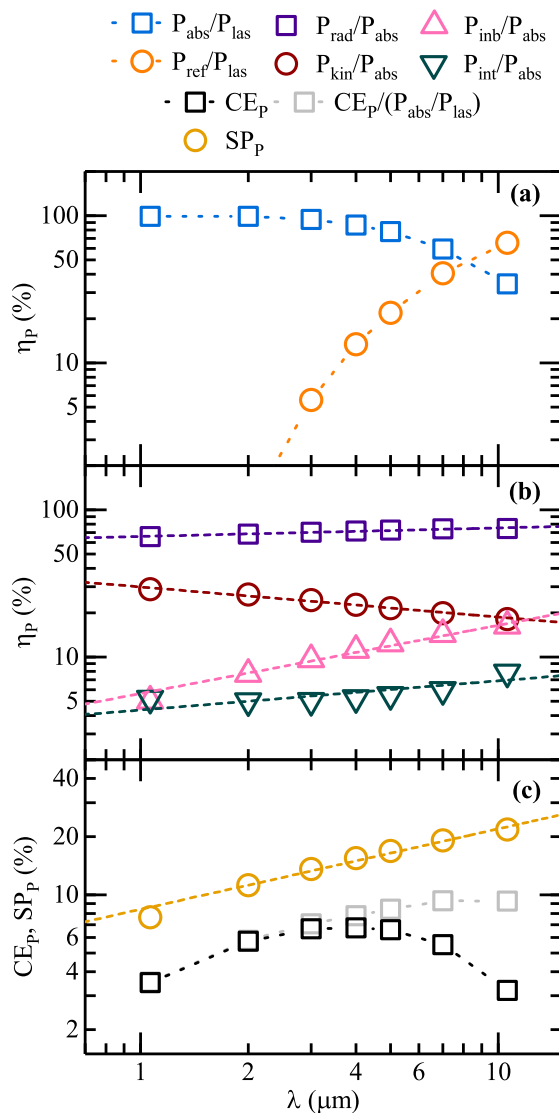
Figure 5.3: The instantaneous (at $t = 18$ ns) partitioning of (a) laser-based components (normalized by P_{las}) (b) plasma-based components (normalized by P_{abs}) and (c) spectral purity SP_P (yellow circles), conversion efficiency CE_P (black squares) and $CE_P/(P_{abs}/P_{las})$ (gray squares) as a function of laser wavelength. The dashed curves represent power-law fits to the data.

5

quantity which decreases rapidly as the plasma expands and starts absorbing incident laser radiation. After 5 ns, a "steady-state" plasma flow regime is established whereafter P_{abs} and P_{ref} attain near-constant values. This behaviour is evident in the plasma-based components P_{kin} (kinetic power, red), P_{rad} (total radiated power, purple), P_{inb} (in-band power, pink) and P_{int} (internal power — derived from the specific Helmholtz free energy [52], green) shown in Fig. 5.2(b). It is well-known that plasmas containing high-Z ions exhibit large radiative losses [42], and our simulations indicate that approximately 70% of the absorbed laser power is channeled into radiation. Moreover, we find that nearly 16% of this radiation is concentrated in the in-band region, a surprisingly large fraction given the narrowness (0.27 nm) of this wavelength region.

5.3.2   Wavelength-dependent power partitioning

Next, we quantify power partitioning as a function of laser wavelength. This enables a comprehensive characterization of the EUV plasma source conditions, where high laser absorptivities coupled with large in-band radiative losses and minimal kinetic losses are most desired. In Fig. 5.3(a), we present the ratios P_{abs}/P_{las} (blue) and P_{ref}/P_{las} (orange) as a function of laser wavelength at steady-state conditions. We note the significant increase in laser reflectivity comparing $\lambda_{laser} = 1.064$ and 10.6 μm cases, which is due to the significant reduction of τ_{laser} with increasing λ_{laser} specific to the current target geometry.

The internal, radiated and kinetic components exhibit their own unique dependencies on laser wavelength. In Fig. 5.3(b), we show the ratios P_{rad}/P_{abs} (purple squares), P_{kin}/P_{abs} (red circles), P_{inb}/P_{abs} (pink triangles), and P_{int}/P_{abs} (green inverted triangles). The dashed curves represent power-law fits to the data. The origin of these power laws is not exactly known, and they most likely originate from a complex interplay of radiation transport, laser absorption and plasma expansion effects. With increasing λ_{laser} (and therefore decreasing plasma density), the optical depth of EUV photons reduces from $\tau_{EUV} \approx 6$ (Nd:YAG-driven plasma) through $\tau_{EUV} \approx 2$ (4-μm-driven plasma) to $\tau_{EUV} \approx 0.5$ (CO_2-driven plasma) [51, 85]. This limits the degree of spectral broadening and redistribution of in-band energy into other channels, which explains the observed increase of P_{inb}/P_{abs} with increasing λ_{laser} and the behaviour of the spectral purity $SP_P = P_{inb}/P_{rad}$ (defined in the full 4π) presented in Fig. 5.3(c). The influence of optical depth on spectral purity and conversion efficiency is further discussed in the work of Schupp *et al.* [85, 148]. As the relative fraction of radiative losses increases with increasing λ_{laser}, the balance dictates a corresponding decrease of kinetic losses.

The efficiency of producing in-band EUV radiation as a function of laser wavelength is shown in Fig. 5.3(c). The conversion efficiency CE_P (black squares) exhibits a concave dependence on λ_{laser} with a maximum at $\lambda_{laser} = 4\,\mu m$. This maximum arises from the rather unique combination of the values of laser optical depth and optical depth of EUV photons. In essence, the plasma conditions are in a "sweet spot" intermediate to the extreme cases of high laser absorptivity/low spectral efficiency ($\lambda_{laser} = 1.064\,\mu m$) and low absorptivity/high spectral efficiency ($\lambda_{laser} = 10.6\,\mu m$). This explains the simulation results of Langer *et al.*, who identified an optimum for $\lambda_{laser} = 4.5\,\mu m$ irradiation of a one-dimensional tin vapor target [167], with which our result is in agreement. It is worthwhile noting that the maximum is located on a rather flat part of the curve between 3 and 5 μm, and that the CE_P increase from 1.064 μm to 2 μm is rather substantial, in line with experimental observations [86].

The strong dependence of conversion efficiency on laser absorptivity for $\lambda_{laser} > 4\,\mu m$ substantiates the opportunity to improve CE_P for long laser wavelengths. In Fig. 5.3(c), we plot the quantity $CE_P/(P_{abs}/P_{las})$ (grey squares), which represents the conversion efficiency if the absorption fraction would be unity for all laser wavelengths. This quantity increases monotonically with increasing λ_{laser}, while reaching a plateau between $\lambda_{laser} = 7$ and $10.6\,\mu m$.

In order to increase laser absorptivity for long λ_{laser}, one could pre-irradiate the target to convert it into a rarefied, spatially extended medium. This would decrease the plasma density gradient and subsequently increase the laser optical depth and, thus, its absorption in the plasma. Such target pre-shaping has been successfully applied in industrial applications, enabling high conversion efficiencies from CO_2 laser-irradiated tin targets [7]. That said, target shaping remains unexplored in the intermediate wavelength region considered in this work, and this may lead to substantial increases in CE_P.

5.4 Intensity-dependent plasma dynamics

As an extension to the characterization described above, we investigate the effects of laser intensity I_{laser} on the radiative and kinetic properties of a plasma driven by $\lambda_{laser} = 1.064\,\mu m$. In a similar vein to Fig. 5.1, we show in Fig. 5.4 the tin mass density ρ, critical electron density contour $n_{e,cr}$, ζ_{abs} (absorbed laser power per unit volume normalized by input laser power) and $\zeta_{in\text{-}band}$ (in-band radiated power per unit volume normalized by input laser power) for four laser intensities $I_{laser} = \{0.5, 1.4, 2, 5\} \times 10^{11}\,W\,cm^{-2}$ at $t = 18$ ns. With increasing laser intensity,
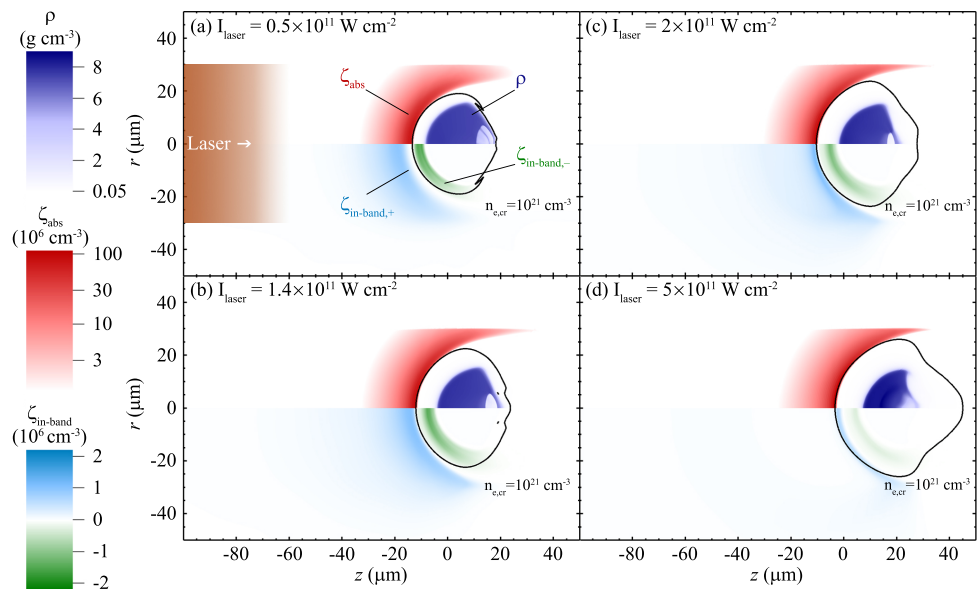
Figure 5.4: The instantaneous (at $t = 18$ ns) volume-specific laser deposition rate [39] ζ_{abs} (red) and in-band radiative power $\zeta_{in\text{-}band}$ (light blue - green) normalized by the input laser power for $I_{laser} =$ (a) 0.5, (b) 1.4, (c) 2 and (d) 5 $\times 10^{11}$ W cm^{-2}. The critical electron density (black contour) and fluid density ρ (dark blue) are indicated.

the critical electron density contour tends towards a more spherical shape, and its radius (as measured from the center of mass of the droplet, for instance) extends to larger distances. This leads to a reduction in the amount of laser radiation that "escapes" from the system, as is visible from the upper halves of the panels in Fig. 5.4. In the following, we discuss and compare the properties of these plasmas in greater detail.

5.4.1 Dependence of spatial plasma features on laser intensity

As steady-state plasma flows have been attained at $t = 18\,\text{ns}$, we can compare the spatial profiles of various plasma quantities for different laser intensities. Spatial profiles, taken along the z-axis, of all relevant variables are shown in Fig. 5.5 for $I_{\text{laser}} = \{0.5, 2, 5\} \times 10^{11}\,\text{W}\,\text{cm}^{-2}$. The profiles generated by different laser intensities are shifted by the position of the droplet surface z_{droplet}, which depends on laser intensity as seen in Fig. 5.4. Specifically, z_{droplet} is defined as the point along the z-axis where $\rho = 1\,\text{g}\,\text{cm}^{-3}$.

Examining Fig. 5.5(a), we see that the fluid density ρ looks similar for all laser intensities except in the region $0 < z - z_{\text{droplet}} < 10\,\mu\text{m}$, where higher laser intensities yield higher fluid densities. In tandem, the fluid speed $|\mathbf{v}|$ shows the opposite behaviour in this region, where higher intensities lead to lower speeds. However, for $z - z_{\text{droplet}} > 10\,\mu\text{m}$ the expected positive correlation between flow speed and intensity is established, and fluid density profiles overlap. In Fig. 5.5(a) we also plot the sound speed $c_s = \sqrt{\gamma Z_{\text{ion}} k_B T / m_{\text{ion}}}$, where γ is the adiabatic index (taken to be $\gamma = 1.167$ following Ref. [53]) and $m_{\text{ion}} = 118.71$ amu is the ion mass. The position of the sonic point (where $|\mathbf{v}| = c_s$) also moves to larger distance with increasing laser intensity. Shown in Fig. 5.5(b) are profiles of the electron density n_e and the volume-specific laser deposition rate ζ_{abs}, where the aforementioned shift of the position of the critical electron density $n_{e,cr} \approx 10^{21}\,\text{cm}^{-3}$ to larger distances with increasing I_{laser} is clearly observed.

The fluid temperature profile, shown in Fig. 5.5(c), peaks close to the position of maximum laser absorption and is found to increase with laser intensity (also see discussion in Sec. 5.4.2). The spatial profile of the average charge state Z_{ion} shown in Fig. 5.5(c) follows that of the temperature given the power law scaling $Z_{\text{ion}} \propto T^{0.6}$, see also Ref. [53]. Also presented in Fig. 5.5(c) is the volume-specific in-band radiative power $\zeta_{\text{in-band}}$, split into its positive (net emission) and negative (net absorption) branches. As before, the position of net absorption $\zeta_{\text{in-band},-}$ is located beside the droplet surface. The profile of the net emission of in-band radiation, $\zeta_{\text{in-band},+}$, exhibits a non-trivial dependence on laser intensity: with increasing I_{laser}, the spatial
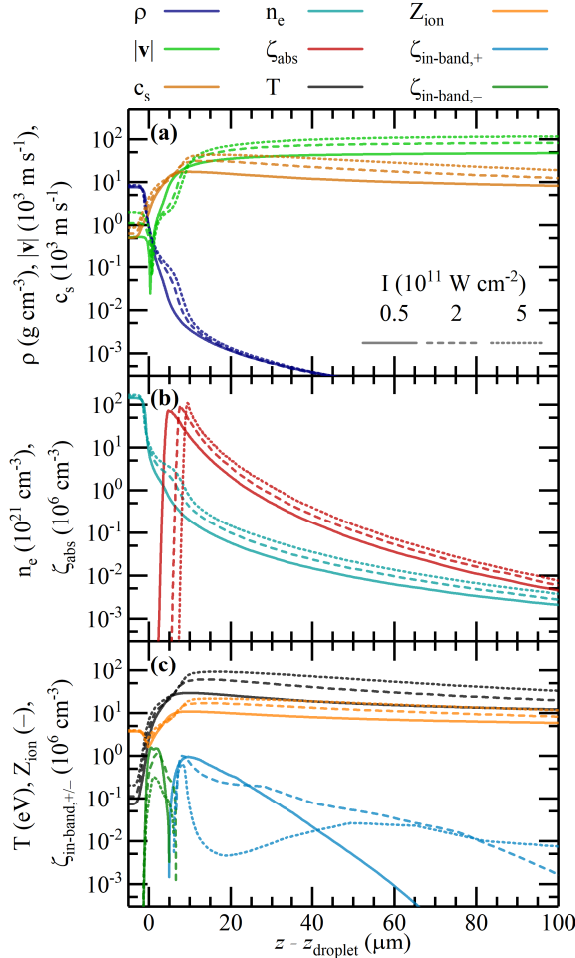
5

Figure 5.5: Spatial profiles along the laser axis (at $t = 18\,\mathrm{ns}$) for three laser intensities $I_{\mathrm{laser}} = \{0.5, 2, 5\} \times 10^{11}\,\mathrm{W\,cm^{-2}}$ and fixed laser wavelength $\lambda_{\mathrm{laser}} = 1.064\,\mu\mathrm{m}$, shown as solid, dashed, and dotted lines, respectively. The profiles are shifted in space by the position of the droplet surface, z_{droplet}. Shown are (a) fluid density ρ (dark blue), fluid speed $|\mathbf{v}|$ (light green) and sound speed c_s (brown), (b) electron density n_e (cyan) and volume-specific laser deposition rate ζ_{abs} (red), and (c) temperature T (black), average charge state Z_{ion} (orange), net in-band radiative emission power $\zeta_{\mathrm{in\text{-}band},+}$ (light blue) and net in-band radiative absorption power $\zeta_{\mathrm{in\text{-}band},-}$ (dark green).

profile first broadens and then, for $I_{laser} = 5 \times 10^{11} \, \mathrm{W \, cm^{-2}}$ exhibits a local minimum near $z - z_{droplet} = 20 \, \mu m$. This behaviour can be understood from the spatial profiles of the average charge state Z_{ion} and the fluid density ρ, respectively the location and abundance of ion charge states responsible for in-band EUV emission ($11 < Z_{ion} < 14$) [18]. Comparing the region $10 < z - z_{droplet} < 40 \, \mu m$ for the three laser intensities, the case $I_{laser} = 0.5 \times 10^{11} \, \mathrm{W \, cm^{-2}}$ is characterized by so-called "underheating" ($Z_{ion} < 11$) towards longer distances, while $I_{laser} = 5 \times 10^{11} \, \mathrm{W \, cm^{-2}}$ is characterized by "overheating" ($Z_{ion} > 14$) towards shorter distances.

5.4.2 Intensity-dependent power partitioning

We now quantify the power partitioning as a function of laser intensity, the results of which are shown in Fig. 5.6. From panel (a) we see that the absorbed power fraction remains near unity for the described intensity range. Moreover, the growth of the critical surface radius with increasing laser intensity leads to a reduction in the escaped component, while at the same time we see an increase in the reflected component.

Rather surprisingly, the ratios of the radiated and kinetic components, shown in Fig. 5.6(b) as P_{rad}/P_{abs} and P_{kin}/P_{abs}, are approximately constant over the order-of-magnitude I_{laser} range considered here. Trivially, I_{laser} is proportional to the total laser power P_{las}, and from Fig. 5.6(a) we can deduce that P_{abs} and P_{las} are equivalent for our purpose here. As such, we will only consider the intensity scaling of P_{kin} and P_{rad} in the following, having established a simple connection to the quantities shown in Fig. 5.6(b), given by

$$P_{kin}/P_{abs} \propto P_{kin} I_{laser}^{-1}, \tag{5.2}$$

$$P_{rad}/P_{abs} \propto P_{rad} I_{laser}^{-1}. \tag{5.3}$$

As steady-state flow is observed, the mass flux is conserved [51] and we can describe the system by the kinetic energy flux at any point along a flow line. We consider the scaling of kinetic energy flux with laser intensity at the sonic point. Analogous to the total laser input power argument, we consider the specific kinetic energy transfer rate I_{kin} (sometimes referred to as the kinetic energy flux density), which is proportional to the total kinetic energy transfer rate P_{kin}. The kinetic energy flux density is defined as the product of the ion number flux and the ion kinetic energy via

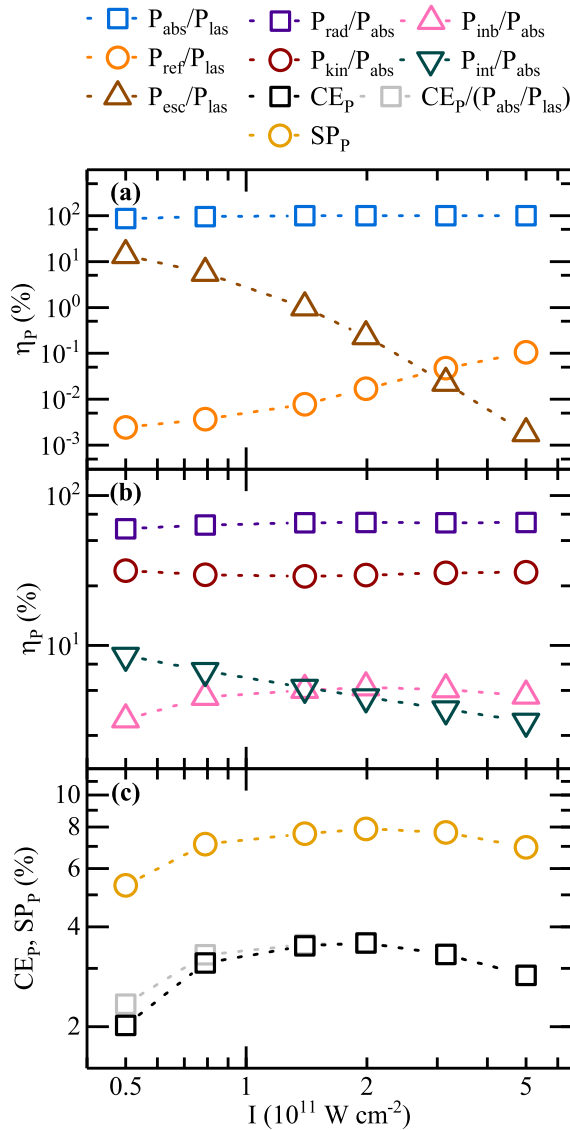$$I_{kin} = \rho |\mathbf{v}| \cdot \frac{1}{2} m_{ion} |\mathbf{v}|^2 \propto \rho |\mathbf{v}|^3 \tag{5.4}$$

5

Figure 5.6: The instantaneous (at $t = 18$ ns) partitioning of (a) laser-based components (normalized by P_{las}) (b) plasma-based components (normalized by P_{abs}) and (c) spectral purity SP_P (yellow circles), conversion efficiency CE_P (black squares) and $CE_P/(P_{abs}/P_{las})$ (gray squares) as a function of laser intensity.

which becomes $I_{\text{kin}} \propto \rho_s c_s^3$ at the sonic point. The sonic speed $c_s \propto \sqrt{Z_{\text{ion}}T}$ can be written as a sole function of temperature T through the scaling $Z_{\text{ion}} \propto T^{0.6}$. The scaling of the temperature at the sonic point T_s with laser intensity is derived from the simulation data and is given by $T_s \propto I_{\text{laser}}^{0.49}$, in close agreement with the findings of Ref. [53] and Ref. [173]. We obtain the following scaling for the kinetic energy flux density

$$I_{\text{kin}} \propto \rho_s c_s^3 \propto \rho_s I_{\text{laser}}^{1.17}, \tag{5.5}$$

very close to a linear scaling with laser intensity. Furthermore, combining the scaling of the speed with the scaling of the density $\rho_s \propto I_{\text{laser}}^{-0.22}$ at the sonic point, as obtained from the simulations, we obtain $I_{\text{kin}} \propto I_{\text{laser}}^{0.95}$ to even more accurately reproduce the linear scaling with laser intensity.

By virtue of Eq. 5.2 we can now write

$$P_{\text{kin}}/P_{\text{abs}} \propto I_{\text{kin}} I_{\text{laser}}^{-1} \propto I_{\text{laser}}^{-0.05}, \tag{5.6}$$

which underpins the observed very weak dependence of $P_{\text{kin}}/P_{\text{abs}}$ on I_{laser} as is evident from Fig. 5.6(b).

Next, we consider the scaling of the radiative energy flux density, I_{rad}, which is proportional to P_{rad}. The energy density of a non-equilibrium local radiation field (as is the case in EUV source plasmas) is often characterized by the radiation temperature $T_r = (U_r/4\sigma_{\text{SB}})^{1/4}$, where σ_{SB} is the Stefan-Boltzmann constant and

$$U_r = \int_{4\pi} \int_0^\infty I_\nu \, d\nu d\vec{\Omega} \tag{5.7}$$

is the 4π- and frequency-integrated specific intensity of the radiation field I_ν. Clearly, one can write

$$I_{\text{rad}} \propto U_r \propto T_r^4. \tag{5.8}$$

From the RALEF-2D simulations we find the scaling $T_{r,\text{max}} \propto I_{\text{laser}}^{0.24}$ and therefore the following relationship holds *locally*

$$I_{\text{rad}} \propto I_{\text{laser}}^{0.96}. \tag{5.9}$$

Based on Eq. 5.3, we conclude that there is a near-independence of the radiation component on the laser intensity as

$$P_{\text{rad}}/P_{\text{abs}} \propto I_{\text{laser}}^{0.96} I_{\text{laser}}^{-1} \propto I_{\text{laser}}^{-0.04}. \tag{5.10}$$

The dependence of conversion efficiency CE_P on laser intensity, shown in Fig. 5.6(c), follows the same trend as the spectral purity (SP_P) with a maximum at $I_{laser} = 2 \times 10^{11} \, W \, cm^{-2}$. This is due to the near-independence of P_{rad}/P_{abs} and P_{abs}/P_{las} on laser intensity, the exact opposite of what was found in Sec. 5.3.2. As such, the effect of optimizing the absorption ratio by reducing the escaped laser component ($CE_P/(P_{abs}/P_{las})$) does not shift the found maximum as is clear from Fig. 5.6(c). Combining the dependences of P_{rad}/P_{abs} and CE_P on I_{laser}, we see that increasing laser intensity can yield a significant increase in absolute in-band radiation without significantly influencing the conversion efficiency of the system.

5.5   Summary and conclusion

In summary, we have investigated the power partitioning in a laser-produced tin plasma for laser wavelengths in the $1.064 \leq \lambda_{laser} \leq 10.6 \, \mu m$ range and laser intensities of $0.5 \times 10^{11} \leq I_{laser} \leq 5 \times 10^{11} \, W \, cm^{-2}$ for $\lambda_{laser} = 1.064 \, \mu m$. We have identified a strong laser-wavelength dependence of laser absorptivity and the location of EUV generation. With increasing laser wavelength, the power balance monotonically shifts from kinetic losses to in-band radiative losses. The decrease in laser absorption for long laser wavelengths, combined with a concurrent decrease in EUV optical depth, yields a non-monotonic behaviour of the conversion efficiency, leading to an optimum at $\lambda_{laser} = 4 \, \mu m$. EUV sources based on long laser wavelengths would therefore benefit from additional target preparation to ensure a higher absorption fraction. The influence of laser intensity on the power partitioning for $\lambda_{laser} = 1.064 \, \mu m$ is found to be small: no significant shift between kinetic losses and radiative losses is seen. With increasing laser intensity, we find an increase in in-band radiative power at minor cost in terms of conversion efficiency.

Acknowledgements

Conclusion and outlook

In this thesis, work is presented on radiation-hydrodynamic modeling of tin droplet-based laser-produced plasmas. Over the course of five chapters, four topics are discussed in detail: after a discussion in Ch. 1 of the plasma physics underlying the numerical modeling, this thesis considers plasma expansion in Ch. 2 and 3, plasma-induced droplet dynamics in Ch. 4 and plasma characterization in Ch. 5. The first section of this concluding chapter consists of a short summary and key conclusions from the work presented in this thesis. In the second section, a potential direction for future research will be discussed.

The work is guided by the quest of the nanolithography industry to increase the performance of the light source, a laser-produced tin plasma whose most important feature is the emission of extreme ultraviolet radiation. The work aims to specifically contribute to the investigation of solid-state laser-driven EUV sources, such as Nd:YAG-laser illumination ($\lambda_{\text{laser}} = 1.064\,\mu\text{m}$) featured in Ch. 2 – 4. Such solid-state lasers may drive future EUV light sources for EUV nanolithography given their larger efficiency in converting electrical power into laser light when compared to the currently used CO_2-gas lasers as well as their potential for scaling to high average powers. Central to the presented work are tin plasmas generated on tin micrometer-sized droplets by these solid-state lasers. In chronological order in a laser-droplet system, the investigation encompasses plasma formation from the droplet surface, its temporal and spatial dynamics, its rarefaction flow as it distributes over space, and its

C

interaction with the remaining droplet volume. This last effect, the plasma pressure impulse, leads to propulsion and initiates the subsequent deformation dynamics of the droplet, which lasts long after the plasma has subsided. Although all subtopics start with the formation of plasma and its dynamics during laser illumination, chapter 5 focuses explicitly on this topic. There, the absorption and emission properties of a steady-state plasma flow are characterized as a function of laser wavelength and intensity. Generally, the performance of the EUV source is approached from two sides: radiative efficiency and tin debris generation, which are important for the necessary EUV light generation and system uptime, respectively. The efficiency of generating in-band EUV light from laser light, that is, the conversion efficiency (CE), is the focus of the plasma characterization presented in Ch. 5. Moreover, in Ch. 4 the physical parameters that determine the final morphology of a deformed droplet are explored in detail. This final morphology may affect the obtainable CE. In addition, a substantial part of the research efforts is devoted to plasma expansion dynamics, i.e., the generation of ionic debris, as presented in Ch. 2 and 3, contributing to the industrial task of ion mitigation by extensive characterization of the ion emission characteristics.

1   Conclusion

First, the aim of this thesis is reiterated here: to investigate the suitability of applying single-fluid radiation-hydrodynamic modeling to laser-produced, EUV-emitting plasmas and, next, to utilize it to guide experiments, with the ambition to enable designing next-generation EUV light sources.

Chapters 2 – 4 feature validation of the simulation code and the implemented approach in the context of plasma expansion and early-time droplet dynamics. Subsequently, the simulations are used to deepen the understanding into these processes. On this foundation, further investigations are built, as presented in Ch. 5, which may guide future experiments. In the following section, first the key features of the simulation approach are highlighted, followed by a discussion of the successful validation efforts. Then, some key new insights and conclusions are discussed, as presented in the first three chapters of this thesis. Lastly, the research of Ch. 5 is reviewed.

   The plasma modeling approach employed in this work is based on a single-fluid, single-temperature model, which includes substantial simplifications. In Ch. 1, the fluid equations are derived from particle kinetic theory. Simplifying assumptions are included of both quasi-neutrality and of equal temperature of the ions and electrons

in the plasma. These are applicable to the laser-produced tin plasma (under EUV emission conditions) due to its small Debye length relative to any density gradients, as well as high plasma densities which lead to a high electron–ion collision rate. The single-fluid, single-temperature approach is validated on two distinct types of experimental measurements. First, the fluid approach is extensively assessed in the context of plasma expansion and good agreement is reported between the ion kinetic energy distributions from experiment and simulation. This includes the non-trivial shape of the distribution and the absolute number of ions integrated over energy. This agreement between simulation and experiment also extends to a multitude of measurement angles, enabling a quantitative understanding of the spatial distribution of highly energetic ionic debris. While the overall shape of the ion kinetic energy distribution is reproduced by the single-fluid simulations, there are some differences. A rather abrupt fall-off of the simulated distribution is observed toward the highest kinetic energies. The apparent disadvantage of the simplifications of fluid theory in comparison to kinetic theory is the reduction of the intrinsic particle velocity distribution to a single average velocity. This overlooks the Maxwell–Boltzmann distribution of particle velocities around an average velocity, which also holds for the maximum value currently captured in the simulations. In combination with the limited spatial resolution at the mesh boundary, this leads to the assignment of a single kinetic energy value to a relatively large amount of mass. The experimentally observed high-energy 'tails' are therefore not captured in the simulations. Secondly, in Ch. 4, the fluid approach is successfully applied to the early-time hydrodynamic evolution of a laser-irradiated tin micro-droplet. Although its applicability is restricted to early times when surface tension does not yet play a role, the simulated droplet dynamics is in agreement with experimental measurements for a wide range of laser and droplet parameters. The early-time propulsion and deformation of the tin microdroplet ultimately determine the late-time morphology of the pizza-like target. For example, our (experimental) results indicate that the use of smaller droplets leads to flatter morphologies and faster expansion and propulsion velocities.

After validation of the approach in both subfields, the numerical simulations lead to new findings, thereby enriching the experimental studies. In the case of plasma expansion, the detailed temporal and spatial resolution of the plasma density and velocity leads to insight in the underlying dynamics, shaping the measured ion kinetic energy distribution. The existence of a peak in the distribution is attributed to a quasi-spherical expanding shell which is formed at early times, during laser illumination. The strongly anisotropic ion emission characteristics found in subsequent experiments are related to its quasi-spherical nature (cf. Ch. 3). The droplet

dynamics is set in motion by the plasma pressure at the droplet-plasma interface, as theoretically proposed, which is now quantified by the simulations. The width of the plasma pressure impulse, as quantified by the simulations, is identified as the sole pertinent parameter for the kinetic energy partitioning over propulsion and deformation. So, after validation by the experimental measurements, the modeling is used to enrich the research of laser-produced tin plasmas. Its contribution lies in the calculation and visualization of the complex plasma dynamics and its aftermath, which is unavailable from direct experimental measurements.

Furthermore, as a result of the temporal resolution of the simulations, the presented findings underline the importance of understanding the temporal evolution of the plasma, both during the laser pulse and afterward. On the one hand, from investigation of the plasma expansion, the transient conditions during a 10-ns Gaussian laser pulse lead to a quasi-spherical density shell, ultimately resulting in a non-trivial ion kinetic energy distribution. These conditions make analytical solutions unable to reproduce the plasma density profile and its associated number distribution over energy. The formation of a density shell, which is due to two distinct bursts of laser-induced ablation, points to a general sensitivity of the kinetic energy distribution to the temporal profile of the laser pulse. On the other hand, as part of the work on plasma characterization in Ch. 5, different laser illumination, now constant in time, leads to steady-state ablation flow, where the spatial profiles do not change in time. This has allowed characterization through the instantaneous, converged power partitioning in the plasma. Additionally, this allows extrapolation of the results to longer pulse lengths. This observation leads to the topic of the Outlook section below.

In the final chapter 5, a next step in the simulation-based research is undertaken. After validation of the simulation approach and already proving its ability to provide new insights, a parameter space is explored that is currently inaccessible to experiments. Changing the laser wavelength driving the plasma fundamentally influences its properties, as exemplified by the dependence of the critical electron density on laser wavelength. In the context of the droplet case study, the quantification of the laser absorption and EUV emission uncovers a trade-off between both quantities in the range $\lambda_{laser} = 1.064 - 10.6\,\mu m$. The combination of laser absorptivity and optical depth for EUV photons in densities set by the laser wavelength determines the conversion efficiency for the investigated laser wavelength range. Moreover, the work in Ch. 5 aims to guide future experiments in search of improved EUV source performance, especially those based on solid-state lasers. Important in this context is an increase in conversion efficiency from $\lambda_{laser} = 1.064$ to $2\,\mu m$, which is attributed to
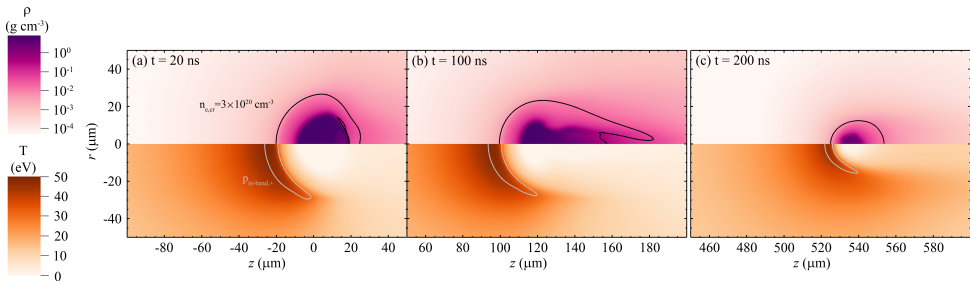
Figure C.1: The fluid density and plasma temperature during constant illumination by a (200 ns) 2 μm laser pulse at (a) $t = 20$, (b) $t = 100$ and (c) $t = 200$ ns. The critical electron density (black contour) is indicated, as well as the net in-band radiative emission represented by a (gray) contour at the half-maximum value of in-band radiative power per unit volume.

an increase in spectral purity without a loss in laser absorptivity. Additionally, an opportunity for increasing EUV power presents itself when employing increased laser intensities for $\lambda_{\text{laser}} = 1.064$ μm: For increased laser intensity, absolute in-band radiative power increases without a significant decrease in conversion efficiency.

In conclusion, the propriety of applying single-fluid radiation-hydrodynamic modeling to EUV source plasmas is successfully demonstrated, both in the context of plasma expansion and plasma-induced droplet dynamics. Capitalizing on this, the capability is used to deepen the understanding of the plasma physics and guide current and future experiments toward truly optimal plasma conditions.

2 Outlook

In this section, a conclusion from the work in Ch. 5 is pursued further, which is a new opportunity to validate the simulation approach, provide new insights, and guide future experiments.

As alluded to in Ch. 5, an opportunity lies in plasmas driven by a solid-state laser operating at a wavelength of $\lambda_{\text{laser}} = 2$ μm. Such a solid-state laser system benefits from advantages such as having a high efficiency in converting electrical power to laser light and the potential for scaling to high average powers. The plasma generated by a 2 μm laser obtains near-unity absorptivity and shows improvement in conversion efficiency in comparison to a 1.064 μm laser system. The first point leads to the conclusion that further target shaping by a pre-pulse is unnecessary to improve laser absorptivity, in contrast to the CO_2 laser case. The second point is directly related to the lower plasma densities, improving the spectral purity as a

result of reduced spectral broadening. Additionally, the work in Ch. 5 shows two more observations. Within the employed pulse length (20 ns), a steady-state flow is reached, which leads to the hypothesis that longer pulse lengths yield a similar power partitioning, i.e., continuous emission of EUV with constant conversion efficiency. After the employed 20 ns pulse, a significant amount of tin mass is left in the droplet, i.e., the mass efficiency of the system is suboptimal. Longer pulse lengths increase the tin droplet fraction utilized for plasma formation, thereby minimizing liquid tin debris. Therefore, further investigation is proposed of droplet-based EUV sources driven by a 2 µm laser with a long pulse length to enable optimal tin mass use. It is envisioned that the simulation approach presented in this thesis is suited to explore the large parameter space that comes with a new laser–droplet setup. Two new numerical challenges may arise in this new setup. First, radiation transport must be simulated for the duration of the (long) pulse. Its computationally heavy nature may require simplifications in its implementation or facilitation of a longer wall-clock time. Second, to account for the kinetic energy loss, all fluid mass must be contained in the simulation domain for the full pulse length. Additionally, employing more realistic laser focusing conditions, i.e., a finite Rayleigh length, could be considered to increase the predictive value of the simulations. Simulations may be used as a guide toward a reduced set of conditions, which can be subsequently investigated by experimental measurements.

Some first results are presented in Fig. C.1 of an EUV source generated on tin microdroplets by long-pulse 2 µm laser illumination. As a test case, a 30 µm-diameter droplet is considered, irradiated by a 2 µm laser beam with a constant intensity of 0.7×10^{11} W cm^{-2}. In Fig. C.1 the fluid density and plasma temperature are shown at three times during constant illumination by a 2 µm laser pulse. At $t = 20$ ns steady-state flow is reached, as previously described in Ch. 5. The in-band radiative emission region is schematically shown as a contour of net in-band emission at half-maximum power (per unit volume). This region extends up to the laser beam diameter of 60 µm at $t = 20$ ns. Later, at $t = 100$ ns, the droplet–plasma system is propelled along the laser axis. A slight reduction in droplet radius is observed, as well as the formation of a liquid 'tail' in the shadow of the droplet, which originates from flow of liquid mass to the back. Also, the radii of the critical surface and in-band emission region are reduced. Finally, at $t = 200$ ns, the mass-limited nature of the 30 µm droplet is observed: the liquid volume significantly shrinks in radius while being propelled further. This causes a reduction of the radius of the critical surface, the laser-produced plasma, and consequently the in-band emission region. For the simulation presented here, the instantaneous CE (CE$_P$ in Ch. 5) remains around 5% up to approximately 170 ns, resulting in a (power-integrated) CE

of 4.8% at $t = 200$ ns. This translates to an in-band radiative energy into the laser-illuminated half-sphere of approximately 20 mJ for this test case with a 200 ns-long 2 μm laser pulse.

The above observations point toward features that define new research questions for further investigation. The movement of the droplet target, and thereby the EUV emission region, leads to an EUV emission volume significantly extended in the axial direction. At the same time, the plasma volume reduces in radial size over time, as can be quantified by the critical surface radius, causing more laser light to escape instead of being absorbed. Still, the CE does not significantly reduce up to approximately 170 ns, at which nearly all initial mass is ablated and converted to plasma. Lastly, the movement of the droplet target during laser illumination requires consideration of the (experimental) laser focusing conditions.

These preliminary simulation results clearly demonstrate that an EUV-emitting laser-produced plasma based on only a single (long) laser pulse can make full use of the provided liquid tin mass while maintaining a high CE over time. This reveals opportunities for delivering high in-band EUV energy in a single pulse. Future work should focus on addressing the related open research questions, building further on the results and validation presented in this thesis.

Bibliography

[1] I. Langmuir, *Oscillations in ionized gases*, Proc. Natl. Acad. Sci. **14**, 627–637 (1928).

[2] P. W. Hatfield, J. A. Gaffney, G. J. Anderson, S. Ali, L. Antonelli, S. B. du Pree, J. Citrin, M. Fajardo, P. Knapp, B. Kettle, B. Kustowski, M. J. MacDonald, D. Mariscal, M. E. Martin, T. Nagayama, C. A. J. Palmer, J. L. Peterson, S. Rose, J. J. Ruby, C. Shneider, M. J. V. Streeter, W. Trickey, and B. Williams, *The data-driven future of high-energy-density physics*, Nature **593**, 351–361 (2021).

[3] *The ITER tokamak*, English, Accessed: 2023-04-04, ITER organization, (2023) `https://web.archive.org/web/20230404124700/https://www.iter.org/mach`.

[4] H. Abu-Shawareb et al., *Lawson Criterion for Ignition Exceeded in an Inertial Fusion Experiment*, Phys. Rev. Lett. **129**, 075001 (2022).

[5] B. Bishop, *Lawrence Livermore National Laboratory achieves fusion ignition*, English, Accessed: 2023-05-05, Lawrence Livermore National Laboratory, (Dec. 2022) `https://web.archive.org/web/20230505101354/https://www.llnl.gov/news/lawrence-livermore-national-laboratory-achieves-fusion-ignition`.

[6] V. Bakshi, ed., *EUV Lithography*, 2nd edition (SPIE Press, 2018).

[7]I. Fomenkov, D. Brandt, A. Ershov, A. Schafgans, Y. Tao, G. Vaschenko, S. Rokitski, M. Kats, M. Vargas, M. Purvis, R. Rafac, B. La Fontaine, S. De Dea, A. LaForge, J. Stewart, S. Chang, M. Graham, D. Riggs, T. Taylor, M. Abraham, and D. Brown, *Light sources for high-volume manufacturing EUV lithography: technology, performance, and power scaling*, Adv. Opt. Techn. **6**, 173–186 (2017).

[8]P. J. Denning and T. G. Lewis, *Exponential laws of computing growth*, Commun. ACM **60**, 54–65 (2017).

[9]G. E. Moore, *Cramming more components onto integrated circuits*, Electronics **38**, 114–117 (1965).

[10]G. E. Moore, *Progress in digital integrated electronics*, Proc. IEDM Tech. Dig., 11–13 (1975).

[11]J. G. Koomey, S. Berard, M. Sanchez, and H. Wong, *Implications of historical trends in the electrical efficiency of computing*, IEEE Ann. Hist. Comput. **33**, 46–54 (2011).

[12]C. Smeets, N. Benders, F. Bornebroek, J. Carbone, R. V. Es, A. Minnaert, G. Salmaso, and S. Young, *0.33 NA EUV systems for high volume manufacturing*, in Optical and EUV nanolithography XXXVI, edited by A. Lio and M. Burkhardt (Apr. 2023).

[13]S. Bajt, J. B. Alameda, T. W. Barbee Jr., W. M. Clift, J. A. Folta, B. Kaufmann, and E. A. Spiller, *Improved reflectance and stability of Mo-Si multilayers*, Opt. Eng. **41**, 1797–1804 (2002).

[14]Q. Huang, V. Medvedev, R. van de Kruijs, A. Yakshin, E. Louis, and F. Bijkerk, *Spectral tailoring of nanoscale EUV and soft x-ray multilayer optics*, Appl. Phys. Rev. **4**, 011104 (2017).

[15]S. S. Churilov and A. N. Ryabtsev, *Analyses of the Sn IX–Sn XII spectra in the EUV region*, Phys. Scr. **73**, 614 (2006).

[16]A. Sasaki, A. Sunahara, H. Furukawa, K. Nishihara, S. Fujioka, T. Nishikawa, F. Koike, H. Ohashi, and H. Tanuma, *Modeling of radiative properties of Sn plasmas for extreme-ultraviolet source*, J. Appl. Phys. **107**, 113303 (2010).

[17]G. O'Sullivan, B. Li, R. D'Arcy, P. Dunne, P. Hayden, D. Kilbane, T. McCormack, H. Ohashi, F. O'Reilly, P. Sheridan, E. Sokell, C. Suzuki, and T. Higashiguchi, *Spectroscopy of highly charged ions and its relevance to EUV and soft x-ray source development*, J. Phys. B: At. Mol. Opt. Phys. **48**, 144025 (2015).

[18]F. Torretti, J. Sheil, R. Schupp, M. M. Basko, M. Bayraktar, R. A. Meijer, S. Witte, W. Ubachs, R. Hoekstra, O. O. Versolato, A. J. Neukirch, and J. Colgan, *Prominent radiative contributions from multiply-excited states in laser-produced tin plasma for nanolithography*, Nat. Commun. **11** (2020).

[19]J. Sheil, O. O. Versolato, A. J. Neukirch, and J. Colgan, *Multiply-excited states and their contribution to opacity in CO_2 laser-driven tin-plasma conditions*, J. Phys. B **54**, 035002 (2021).

[20]S. Fujioka, H. Nishimura, K. Nishihara, M. Murakami, Y.-G. Kang, Q. Gu, K. Nagai, T. Norimatsu, N. Miyanaga, Y. Izawa, and K. Mima, *Properties of ion debris emitted from laser-produced mass-limited tin plasmas for extreme ultraviolet light source applications*, Appl. Phys. Lett. **87**, 241503 (2005).

[21]S. Fujioka, M. Shimomura, Y. Shimada, S. Maeda, H. Sakaguchi, Y. Nakai, T. Aota, H. Nishimura, N. Ozaki, A. Sunahara, K. Nishihara, N. Miyanaga, Y. Izawa, and K. Mima, *Pure-tin microdroplets irradiated with double laser pulses for efficient and minimum-mass extreme-ultraviolet light source production*, Appl. Phys. Lett. **92**, 241502 (2008).

[22]D. Nakamura, K. Tamaru, Y. Hashimoto, T. Okada, H. Tanaka, and A. Takahashi, *Mitigation of fast ions generated from laser-produced Sn plasma for extreme ultraviolet light source by H_2 gas*, J. Appl. Phys. **102**, 123310 (2007).

[23]D. B. Abramenko, M. V. Spiridonov, P. V. Krainov, V. M. Krivtsun, D. I. Astakhov, V. V. Medvedev, M. van Kampen, D. Smeets, and K. N. Koshelev, *Measurements of hydrogen gas stopping efficiency for tin ions from laser-produced plasma*, Appl. Phys. Lett. **112**, 164102 (2018).

[24]A. L. Klein, C. W. Visser, W. Bouwhuis, H. Lhuissier, C. Sun, J. H. Snoeijer, E. Villermaux, D. Lohse, and H. Gelderblom, *Laser impact on a drop*, Phys. Fluids **27**, 091106 (2015).

[25]D. Kurilovich, A. L. Klein, F. Torretti, A. Lassise, R. Hoekstra, W. Ubachs, H. Gelderblom, and O. O. Versolato, *Plasma propulsion of a metallic microdroplet and its deformation upon laser impact*, Phys. Rev. Appl. **6**, 014018 (2016).

[26]B. Liu, D. Kurilovich, H. Gelderblom, and O. O. Versolato, *Mass loss from a stretching semitransparent sheet of liquid tin*, Phys. Rev. Appl. **13**, 024035 (2020).

[27]I. Tamer, B. A. Reagan, T. Galvin, J. Galbraith, E. Sistrunk, A. Church, G. Huete, H. Neurath, and T. Spinka, *Demonstration of a compact, multi-joule, diode-pumped Tm:YLF laser*, Opt. Lett. **46**, 5096–5099 (2021).

[28] O. O. Versolato, J. Sheil, S. Witte, W. Ubachs, and R. Hoekstra, *Microdroplet-tin plasma sources of EUV radiation driven by solid-state-lasers (Topical Review)*, J. Opt. **24**, 054014 (2022).

[29] S. Eliezer and Y. Eliezer, *The Fourth State of Matter: An Introduction to Plasma Science*, Second Edition (Institute of Physics Publishing, Bristol and Philadelphia, 2001).

[30] R. A. Meijer, D. Kurilovich, B. Liu, Z. Mazzotta, J. Hernandez-Rueda, O. O. Versolato, and S. Witte, *Nanosecond laser ablation threshold of liquid tin microdroplets*, Appl. Phys. A **128** (2022).

[31] A. Macchi, M. Borghesi, and M. Passoni, *Ion acceleration by superintense laser-plasma interaction*, Rev. Mod. Phys. **85**, 751–793 (2013).

[32] S. Eliezer, *The Interaction of High-Power Lasers with Plasmas* (CRC Press, 2002).

[33] V. Bakshi, ed., *EUV Sources for Lithography*, SPIE Press monograph (SPIE Press, 2006).

[34] O. O. Versolato, *Physics of laser-driven tin plasma sources of EUV radiation for nanolithography*, Plasma Sources Sci. Tech. **28**, 083001 (2019).

[35] J. A. Bittencourt, *Fundamentals of plasma physics* (Springer New York, 2004).

[36] M. Murakami and M. M. Basko, *Self-similar expansion of finite-size non-quasi-neutral plasmas into vacuum: relation to the problem of ion acceleration*, Phys. Plasmas **13**, 012105 (2006).

[37] A. Sunahara and K. Tanaka, *Atomic number Z dependence of dynamics of laser-ablated materials*, Fus. Eng. Des. **85**, 935–939 (2010).

[38] A. Z. Giovannini and R. S. Abhari, *Three-dimensional extreme ultraviolet emission from a droplet-based laser-produced plasma*, J. Appl. Phys. **114**, 033303 (2013).

[39] M. M. Basko and I. P. Tsygvintsev, *A hybrid model of laser energy deposition for multi-dimensional simulations of plasmas and metals*, Comp. Phys. Comm. **214**, 59–70 (2017).

[40] A. F. Nikiforov, V. G. Novikov, and V. B. Uvarov, *Quantum-Statistical Models of Hot Dense Matter: Methods for Computation Opacity and Equation of State (Progress in Mathematical Physics)* (Birkhauser, 2005).

[41] V. G. Novikov, V. V. Ivanov, K. N. Koshelev, V. M. Krivtsun, and A. D. Solomyannaya, *Calculation of tin emission spectra in discharge plasma: the influence of reabsorption in spectral lines*, High Energy Density Phys. **3**, 198–203 (2007).

[42]T. Pütterich, R. Neu, R. Dux, A. D. Whiteford, M. G. O'Mullane, and the ASDEX Upgrade Team, *Modelling of measured tungsten spectra from ASDEX Upgrade and predictions for ITER*, Plasma Phys. Control. Fusion **50**, 085016 (2008).

[43]M. M. Basko, J. Maruhn, and A. Tauschwitz, *RALEF-2D: A 2D hydrodynamic code with heat conduction and radiation transport*, Main Report (2017).

[44]M. Basko, J. Maruhn, and A. Tauschwitz, *CAVEAT-TR: A 2D hydrodynamic code with heat conduction and radiation transport. I. Implementation of the SSI method for heat conduction*, GSI Report **2007-05**, Darmstadt (2007).

[45]L. P. Pitaevskii and E. M. Lifshitz, *Physical Kinetics*, Vol. 10, Course of Theoretical Physics (Elsevier, 1981).

[46]J. D. Huba, *NRL Plasma Formulary*, tech. rep. NRL/PU/6790–04-477 (Naval Research Laboratory, Washington, DC 20375-5320, 2004).

[47]N. Ashcroft and N. D. Mermin, *Solid State Physics*, edited by D. G. Crane (AIP Publishing, 1976).

[48]T. B. Kaiser, *Laser ray tracing and power deposition on an unstructured three-dimensional grid*, Phys. Rev. E **61**, 895–905 (2000).

[49]Y. Zel'dovich and Y. Raizer, *Physics of Shock Waves and High-Temperature Hydrodynamic Phenomena* (Academic Press, 1966).

[50]L. Oster, *Emission, absorption, and conductivity of a fully ionized gas at radio frequencies*, Rev. Mod. Phys. **33**, 525 (1961).

[51]M. Basko, *On the maximum conversion efficiency into the 13.5-nm extreme ultraviolet emission under a steady-state laser ablation of tin microspheres*, Phys. Plasmas **23**, 083114 (2016).

[52]S. Faik, A. Tauschwitz, and I. Iosilevskiy, *The equation of state package FEOS for high energy density matter*, Comp. Phys. Comm. **227**, 117–125 (2018).

[53]M. M. Basko, V. G. Novikov, and A. S. Grushin, *On the structure of quasi-stationary laser ablation fronts in strongly radiating plasmas*, Phys. Plasmas **22**, 053111 (2015).

[54]A. J. Kemp and J. Meyer-ter Vehn, *An equation of state code for hot dense matter, based on the QEOS description*, Nucl. Instrum. Methods Phys. Res. A **415**, 674–676 (1998).

[55]R. M. More, K. H. Warren, D. A. Young, and G. B. Zimmerman, *A new quotidian equation of state (QEOS) for hot dense matter*, Phys. Fluids **31**, 3059–3078 (1988).

[56] R. P. Feynman, N. Metropolis, and E. Teller, *Equations of state of elements based on the generalized fermi-thomas theory*, Phys. Rev. **75**, 1561–1573 (1949).

[57] L. D. Landau and E. M. Lifshitz, *Fluid Mechanics*, Second English Edition, Revised, Vol. 6, Course of Theoretical Physics, Translated from the Russian by J. B. Sykes and W. H. Reid (Butterworth-Heinemann, Oxford, 1987).

[58] A. V. Gurevich, L. V. Pariĭskaya, and L. P. Pitaevskiĭ, *Self-similar motion of rarefied plasma*, Sov. Phys. JETP **22**, 449–454 (1966).

[59] M. Murakami, Y.-G. Kang, K. Nishihara, S. Fujioka, and H. Nishimura, *Ion energy spectrum of expanding laser-plasma with limited mass*, Phys. Plasmas **12**, 062706 (2005).

[60] P. Mora, *Plasma expansion into a vacuum*, Phys. Rev. Lett. **90** (2003).

[61] A. Bayerle, M. J. Deuzeman, S. van der Heijden, D. Kurilovich, T. de Faria Pinto, A. Stodolna, S. Witte, K. S. E. Eikema, W. Ubachs, R. Hoekstra, and O. O. Versolato, *Sn ion energy distributions of ns- and ps-laser produced plasmas*, Plasma Sources Sci. Tech. **27**, 045001 (2018).

[62] A. S. Stodolna, T. de Faria Pinto, F. Ali, A. Bayerle, D. Kurilovich, J. Mathijssen, R. Hoekstra, O. O. Versolato, K. S. E. Eikema, and S. Witte, *Controlling ion kinetic energy distributions in laser produced plasma sources by means of a picosecond pulse pair*, J. Appl. Phys. **124**, 053303 (2018).

[63] D. C. Brandt, I. Fomenkov, and J. Stewart, *Progress in availably of NXE:3400B EUVL sources in the field and power scaling towards 500W (Conference Presentation)*, in Extreme Ultraviolet (EUV) Lithography XI, Vol. 11323, edited by N. M. Felix and A. Lio (International Society for Optics and Photonics, 2020).

[64] W. Svendsen and G. O'Sullivan, *Statistics and characteristics of xuv transition arrays from laser-produced plasmas of the elements tin through iodine*, Phys. Rev. A **50**, 3710–3718 (1994).

[65] P. Hayden, A. Cummings, N. Murphy, G. O'Sullivan, P. Sheridan, J. White, and P. Dunne, *13.5 nm extreme ultraviolet emission from tin based laser produced plasma sources*, J. Appl. Phys. **99**, 093302 (2006).

[66] R. Schupp, F. Torretti, R. A. Meijer, M. Bayraktar, J. Scheers, D. Kurilovich, A. Bayerle, K. S. E. Eikema, S. Witte, W. Ubachs, R. Hoekstra and O. O. Versolato, *Efficient generation of extreme ultraviolet light from Nd:YAG-driven microdroplet-tin plasma*, Phys. Rev. Appl. **12**, 014010 (2019).

[67] A. N. Ryabtsev and E. Y. Kononov, *Resonance transitions in the Pd VII spectrum*, Phys. Scr. **85**, 025301 (2012).

[68]J. Colgan, D. Kilcrease, J. Abdallah, M. Sherrill, C. Fontes, P. Hakel, and G. Armstrong, *Atomic structure considerations for the low-temperature opacity of Sn*, High Energy Density Phys. **23**, 133 –137 (2017).

[69]J. Scheers, C. Shah, A. Ryabtsev, H. Bekker, F. Torretti, J. Sheil, D. A. Czapski, J. C. Berengut, W. Ubachs, J. R. C. López-Urrutia, R. Hoekstra, and O. O. Versolato, *EUV spectroscopy of highly charged $Sn^{13+} - Sn^{15+}$ ions in an electron-beam ion trap*, Phys. Rev. A **101**, 062511 (2020).

[70]K. Nishihara, A. Sunahara, A. Sasaki, M. Nunami, H. Tanuma, S. Fujioka, Y. Shimada, K. Fujima, H. Furukawa, T. Kato, F. Koike, R. More, M. Murakami, T. Nishikawa, V. Zhakhovskii, K. Gamata, A. Takata, H. Ueda, H. Nishimura, Y. Izawa, N. Miyanaga, and K. Mima, *Plasma physics and radiation hydrodynamics in developing an extreme ultraviolet light source for lithography*, Phys. Plasmas **15**, 056708 (2008).

[71]S. S. Harilal, B. OShay, and M. S. Tillack, *Debris mitigation in a laser-produced tin plume using a magnetic field*, J. Appl. Phys. **98**, 036102 (2005).

[72]Y. Ueno, G. Soumagne, A. Sumitani, A. Endo, T. Higashiguchi, and N. Yugami, *Reduction of debris of a CO_2 laser-produced Sn plasma extreme ultraviolet source using a magnetic field*, Appl. Phys. Lett. **92**, 211503 (2008).

[73]H. Mizoguchi, H. Nakarai, T. Abe, H. Tanaka, Y. Watanabe, T. Hori, Y. Shiraishi, T. Yanagida, G. Soumagne, T. Yamada, and T. Saitou, *Challenge of >300W high power LPP-EUV source with long collector mirror lifetime for semiconductor HVM*, in Extreme Ultraviolet (EUV) Lithography XI, Vol. 11323, edited by N. M. Felix and A. Lio (International Society for Optics and Photonics, 2020), pp. 225 –238.

[74]A. Roy, S. S. Harilal, M. P. Polek, S. M. Hassan, A. Endo, and A. Hassanein, *Influence of laser pulse duration on extreme ultraviolet and ion emission features from tin plasmas*, Phys. Plasmas **21**, 033109 (2014).

[75]R. A. Burdt, Y. Tao, M. S. Tillack, S. Yuspeh, N. M. Shaikh, E. Flaxer, and F. Najmabadi, *Laser wavelength effects on the charge state resolved ion energy distributions from laser-produced Sn plasma*, J. Appl. Phys. **107**, 043303 (2010).

[76]D. Campos, S. S. Harilal, and A. Hassanein, *The effect of laser wavelength on emission and particle dynamics of Sn plasma*, J. Appl. Phys. **108**, 113305 (2010).

[77]T. Higashiguchi, C. Rajyaguru, N. Dojyo, Y. Taniguchi, K. Sakita, S. Kubodera, and W. Sasaki, *Debris characteristics of a laser-produced tin plasma for extreme ultraviolet source*, Rev. Sci. Instrum. **76**, 126102 (2005).

[78]O. Morris, F. O'Reilly, P. Dunne, and P. Hayden, *Angular emission and self-absorption studies of a tin laser produced plasma extreme ultraviolet source between 10 and 18 nm*, Appl. Phys. Lett. **92**, 2006–2009 (2008).

[79]O. Morris, A. O'Connor, E. Sokell, and P. Dunne, *Angular distribution of the ion emission from a tin-based laser-produced plasma extreme ultraviolet source*, Plasma Sources Sci. Tech. **19**, 025007 (2010).

[80]A. O'Connor, O. Morris, and E. Sokell, *Angular and energy distribution of Sn ion debris ejected from a laser-produced plasma source, for laser power densities in the range suitable for extreme ultraviolet lithography*, J. Appl. Phys. **109**, 073301 (2011).

[81]A. Z. Giovannini, N. Gambino, B. Rollinger, and R. S. Abhari, *Angular ion species distribution in droplet-based laser-produced plasmas*, J. Appl. Phys. **117**, 033302 (2015).

[82]Y. Tao and M. S. Tillack, *Mitigation of fast ions from laser-produced Sn plasma for an extreme ultraviolet lithography source*, Appl. Phys. Lett. **89**, 111502 (2006).

[83]Y. Tao, M. S. Tillack, S. S. Harilal, K. L. Sequoia, and F. Najmabadi, *Investigation of the interaction of a laser pulse with a preformed Gaussian Sn plume for an extreme ultraviolet lithography source*, J. Appl. Phys. **101**, 023305 (2007).

[84]R. A. Burdt, Y. Ueno, Y. Tao, S. Yuspeh, M. S. Tillack, and F. Najmabadi, *Recombination effects during expansion into vacuum in laser produced Sn plasma*, Appl. Phys. Lett. **97**, 041502 (2010).

[85]R. Schupp, F. Torretti, R. A. Meijer, M. Bayraktar, J. Sheil, J. Scheers, D. Kurilovich, A. Bayerle, A. A. Schafgans, M. Purvis, K. S. E. Eikema, S. Witte, W. Ubachs, R. Hoekstra, and O. O. Versolato, *Radiation transport and scaling of optical depth in Nd:YAG laser-produced microdroplet-tin plasma*, Appl. Phys. Lett. **115**, 124101 (2019).

[86]L. Behnke, R. Schupp, Z. Bouza, M. Bayraktar, Z. Mazzotta, R. Meijer, J. Sheil, S. Witte, W. Ubachs, R. Hoekstra, and O. O. Versolato, *Extreme ultraviolet light from a tin plasma driven by a 2-μm-wavelength laser*, Opt. Express **29**, 4475–4487 (2021).

[87]L. Poirier, A. Bayerle, A. Lassise, F. Torretti, R. Schupp, L. Behnke, Y. Mostafa, W. Ubachs, O. O. Versolato, and R. Hoekstra, *Cross-calibration of a combined electrostatic and time-of-flight analyzer for energy- and charge-state-resolved spectrometry of tin laser-produced plasma*, Appl. Phys. B **128**, 39 (2021).

[88] A. Sunahara, A. Sasaki, and K. Nishihara, *Two dimensional radiation hydrodynamic simulation for extreme ultra-violet emission from laser-produced tin plasmas*, J. Phys.: Conf. Ser. **112**, 042048 (2008).

[89] K. Koshelev, V. Ivanov, V. Medvedev, V. M. Krivtsun, V. G. Novikov, and A. S. Grushin, *Return-to-zero line code modeling of distributed tin targets for laser-produced plasma sources of extreme ultraviolet radiation*, Journal of Micro/Nanolithography, MEMS, and MOEMS **11**, 1–7 (2012).

[90] V. Sizyuk, A. Hassanein, and T. Sizyuk, *Three-dimensional simulation of laser-produced plasma for extreme ultraviolet lithography applications*, J. Appl. Phys. **100**, 103106 (2006).

[91] A. Sunahara, private communication, 2021.

[92] R. Hockney and J. Eastwood, *Computer Simulations Using Particles* (McGraw-Hill, 1981).

[93] C. K. Birdsall and A. B. Langdon, *Plasma Physics via Computer Simulation, Series in Plasma Physics* (Taylor and Francis, 1991).

[94] K. Germaschewski, W. Fox, S. Abbott, N. Ahmadi, K. Maynard, L. Wang, H. Ruhl, and A. Bhattacharjee, *The plasma simulation code: a modern particle-in-cell code with patch-based load-balancing*, J. Comput. Phys. **318**, 305–326 (2016).

[95] A. Tauschwitz, M. Basko, A. Frank, V. Novikov, A. Grushin, A. Blazevic, M. Roth, and J. Maruhn, *2D radiation-hydrodynamics modeling of laser-plasma targets for ion stopping measurements*, High Energy Density Phys. **9**, 158–166 (2013).

[96] S. Faik, A. Tauschwitz, M. M. Basko, J. A. Maruhn, O. Rosmej, T. Rienecker, V. G. Novikov, and A. S. Grushin, *Creation of a homogeneous plasma column by means of hohlraum radiation for ion-stopping measurements*, High Energy Density Phys. **10**, 47–55 (2014).

[97] M. M. Basko, M. S. Krivokorytov, A. Y. Vinokhodov, Y. V. Sidelnikov, V. M. Krivtsun, V. V. Medvedev, D. A. Kim, V. O. Kompanets, A. A. Lash, and K. N. Koshelev, *Fragmentation dynamics of liquid–metal droplets under ultra-short laser pulses*, Laser Phys. Lett. **14**, 036001 (2017).

[98] D. Kurilovich, M. M. Basko, D. A. Kim, F. Torretti, R. Schupp, J. C. Visschers, J. Scheers, R. Hoekstra, W. Ubachs, and O. O. Versolato, *Power-law scaling of plasma pressure on laser-ablated tin microdroplets*, Phys. Plasmas **25**, 012709 (2018).

[99] J. K. Dukowicz, M. C. Cline, and F. L. Addessio, *A general topology Godunov method*, J. Comput. Phys. **82**, 29–63 (1989).

[100] F. L. Addessio, J. R. Baumgardner, J. K. Dukowicz, N. L. Johnson, B. A. Kashiwa, R. M. Rauenzahn, and C. Zemach, *CAVEAT: A Computer Code for Fluid Dynamics Problems With Large Distortion and Internal Slip*, Report LA-10613-MS-Rev. 1, UC-32 (Los Alamos National Laboratory, 1992).

[101] E. Livne and A. Glasner, *A finite difference scheme for the heat conduction equation*, J. Comput. Phys. **58**, 59–66 (1985).

[102] M. M. Basko, *A model for the conversion of ionbeam energy into thermal radiation*, Phys. Fluids B: Plasma Physics **4**, 3753–3763 (1992).

[103] Y. Kawasuji, K. M. Nowak, T. Hori, T. Okamoto, H. Tanaka, Y. Watanabe, T. Abe, T. Kodama, Y. Shiraishi, H. Nakarai, et al., *Key components technology update of the 250W high-power LPP-EUV light source*, in SPIE Advanced Lithography, Vol. 10143 (International Society for Optics and Photonics, 2017), 101432G.

[104] D. J. Hemminga, L. Poirier, M. M. Basko, R. Hoekstra, W. Ubachs, O. O. Versolato, and J. Sheil, *High-energy ions from Nd:YAG laser ablation of tin microdroplets: comparison between experiment and a single-fluid hydrodynamic model*, Plasma Sources Sci. Technol. **30**, 105006 (2021).

[105] M. Brandstätter, N. Gambino, and R. S. Abhari, *Temporally and spatially resolved ion dynamics of droplet-based laser-produced tin plasmas in lateral expansion direction*, J. Appl. Phys. **123**, 043308 (2018).

[106] N. Gambino, M. Brandstätter, B. Rollinger, and R. Abhari, *A hemispherical Langmuir probe array detector for angular resolved measurements on droplet-based laser-produced plasmas*, Rev. Sci. Instrum. **85**, 093302 (2014).

[107] O. Morris, P. Hayden, P. Dunne, F. O'Reilly, G. O'Sullivan, E. L. Antonsen, S. N. Srivastava, K. C. Thompson, and D. N. Ruzic, *Determination of charge state, energy and angular distributions of tin ions emitted from laser produced plasma based EUV sources*, J. Phys.: Conf. Ser. **58**, 391–394 (2007).

[108] P. Yeates, C. Fallon, E. T. Kennedy, and J. T. Costello, *Charge resolved electrostatic diagnostic of colliding copper laser plasma plumes*, Phys. Plasmas **18**, 103104 (2011).

[109] J. C. S. Kools, T. S. Baller, S. T. De Zwart, and J. Dieleman, *Gas flow dynamics in laser ablation deposition*, J. Appl. Phys. **71**, 4547–4556 (1992).

[110] Q. Qin, M. Zhou, and D. Mao, *Time-of-flight mass spectrometric study on UV laser ablation of silver chloride*, Appl. Surf. Sci. **119**, 321–329 (1997).

[111]R. Kelly and R. Dreyfus, *Reconsidering the mechanisms of laser sputtering with Knudsen-layer formation taken into account*, Nucl. Instrum. Methods Phys. Res. B **32**, 341–348 (1988).

[112]P. Hess, R. Bailey, A. Boccara, and Physikzentrum (Bad Honnef, Germany), *Photoacoustic, Photothermal, and Photochemical Processes at Surfaces and in Thin Films*, Topics in current physics (Springer-Verlag, 1989).

[113]Z. Chen, X. Wang, D. Zuo, and J. Wang, *Investigation of ion characteristics in CO_2 laser irradiating predeformed tin-droplet plasma*, Laser Part. Beams **34**, 552–561 (2016).

[114]L. Poirier, A. Lassise, Y. Mostafa, L. Behnke, N. Braaksma, L. Assink, O. Versolato, and R. Hoekstra, *Energy- and charge-state-resolved spectrometry of tin-laser-produced plasma using a retarding field analyzer*, Appl. Phys. B **128**, 135 (2022).

[115]L. Assink et al., *In preparation*, (2022).

[116]J. Hernandez-Rueda, B. Liu, D. J. Hemminga, Y. Mostafa, R. A. Meijer, D. Kurilovich, M. Basko, H. Gelderblom, J. Sheil, and O. O. Versolato, *Early-time hydrodynamic response of a tin droplet driven by laser-produced plasma*, Phys. Rev. Research **4**, 013142 (2022).

[117]B. Liu, R. A. Meijer, J. Hernandez-Rueda, D. Kurilovich, Z. Mazzotta, S. Witte, and O. O. Versolato, *Laser-induced vaporization of a stretching sheet of liquid tin*, J. Appl. Phys. **129**, 053302 (2021).

[118]R. A. Meijer, R. Schupp, J. Sheil, M. M. Basko, K. S. E. Eikema, O. O. Versolato, and S. Witte, *Spall-velocity reduction in double-pulse impact on tin microdroplets*, Phys. Rev. Applied **16**, 024026 (2021).

[119]Y. Tao, R. J. Rafac, I. V. Fomenkov, D. J. Brown, and D. J. Golich, *Target for extreme ultraviolet light source*, US Patent 8,912,514, Dec. 2014.

[120]M. Purvis, I. V. Fomenkov, A. A. Schafgans, P. Mayer, K. Hummler, M. H. Leenders, Y. Tao, S. I. Rokitski, J. Stewart, A. I. Ershov, R. J. Rafac, S. D. Dea, G. O. Vaschenko, D. C. Brandt, and D. J. Brown, *Laser-produced plasma incoherent EUV light sources for high-volume manufacturing semiconductor lithography (Conference Presentation)*, in X-Ray Lasers and Coherent X-Ray Sources: Development and Applications XIII, Vol. 11111, edited by A. Klisnick and C. S. Menoni (International Society for Optics and Photonics, 2019).

[121] T. Sizyuk and A. Hassanein, *Tuning laser wavelength and pulse duration to improve the conversion efficiency and performance of EUV sources for nanolithography*, Phys. Plasmas **27**, 103507 (2020).

[122] S. S. Churilov and A. N. Ryabtsev, *Analysis of the spectra of In XII–XIV and Sn XIII–XV in the far-VUV region*, Opt. Spectrosc. **101**, 169–178 (2006).

[123] A. N. Ryabtsev, É. Y. Kononov, and S. S. Churilov, *Spectra of rubidium-like Pd X-Sn XIV ions*, Opt. Spectrosc. **105**, 844–850 (2008).

[124] H. Mizoguchi, T. Abe, Y. Watanabe, T. Ishihara, T. Ohta, T. Hori, A. Kurosu, H. Komori, K. Kakizaki, A. Sumitani, O. Wakabayashi, H. Nakarai, J. Fujimoto, and A. Endo, *First generation laser-produced plasma source system for HVM EUV lithography*, Proc. SPIE **7636**, 763608 (2010).

[125] V. Y. Banine, K. N. Koshelev, and G. H. P. M. Swinkels, *Physical processes in EUV sources for microlithography*, J. Phys. D: Appl. Phys. **44**, 253001 (2011).

[126] E. Louis, A. E. Yakshin, T. Tsarfati, and F. Bijkerk, *Nanometer interface and materials control for multilayer EUV-optical applications*, Prog. Surf. Sci **86**, 255–294 (2011).

[127] A. L. Klein, W. Bouwhuis, C. W. Visser, H. Lhuissier, C. Sun, J. H. Snoeijer, E. Villermaux, D. Lohse, and H. Gelderblom, *Drop Shaping by Laser-Pulse Impact*, Phys. Rev. Appl. **3**, 044018 (2015).

[128] H. Gelderblom, H. Lhuissier, A. L. Klein, W. Bouwhuis, D. Lohse, E. Villermaux, and J. H. Snoeijer, *Drop deformation by laser-pulse impact*, J. Fluid Mech. **794**, 676–699 (2016).

[129] E. Villermaux and B. Bossa, *Drop fragmentation on impact*, J. Fluid Mech. **668**, 412–435 (2011).

[130] Y. Wang, R. Dandekar, N. Bustos, S. Poulain, and L. Bourouiba, *Universal rim thickness in unsteady sheet fragmentation*, Phys. Rev. Lett. **120**, 204503 (2018).

[131] A. L. Klein, D. Kurilovich, H. Lhuissier, O. O. Versolato, D. Lohse, E. Villermaux, and H. Gelderblom, *Drop fragmentation by laser-pulse impact*, J. Fluid Mech. **893**, A7 (2020).

[132] Y. Wang and L. Bourouiba, *Growth and breakup of ligaments in unsteady fragmentation*, J. Fluid Mech. **910** (2021).

[133] C. Josserand and S. T. Thoroddsen, *Drop impact on a solid surface*, Annu. Rev. Fluid Mech. **48**, 365–91 (2016).

[134]S. Wildeman, C. W. Visser, C. Sun, and D. Lohse, *On the spreading of impacting drops*, J. Fluid Mech. **805**, 636655 (2016).

[135]C. Clanet, C. Béguin, D. Richard, and D. Quéré, *Maximal deformation of an impacting drop*, J. Fluid Mech. **517**, 199–208 (2004).

[136]J. Philippi, P.-Y. Lagrée, and A. Antkowiak, *Drop impact on a solid surface: short-time self-similarity*, J. Fluid Mech. **795**, 96135 (2016).

[137]J. Eggers, M. Fontelos, C. Josserand, and S Zaleski, *Drop dynamics after impact on a solid wall: theory and simulations*, Phys. Fluids **22**, 1063 (2010).

[138]C. W. Visser, P. E. Frommhold, S. Wildeman, R. Mettin, D. Lohse, and C. Sun, *Dynamics of high-speed micro-drop impact: numerical simulations and experiments at frame-to-frame times below 100 ns*, Soft Matter **11**, 1708–1722 (2015).

[139]Y. Wang and L. Bourouiba, *Drop impact on small surfaces: thickness and velocity profiles of the expanding sheet in the air*, J. Fluid Mech. **814**, 510–534 (2017).

[140]Y. Wang, "Fundamentals in unsteady fluid fragmentation from drop impact", PhD thesis (Massachusetts Institute of Technology, 2021).

[141]D. Kurilovich, "Laser-induced dynamics of liquid tin microdroplets", PhD thesis (Vrije Universiteit Amsterdam, 2019).

[142]T. de Faria Pinto, J. Mathijssen, R. Meijer, H. Zhang, A. Bayerle, D. Kurilovich, O. O. Versolato, K. S. Eikema, and S. Witte, *Cylindrically and non-cylindrically symmetric expansion dynamics of tin microdroplets after ultrashort laser pulse impact*, Appl. Phys. A **127**, 1–10 (2021).

[143]R. A. Meijer, D. Kurilovich, K. S. E. Eikema, O. O. Versolato, and S. Witte, *The transition from short- to long-timescale pre-pulses: laser-pulse impact on tin microdroplets*, J. Appl. Phys. **131**, 105905 (2022).

[144]J. Hermens, H. Gelderblom, B. Liu, J. Duffhues, P. Rindt, and O. O. Versolato, *Laser-impact-induced splashing: an analysis of the splash crown evolution after Nd:YAG ns-pulse laser impact on a liquid tin pool*, Appl. Phys. B **127**, 1–6 (2021).

[145]Y. Wang and L. Bourouiba, *Unsteady sheet fragmentation: droplet sizes andăspeeds*, J. Fluid Mech. **848**, 946967 (2018).

[146]M. M. Basko, J. Maruhn, and A. Tauschwitz, *Development of a 2D radiation-hydrodynamics code RALEF for laser plasma simulations, GSI Report 2010-1, PLASMA-PHYSICS-25 (GSI Helmholtzzentrum für Schwerionenforschung GmbH)*, 2010.

[147] M. M. Basko, P. V. Sasorov, M Murakami, V. G. Novikov, and A. S. Grushin, *One-dimensional study of the radiation-dominated implosion of a cylindrical tungsten plasma column*, Plasma Phys. Control. Fusion **54**, 055003 (2012).

[148] R. Schupp, L. Behnke, J. Sheil, Z. Bouza, M. Bayraktar, W. Ubachs, R. Hoekstra, and O. O. Versolato, *Characterization of 1- and 2−μm-wavelength laser-produced microdroplet-tin plasma for generating extreme-ultraviolet light*, Phys. Rev. Research **3**, 013294 (2021).

[149] M. M. Basko, J. Maruhn, and A. Tauschwitz, *An efficient cell-centered diffusion scheme for quadrilateral grids*, J. Comput. Phys. **228**, 2175–2193 (2009).

[150] A. Dedner and P. Vollmöller, *An adaptive higher order method for solving the radiation transport equation on unstructured grids*, J. Comput. Phys. **178**, 263–289 (2002).

[151] J. I. Castor, *Radiation Hydrodynamics*, tech. rep. (Lawrence Livermore National Lab (LLNL), Livermore, CA (United States), 2003).

[152] S. A. Reijers, J. H. Snoeijer, and H. Gelderblom, *Droplet deformation by short laser-induced pressure pulses*, J. Fluid Mech. **828**, 374–394 (2017).

[153] C. R. Phipps, T. P. Turner, R. F. Harrison, G. W. York, W. Z. Osborne, G. K. Anderson, X. F. Corlis, L. C. Haynes, H. S. Steele, K. C. Spicochi, and T. R. King, *Impulse coupling to targets in vacuum by KrF, HF, and CO_2 single-pulse lasers*, J. Appl. Phys. **64**, 1083–1096 (1988).

[154] P. W. Humrickhouse, *An equation of state and compendium of thermophysical properties of liquid tin, a prospective plasma-facing material*, IEEE Trans Plasma Sci. **47**, 3374–3379 (2019).

[155] S. Reijers, D. Kurilovich, F. Torretti, H. Gelderblom, and O. O. Versolato, *Laser-to-droplet alignment sensitivity relevant for laser-produced plasma sources of extreme ultraviolet light*, J. App. Phys. **124**, 013102 (2018).

[156] D. Hudgins, N. Gambino, B. Rollinger, and R. Abhari, *Neutral cluster debris dynamics in droplet-based laser-produced plasma sources*, J. Phys. D: Appl. Phys. **49**, 185205 (2016).

[157] S. K. Moore, *EUV lithography finally ready for fabs*, IEEE Spectrum **55**, 46–48 (2018).

[158] J. Fujimoto, H. Mizoguchi, T. Abe, S. Tanaka, T. Ohta, T. Hori, T. Yanagida, and H. Nakarai, *Laser-produced plasma-based extreme-ultraviolet light source technology for high-volume manufacturing extreme-ultraviolet lithography*, Journal of Micro/Nanolithography, MEMS, and MOEMS **11**, 1 –15 (2012).

[159]S. Y. Grigoryev, B. Lakatosh, M. Krivokorytov, V. Zhakhovsky, S. Dyachkov, D. Ilnitsky, K. Migdal, N. Inogamov, A. Y. Vinokhodov, V. Kompanets, Y. V. Sidelnikov, V. Krivtsun, K. Koshelev, and V. Medvedev, *Expansion and fragmentation of a liquid-metal droplet by a short laser pulse*, Phys. Rev. Appl. **10**, 064009 (2018).

[160]S. Fujioka, H. Nishimura, K. Nishihara, A. Sasaki, A. Sunahara, T. Okuno, N. Ueda, T. Ando, Y. Tao, Y. Shimada, K. Hashimoto, M. Yamaura, K. Shigemori, M. Nakai, K. Nagai, T. Norimatsu, T. Nishikawa, N. Miyanaga, Y. Izawa, and K. Mima, *Opacity effect on extreme ultraviolet radiation from laser-produced tin plasmas*, Phys. Rev. Lett. **95**, 235004 (2005).

[161]I. V. Fomenkov, M. A. Purvis, A. A. Schafgans, Y. Tao, S. Rokitski, J. Stewart, A. LaForge, A. I. Ershov, R. J. Rafac, S. D. Dea, C. Rajyaguru, G. O. Vaschenko, M. Abraham, D. C. Brandt, and D. J. Brown, *NXE:3400B EUV source performance in the field, readiness for HVM and power scaling beyond 250W*, in International Conference on Extreme Ultraviolet Lithography 2018, Vol. 10809, edited by K. G. Ronse, E. Hendrickx, P. P. Naulleau, P. A. Gargini, and T. Itani (2018).

[162]D. C. Brandt, M. Purvis, I. Fomenkov, D. Brown, A. Schafgans, P. Mayer, and R. Rafac, *Advances toward high power EUV sources for EUVL scanners for HVM in the next decade and beyond*, in Extreme Ultraviolet (EUV) Lithography XII, Vol. 11609, edited by N. M. Felix and A. Lio (International Society for Optics and Photonics, 2021).

[163]K. Nowak, T. Ohta, T. Suganuma, J. Fujimoto, H. Mizoguchi, A. Sumitani, and A. Endo, *CO_2 laser drives extreme ultraviolet nano-lithography second life of mature laser technology*, Opto-Electr. Rev. **21**, 345–354 (2013).

[164]Y. Yuan, Y. Y. Ma, W. P. Wang, S. J. Chen, Y. Cui, M. Zi, X. H. Yang, G. B. Zhang, and Y. X. Leng, *Enhancing the conversion efficiency of extreme ultraviolet light sources using a 2 μm wavelength laser*, Plasma Phys. Control. Fusion **64**, 025001 (2021).

[165]C. W. Siders, A. C. Erlandson, T. C. Galvin, H. Frank, S. Langer, B. A. Reagan, H. Scott, E. F. Sistrunk, and T. M. Spinka, *Efficient high power laser drivers for next-generation High Power EUV sources*, in Source Workshop, S22 (Advanced Photon Technologies, NIF and Photon Science, Lawrence Livermore National Laboratory, DOE/NNSA, Nov. 2019).

[166]F. Torretti, F. Liu, M. Bayraktar, J. Scheers, Z. Bouza, W. Ubachs, R. Hoekstra, and O. O. Versolato, *Spectral characterization of an industrial EUV light source for nanolithography*, J. Phys. D: Appl. Phys. **53**, 055204 (2019).

[167] S. Langer, C. Siders, T. Galvin, H. Scott, and E. Sistrunk, *Simulations of EUV Sources Driven by CO$_2$ and Thulium Lasers*, in Source Workshop, S94 (Lawrence Livermore National Laboratory, DOE/NNSA, Nov. 2019).

[168] I. Fomenkov, *EUV Source for Lithography in HVM: performance and prospects*, in Source Workshop, S1 (ASML, Nov. 2019).

[169] I. Y. Vichev, A. D. Solomyannaya, A. S. Grushin, and D. A. Kim, *On certain aspects of the THERMOS toolkit for modeling experiments*, High Energy Density Phys. **33**, 100713 (2019).

[170] R. Schupp, L. Behnke, Z. Bouza, Z. Mazzotta, Y. Mostafa, A. Lassise, L. Poirier, J. Sheil, M. Bayraktar, W. Ubachs, R. Hoekstra, and O. O. Versolato, *Characterization of angularly resolved EUV emission from 2-μm-wavelength laser-driven Sn plasmas using preformed liquid disk targets*, J. Phys. D: Appl. Phys. **54**, 365103 (2021).

[171] Y. Shimada, H. Nishimura, M. Nakai, K. Hashimoto, M. Yamaura, Y. Tao, K. Shigemori, T. Okuno, K. Nishihara, T. Kawamura, et al., *Characterization of extreme ultraviolet emission from laser-produced spherical tin plasma generated with multiple laser beams*, Appl. Phys. Lett. **86**, 051501 (2005).

[172] A. Z. Giovannini and R. S. Abhari, *Effects of the dynamics of droplet-based laser-produced plasma on angular extreme ultraviolet emission profile*, Appl. Phys. Lett. **104**, 194104 (2014).

[173] K. Nishihara, A. Sasaki, A. Sunahara, and T. Nishikawa, "Conversion Efficiency of LPP Sources", in *EUV sources for lithography*, Vol. 149, edited by V. Bakshi (SPIE Press, Bellingham, Washington, 2006) Chap. 11, pp. 339 –370.

[174] K. Nishihara, *Scaling laws of plasma ablation by thermal radiation*, Jpn. J. Appl. Phys. **21**, L571–L573 (1982).

[175] N. Tanaka, M. Masuda, R. Deguchi, M. Murakami, A. Sunahara, S. Fujioka, A. Yogo, and H. Nishimura, *Characterization of material ablation driven by laser generated intense extreme ultraviolet light*, Appl. Phys. Lett. **107**, 114101 (2015).

List of publications

Chapter 2

D. J. Hemminga, L. Poirier, M. Basko, W. Ubachs, R. Hoekstra, O. O. Versolato, and J. Sheil, *High-energy ions from Nd:YAG laser ablation of tin microdroplets: Comparison between experiment and a single-fluid hydrodynamic model*, Plasma Sci. Technol. **30**, 105006 (2021).⋆

⋆ D. J. Hemminga contributed to investigation through performing simulations, visualization, and both writing of the first draft and writing, review and editing of the final draft.

Chapter 3

L. Poirier[†], D. J. Hemminga[†], A. Lassise, L. Assink, R. Hoekstra, J. Sheil, and O. O. Versolato, *Strongly anisotropic ion emission in the expansion of Nd:YAG-laser-produced plasma*, Phys. Plasmas **29**, 123102 (2022).⋆

[†] L. Poirier and D. J. Hemminga contributed equally.

⋆ D. J. Hemminga contributed to conceptualization, formal analysis, investigation through performing simulations, visualization, and both writing of the first draft and writing, review and editing of the final draft.

Chapter 4

J. Hernandez-Rueda, B. Liu, D. J. Hemminga, Y. Mostafa, R. A. Meijer, D. Kurilovich, M. Basko, H. Gelderblom, J. Sheil, and O. O. Versolato, *Early-time hydrodynamic response of a tin droplet driven by laser-produced plasma*, Phys. Rev. Research **4**, 013142 (2022).⋆

⋆ D. J. Hemminga contributed to formal analysis, investigation through performing simulations, and both writing of the first draft and writing, review and editing of the final draft.

Chapter 5

D. J. Hemminga, O. O. Versolato, and John Sheil, *Simulations of plasmas driven by laser wavelengths in the 1.064 – 10.6 µm range as future extreme ultraviolet light sources*, Phys. Plasmas **30**, 033301 (2023).⋆

⋆ D. J. Hemminga contributed to formal analysis, investigation through performing simulations, visualization, and both writing of the first draft and writing, review and editing of the final draft.

The author has summarized the work of this thesis in the following publication:

D. J. Hemminga, L. Poirier, J. Hernandez-Rueda, B. Liu, A. Lassise, R. Hoekstra, J. Sheil, O. O. Versolato, *Tin fluid dynamics driven by laser-produced plasmas relevant to EUV nanolithography*, Proc. SPIE **12494**, Optical and EUV Nanolithography XXXVI, 124941B (2023).

Acknowledgments

As the physics of my four-year PhD journey is now recorded in this manuscript, I want to spend this last section thanking the people who helped me along the way. I'm thankful for each of you who have contributed in their own way: either large or small, direct or indirect, it was all very much appreciated.

Foremost, the person with who I spend the most time at work, John. It was a pleasure working with you! From my start on the 'theory island' where you were always open to questions, your passionate explanations on the glass wall (which may still be there to this day), to our weekly video chats which were bright moments during the pandemic. It was an honor to be the unofficial first PhD student in your newfound group, I wish you much 'beautiful physics' in the future.

My thanks also goes out to Oscar, thank you for supervising me in this PhD journey. I admire your ability of working on a long-term vision while managing a research group. During the last months, I realized how we went through my PhD project according to the plan put together at the beginning. It was great to come back to your group, after you already supervised my BSc project, and work together for much longer.

I would like to thank both Wim U. and Ronnie for their relaxed, but critical stance towards my work. Wim, you've played a large role in my career: from introducing me to ARCNL for a BSc project, to discussing opportunities for my career after this PhD. I'm very thankful for this.

For a vital component of the results presented in this thesis, and therefore my PhD project as a whole, I would like to express my gratitude to Mikhail. I've learned

For the nice interactions, I would also like to thank Emilia, Klaasjan, Paul, Peter and Roland. Wim v. d. Z., thank you for your input on my work and career, first from the ASML side and now at ARCNL. Marjan, thank you for managing the institute. Joost, thank you for heading the institute and for your critical questions. For their willingness to help, I would like to thank Nik, Rosa, Romy, Cathelijne, Marja, Marga, Jusra and Ellen. For the fruitful discussions, I would like to thank our contacts at ASML. In particular, thank you, Niels and Elio, for the nice interactions. For all their calculations, I would like to thank the supercomputers Cartesius and Snellius, and their administrator SURF. Furthermore, I'm thankful for the European Research Council for financing my PhD project.

Beste Marinus, we kennen elkaar al zo lang. Ik ben heel blij dat je de kaft van mijn proefschrift hebt ontworpen; ik vond het een heel gezellige samenwerking! Bedankt dat je steeds geïnteresseerd was in mijn project, ik heb jouw doorvragen erg gewaardeerd. Dit geldt ook voor jullie, Han en Marleen, bedankt voor jullie interesse en gastvrijheid.

Beste Mathilde, ik vind het heel fijn dat we contact hebben gehouden tussen school, studie en nu werk door. Onze bioscoop- en museumbezoekjes waren altijd welkome ontspanning. Bedankt dat je mij (letterlijk) weer op de been hebt geprobeerd te krijgen door mij ijsjes te brengen. Beste Avital en Thom, bedankt voor jullie geloof in mij. Onze lange videogesprekken waren een lichtpuntje tussen al het thuiswerken.

Beste Patrick, ik vond het fijn om de 'promotiereis' samen met jou te delen. Ik vond het gezellig om samen naar Zandvoort te gaan, na de vele keren F1 kijken op tv. Beste Mark, bedankt dat jij altijd zin (en bijna altijd tijd) hebt om samen te gamen. Onze sessies zijn momenten dat de tijd vliegt en precies wat ik nodig heb na een drukke werkweek. Ik wil ook graag mijn familie bedanken voor hun interesse in mijn studie en promotieproject.

Tenslotte, lieve Herma en Haijo, het is moeilijk te beschrijven hoe dankbaar ik ben dat jullie mijn ouders zijn. Ik ben dankbaar voor het luisterend oor voor al mijn verhalen over mijn promotieproject. Ik heb de plek om altijd thuis te kunnen komen heel erg gewaardeerd, zeker tijdens de coronapandemie en met een gebroken been. Jullie hebben er een groot aandeel in dat ik dit promotieproject ben begonnen, heb volgehouden en nu heb voltooid.